NTNU
Norwegian University of
Science and Technology

Two-Component Spin-Orbit Coupled Ultracold Atoms in the Triangular Lattice

A Monte Carlo Study

Håvard Homleid Haugen

MSc in Physics
Submission date: June 2018
Supervisor: Asle Sudbø, IFY

Norwegian University of Science and Technology
Department of Physics

Abstract

Technological advancements in ultracold atom experiments has over the last decades triggered an increased interest in physically intuitive Hamiltonians used to explore fundamental interactions in strongly correlated systems. Motivated by this we study a Bose-Hubbard tight binding model, describing bosonic atoms in a triangular lattice potential with two internal pseudo-spin degrees of freedom coupled by spin-orbit coupling. In the strong coupling regime we derive an effective spin Hamiltonian with a Heisenberg-, Dzyaloshinskii-Moriya- and an off-diagonal compass-coupling, providing us with a platform to investigate several quantum magnetic models of interest. Using large scale Monte Carlo annealing simulations, we explore the ground state magnetic textures for different magnitudes of spin-orbit coupling and inter- relative to intra-component scattering. Combining the Monte Carlo results with a variational approach, we construct a zero-temperature phase diagram consisting of ferromagnetic, stripe, spiral and vortex ordering. We also use the Monte Carlo algorithm to investigate the effects of thermal excitations in the systems, by sampling the helicity modulus using two different methods. Results from the fully isotropic Heisenberg model shows that these two methods give qualitatively similar results, but the approach fails when trying to generalise the model to include a Dzyaloshinskii-Moriya interaction. Furthermore, we confirm the well established quasi-long-range ordering in the XY-model on the triangular lattice, and find a weaker, pseudo-critical, behaviour in the Heisenberg model.

Sammendrag

Teknologiske fremskritt i ultrakalde atom-eksperimenter har over de siste 20 årene økt interessen for fysisk intuitive Hamilton-funksjoner som kan brukes til å undersøke fundamentale vekselvirkninger i sterkt korrelerte systemer. Motivert av dette, ser vi på en Bose-Hubbard modell for bosoniske atomer i et triangulært gitter-potensiale med to interne pseudo-spinn frihetsgrader som vekselvirker via spinn-bane kobling. I det sterkt koblede regimet utleder vi en effektiv spinn Hamilton-funksjon der spinnene vekselvirker via en Heisenberg, Dzyaloshinskii-Moriya og ikke-diagonal kompass-interaksjon. Dette gir en generell modell der vi kan se på flere interessant kvante-magnetiske modeller. Ved hjelp av Monte Carlo simuleringer ser vi på magnetiske grunntilstands-teksturer for ulike styrker av spinn-bane kobling og spredningstyrke for partikler med likt og ulikt spinn. Ved å kombinere resultatene fra Monte Carlo med en variasjons-metode kommer vi frem til et null-temperatur fasediagram med ferromagnetiske, spiral, stripe og virvel-faser. Vi bruker også Monte Carlo simuleringer til å undersøke hvordan disse fasene blir påvirket av termiske fluktuasjoner. Dette blir gjort ved å måle spinnstivhet på to ulike måter. Simuleringer for en fullstendig isotrop Heisenberg-modell viser at de to metodene gir kvalitativt like resultater, men fremgangsmåten vår fungerer ikke når vi generaliserer spin-modellen til å inkludere Dzyaloshinskii-Moriya vekselvirkninger. I XY-modellen bekrefter vi at det finnes kvasi-langtrekkende ordning på det triangulære gitteret, noe som allerede er vel etablert. Videre finner vi en svakere ordning for Heisenberg-modellen, karakterisert som pseudo-kritisk oppførsel.

Preface

I would like to thank prof. Asle Sudbø for his insight, inspiration and support throughout this year. As I have explored the massive subject of strongly correlated systems, he has provided both a great starting point and a direction along the way. Furthermore, I thank Peder Notto Galteland for helping me with the ropes of Monte Carlo methods, and Even Thingstad for writing a very comprehensive thesis last year, giving a lot of inspiration for this text.

Håvard Homleid Haugen

Contents

Chapter 1

Introduction

The understanding of strongly correlated quantum systems has become imperative to the technological advancement of material- and electronics- engineering, with applications in superconductivity[1, 2, 3], spintronics[4, 5, 6] and topological materials[7]. In recent years ultracold atom experiments have become a frontier quantum simulator, because they provide fundamental insight into complex many-body problems that even today's most powerful supercomputers cannot solve[8]. By cooling atoms down to nanokelvin temperatures, experimentalists can create highly tunable systems[9], ideal to investigate fundamental and novel quantum phenomena. Motivated by this technological advancement, we investigate the Mott insulator phase of a Bose-Hubbard model describing strongly correlated bosons in a triangular optical lattice.

The first experimental realisation of ultracold atoms was achieved in 1995 for Rubidium, Sodium and Lithium[10, 11, 12], confirming theoretical predictions of the quantum gas phase of matter, later called a Bose-Einstein condensate[13, 14]. Since then a lot of work has been done in this rapidly expanding field with increasingly sophisticated cooling and measurement techniques[15, 16, 17][18, 19]. Among these advancements is the ability to produce overlapping condensates in different hyperfine states[20]. These internal states can represent pseudo-spin degrees freedom, used to investigate the spin dynamics of bosonic or fermionic quantum gasses.

Electrons in solids typically move in a periodic potential from the crystalline structure of the material. In ultracold atom experiments, such potentials can be generated by superimposing two or more lasers to create an optical lattice interacting with the condensate[21]. Furthermore, the AC Stark effect makes it possible to realise the optical lattice setup for a gas of electrically neutral atoms[22]. In the absence of long range Coulomb repulsion, two-particle scattering is governed by short range effective contact interactions that can be tuned using Feshbach resonances[23]. Consequently, the mobility of the atoms relative to each other and in the lattice can be tuned separately, making these setups ideal to investigate fundamental interactions that are typically obscured in real solids.

The focal point of this thesis is investigating one such interaction, namely spin-orbit coupling (SOC). In atomic physics, SOC is introduced as a correction to the non-relativistic approximation of the Dirac equation and contributes to fine structure in the atomic energy spectra[24]. It also introduces spin splitting in the energy bands of electrons in crystalline solids[25]. In its simplest form, SOC arises as a linear coupling between the spin and momentum of a charged particle moving in an external electric field. There are several

forms of the SOC-interaction depending on the dimensionality of the system and the external field[26, 27, 28]. One such form arising from a uniform electric field is Rashba SOC, used to explain the exotic spin Hall effect[29].

SOC experienced by electrons in solids is generated by electric field strengths far beyond what is available or convenient in experiments[30]. Moreover, it is desirable to use neutral atoms in experiments due to the tunability of their interactions. This situation is remedied by the creation of *synthetic* SOC, which couples the hyperfine states of the atoms by optical Raman transitions[31]. In a condensate with two hyperfine states such as the popular isotope ^{87}Rb, the result is a pseudo-spin $1/2$ system where the spin-states are coupled by a highly tunable SOC-interaction[32].

The high tunability of cold atom experiments has triggered an interest in physically intuitive Hamiltonians, such as the Bose-Hubbard model. Originally developed to capture the dynamics of electrons in narrow conduction bands[33], its bosonic version has been extensively researched because it contains a quantum mechanical superfluid-insulator phase transition[34]. The Mott insulator phase, realised in the atomic limit at integer on-site occupation, is an incompressible phase with correlated number-fluctuations induced from particle-hole pair excitations in the lattice[35, p.12-13]. Furthermore, the Mott insulator can be described by an effective spin Hamiltonian, providing us with a platform to simulate quantum magnetic models of interest. The Bose-Hubbard model has also been generalised to spinfull bosons with SOC in a square lattice potential[36], and in [37] it was shown that SOC results in an exotic Dzyaloshinskii-Moriya (DM) interaction in the spin Hamiltonian. Giving rise to skyrmion structures and magnetic domain walls protected by topology[38, 39], this interaction has been researched in relation to information storage in magnetic materials[40].

One question that arises from this is what happens when geometric frustration is introduced into such magnetic systems. This is a topic that has been researched extensively in relation to spin-liquids, where geometric frustration can lead to groundstates completely absent of ordering, giving rise to novel phenomena[41]. In this thesis we derive an effective spin Hamiltonian from a Bose Hubbard model with SOC similar to [37], but on the triangular lattice. Furthermore, we employ extensive classical Monte Carlo simulations to uncover the ground state phase diagram with a plethora of magnetic textures. Finally, we consider the effects of thermal excitations on the ground-states by measuring the helicity modulus, and try to generalise known methods from literature[42, 43] to include SOC.

1.1 Notation and convention

In this section we introduce conventions and notation used throughout the thesis. All quantities are given in natural units with

$$\hbar = k_B = c = 1. \tag{1.1}$$

Triangular lattice

We consider a triangular lattice setup with lattice constant set to unity, $a = 1$. Translation in the lattice is described by the vectors along the bonds between sites

$$\boldsymbol{\epsilon}_{a_1} = \frac{1}{2}\hat{\mathbf{x}} + \frac{\sqrt{3}}{2}\hat{\mathbf{y}}, \qquad \boldsymbol{\epsilon}_{a_2} = \hat{\mathbf{x}}, \qquad \boldsymbol{\epsilon}_{a_3} = \boldsymbol{\epsilon}_{a_2} - \boldsymbol{\epsilon}_{a_1}. \tag{1.2}$$

Two sites, i and j, are nearest neighbours if $\mathbf{r}_j = \mathbf{r}_i \pm \boldsymbol{\epsilon}_a \equiv \mathbf{r}_{i\pm a}$, where $a \in \{a_1, a_2, a_3\}$ denotes the direction. In the effective spin Hamiltonian derived in chapter 3, we sum over the three forward directions given by eq. (1.2) by convention. The reciprocal of the triangular lattice is also a triangular lattice, with primitive lattice vectors

$$\mathbf{b}_1 = \frac{4\pi}{\sqrt{3}}\hat{\mathbf{y}}, \qquad \mathbf{b}_2 = 2\pi\hat{\mathbf{x}} - \frac{2\pi}{\sqrt{3}}\hat{\mathbf{y}}, \tag{1.3}$$

where the Brillouin zone of a lattice site in reciprocal space consist of all the points closer to that site than any other.

Pauli matrices

The Pauli matrices are given on the standard form $\boldsymbol{\sigma} = (\sigma^x, \sigma^y, \sigma^z)$, with

$$\sigma^x = \begin{pmatrix} 0 & 1 \\ 1 & 0 \end{pmatrix}, \qquad \sigma^y = \begin{pmatrix} 0 & -i \\ i & 0 \end{pmatrix}, \qquad \sigma^z = \begin{pmatrix} 1 & 0 \\ 0 & -1 \end{pmatrix}, \tag{1.4}$$

and implicitly act on the spin-1/2 degrees of freedom of particle operators. In addition we use the associated Pauli matrices, defined as

$$\sigma^+ = \sigma^x + i\sigma^y, \qquad \sigma^- = \sigma^x - i\sigma^y \tag{1.5}$$

Chapter 2

Ultracold atoms

In this chapter we review the experimental realisation of ultracold atoms, and the theoretical description of a quantum gas. Furthermore, we combine these concepts to show how ultracold atomic gasses can be used to study spin-orbit (SO) coupled bosons in a triangular lattice potential.

2.1 Quantum gas

A gas of atoms has several associated length scales. The characteristic length of interactions is denoted R_e, while the mean inter-particle distance can be written in terms of the density as $n^{-1/3}$. Finally, the wave-like nature of particles are characterised by the thermal de Broglie wavelength

$$\Lambda_T = \sqrt{\frac{2\pi}{mT}} \propto k_T^{-1}, \tag{2.1}$$

where k_T is the thermal wavevector. A gas is characterised as *dilute* when the inter-atomic distance is much larger than the interaction-radius

$$nR_e \ll 1. \tag{2.2}$$

To achieve an ultracold atomic gas, it is important to keep it sufficiently dilute because in a dense gas three-body interactions will lead to formation of molecules. The ultracold gas limit is achieved when the thermal de Broglie wavelength is much larger than the interaction-radius

$$\Lambda_T \gg R_e \rightarrow k_T R_e \ll 1. \tag{2.3}$$

In this limit, most of the inter-particle scattering occurs from inelastic s-wave collisions[44].

When the de Broglie wavelength is much smaller than the mean particle separation, particles behave classically. In the opposite limit, when the temperature is made sufficiently low or the density sufficiently high, the macroscopic properties crucially depend on the microscopic degrees of freedom of the gas. The quantum gas limit is given by

$$n\Lambda_T^3 \geq 1, \tag{2.4}$$

where the wavefunctions of particles start overlapping. In this regime the dynamics of the particles are determined by quantum mechanics, and there is a fundamental difference

between bosonic and fermionic particles. For an ideal gas of bosonic particles, the ultracold quantum phase is characterised by a macroscopic occupation of the lowest particle energy state which has later been named a Bose-Einstein condensate[14, 13].

2.1.1 Experimental cooling methods

In experiments, atomic gases are cooled down to temperatures where their quantum nature becomes important. This happens at densities of $10^{14} - 10^{15}\text{cm}^{-1}$ and temperatures of order 100nK[45, p.5]. To achieve such extreme temperature regimes, different experimental methods are used. Laser cooling relies on the Doppler effect; particles moving in one directions are slowed down by velocity-dependant photon absorption, so that the overall kinetic energy of the gas is decreased[46]. Variations of this method are commonly used in experiments[47, 48, 49, 50]. Other cooling methods rely on evaporative effects. By placing the atom gas in a magnetic[51] or optical[52, 53] trapping potential, the barriers of the potential may be step-wise decreased allowing the most energetic atoms to escape. For atomic species that are difficult to cool down by optical means, sympathetic cooling is used. In this method, the species is thermalised with another, more easily cooled species which is subsequently removed after achieving ultracold temperatures. For example, Potassium has been sympathetically cooled together with ^{87}Rb[54]. The implementation of these methods and their effectiveness typically depend on the details of the atomic species, and in most experiments a combination of laser and evaporative cooling is used.

Because electrons in real solids move in a periodic potential from the crystalline structure, it is desirable to replicate this in ultracold atom experiments. This is achieved by placing the ultracold gas in an optical lattice potential, explained in detail in section 2.4. The optical lattice setup has been experimentally realised for both bosons and fermions[55, 56]. Measurements in ultracold atom experiments are done using absorptive imaging to take time-of-flight images of the gas cloud[57]. Although there exist other methods, this is the most common today because it can be used to measure both density profiles and average velocity. This method was also famously used in the first observation of a Bose-Einstein condensate[10].

2.2 Hyperfine states

Hydrogenic alkali atoms with one electron in the outer shell are qualitatively described by the non-relativistic Hamiltonian

$$H = \frac{p^2}{2m} - \frac{Ze^2}{4\pi\epsilon_0}\frac{1}{r}. \tag{2.5}$$

The resulting eigenstates are degenerate in the angular momentum of the electron, and do not describe the complete picture. Degeneracy of the energy levels is partly lifted by the introduction of the fine structure[58]. Taking into account relativistic corrections to eq. (2.5), a more detailed spectrum with less degeneracy emerges. Even smaller corrections to the

simple one-electron picture are introduced by the Lamb shift from radioactive corrections, the Zeeman effect from external magnetic fields and the Stark effect from electric fields[59].

At the pinnacle of these corrections lie the hyperfine structure. First observed by A. Michelson in 1891, these energy shifts are typically much smaller than those from the fine structure[24, p.232]. The hyperfine structure arises from considering the angular momentum of the nucleus. Although we do not know exactly what happens inside, it consists of nucleons with intrinsic spin along with the possibility of orbital motion. The sum of these constitute the *nuclear spin*, $\mathbf{I}$, where $\mathbf{I}^2$ has eigenvalues $I(I+1)$ given by the nuclear spin quantum number. By considering the nucleus as a point dipole giving rise to a vector potential, we obtain a perturbation term from interactions with the outer shell electron. The energy shifts from perturbation theory give rise to the hyperfine energy corrections to the atomic energy spectrum. These are labelled by the total angular momentum of the atom

$$\mathbf{F} = \mathbf{I} + \mathbf{J}, \tag{2.6}$$

where $\mathbf{J} = \mathbf{S} + \mathbf{L}$ is the spin and orbital angular momentum of the electron. The possible values of the quantum number F depend on the other quantum numbers through standard addition of spin algebra

$$F = |I - J|, |I - J| + 1, ..., I + J - 1, I + J. \tag{2.7}$$

To illustrate how these hyperfine states can be used to represented pseudo-spin internal degrees of freedom, we consider the isotope ^{87}Rb. The lowest orbital $5^2\mathrm{S}_{1/2}$ has $L = 0$ so that $J = 1/2$. Furthermore the nuclear spin is $I = 3/2$[60] , giving rise to two possible internal states $F = 1, 2$. These are further split by an external magnetic field into states labelled by the magnetic quantum number $m_F = -F, ..., +F$. In section 2.3.1 we show how these these states may be coupled to represent spin-1/2 degrees of freedom.

2.3 Spin orbit coupling

The SO interaction is in general a coupling between the spin and momentum of charged particles. It was originally proposed to explain the fine structure of the atomic energy spectrum[61, 62]. In solids it results in spin-splitting of the momentum-dependant energy bands of particles, arising from a broken inversion symmetry in the crystal lattice[63].

The linear form of SOC is obtained by considering a charged particle moving in an electric potential. In the reference frame of the particle, the electric field gives rise an effective magnetic field that couples to the magnetic moment of the particle, $\boldsymbol{\mu}$ through the Zeeman interaction

$$H_{\mathrm{Z}} = -\boldsymbol{\mu} \cdot \mathbf{B}_{\mathrm{eff}}. \tag{2.8}$$

The effective magnetic field is given by the Lorentz transformation

$$\mathbf{B}_{\mathrm{eff}} = -\mathbf{v} \times \mathbf{E}, \tag{2.9}$$

where $\mathbf{v}$ is the velocity of the particle and $\mathbf{E} = -\nabla V$ is the electric field. Combining these expressions, gives the Pauli SO interaction on the form given in [25]

$$H_{\mathrm{SO}} = \lambda_{\mathrm{SO}} \boldsymbol{\sigma} \cdot \mathbf{p} \times (\nabla V), \tag{2.10}$$

where λ_{SO} determines the strength of interaction. For an electron in spherical motion around the nuclei, the Coulomb field points in the radial direction. With electron angular momentum $\mathbf{L} = \mathbf{r} \times \mathbf{p}$ and spin $\mathbf{S} = \boldsymbol{\sigma}/2$, the SO interaction can be written

$$H_{SO} = \lambda'_{\mathrm{SO}}(r) \mathbf{S} \cdot \mathbf{L}. \tag{2.11}$$

This is a linear coupling between the spin and orbital angular momentum of the particle, explaining the name spin-orbit coupling.

In this thesis we consider a two-dimensional system, and are consequently interested in the SOC terms that couple to the p_x- and p_y-components. Writing out all the terms in eq. (2.10) and discarding the terms with p_z gives a generic expression on the form

$$H_{\mathrm{SO}} = \alpha p_x \sigma_y + \beta p_y \sigma_x. \tag{2.12}$$

Setting $\alpha = \beta$ gives a Dresselhaus-type coupling[27], and $\alpha = -\beta$ gives Rashba SOC[26]. Schemes for generating three dimensional SOC have also been realised through the fully isotropic Weyl-coupling[28]. We will consider only the case of Rashba coupling given on the form

$$H_{\mathrm{SO}} = \kappa_R (p_y \sigma_x - p_x \sigma_y), \tag{2.13}$$

where the strength of the interaction is determined by the Rashba coupling parameter κ_{R}.

2.3.1 Synthetic spin-orbit coupling

In solids, spin-orbit interactions are generated by strong electric fields that depend heavily on the details of the material. Because such fields are inconveniently large in experiments, *synthetic* SOC is used to simulate the effect for neutral atoms. Letting the internal F-states discussed previously represent spin-degrees of freedom, synthetic SOC is introduced by coupling different states using Raman lasers.

A Raman process is the absorption of a single photon from one laser beam followed by stimulated re-emission into a second, counter-propagating beam[64]. The photons have recoil momentum $p_{\mathrm{R}} = \lambda^{-1}$, so conservation of momentum dictates that the atom acquires the difference of the these two recoil momenta in the process. If the momentum difference is close to the energy difference of two hyperfine states, this stimulates a resonant transition between these. The laser frequencies in the atomic reference frame are velocity dependant through Doppler shifts, so the transitions can be tuned away from resonance in a velocity-dependant way[30]. Effectively the coupling between the two internal states becomes velocity-dependant, providing a coupling similar to SOC. Such a coupling was experimentally realised for a general 2-dimensional SO interaction in the form of a non-abelian gauge field in 2016[32, 65], enabling the study of Rashba SOC discussed in the previous section.

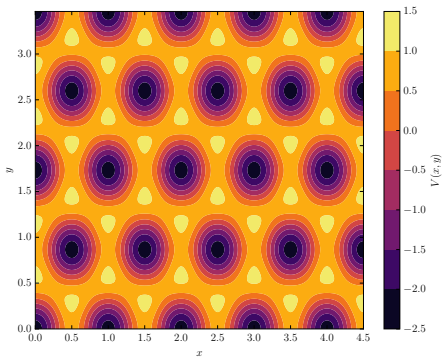

Figure 2.1: Triangular lattice potential from eq. (2.19) with $V_0 = -1.5$ and $q = 4\pi/3$.

2.4 Optical lattice potential

To understand how we can trap neutral atoms with a radiation field, we look at the interactions between these. In the dipole approximation, interactions between an electric field and a neutral particle is given by [45]

$$H = -\mathbf{d} \cdot \boldsymbol{\mathcal{E}}, \tag{2.14}$$

where $\mathbf{d}$ is the dipole moment of the particle, induced by the electric field $\boldsymbol{\mathcal{E}}$. This interaction causes a shift in the energy levels of the atoms, similar to the Stark-effect. To second order in the electric field, the energy shift of the ground state can be written as an effective potential acting on the ground state

$$V_{\mathrm{g}}(\mathbf{r}) = -\frac{1}{2}\alpha'(\omega)\langle \boldsymbol{\mathcal{E}}(\mathbf{r}, t)^2 \rangle. \tag{2.15}$$

Here, $\alpha'(\omega)$ is the real part of the polarisability of the atom, which depends on the frequency of the electric field, along with the matrix elements in the second order perturbation expansion. Typically, the radiation frequency is chosen close to that of an atomic resonance, so that only one matrix element contributes to the polarisability.

We may now generate a spatially varying potential by superimposing several electric fields with equal frequency. In the general case, a superposition of electric fields can be written

$$\boldsymbol{\mathcal{E}}_{\mathrm{tot}}(\mathbf{r}, t) = \sum_i \boldsymbol{\mathcal{E}}_{0i} \cos(\mathbf{q}_i \cdot \mathbf{r} - \omega t + \delta_i). \tag{2.16}$$

Squared and time-averaged, this becomes

$$\langle \boldsymbol{\mathcal{E}}^2 \rangle = \frac{1}{2}\sum_i \boldsymbol{\mathcal{E}}_{0i}^2 + \sum_{i<j} \boldsymbol{\mathcal{E}}_{i0} \cdot \boldsymbol{\mathcal{E}}_{j0} \cos[(\mathbf{q}_i - \mathbf{q}_j) \cdot \mathbf{r} + \delta_i - \delta_j]. \tag{2.17}$$

By choosing the electric field to be polarised along the z-axis, we can create a two-dimensional lattice potential in the xy-plane, with spatially periodic minima given by the wavevectors $\mathbf{q}_i$

and the phases δ_i. The triangular lattice may be generated by superimposing three electric fields of equal phase and with wave-vectors

$$\mathbf{q}_1 = (1, 0, 0)\, q, \qquad \mathbf{q}_2 = \left(-1/2, \sqrt{3}/2, 0\right) q, \qquad \mathbf{q}_3 = \left(-1/2, -\sqrt{3}/2, 0\right) q. \tag{2.18}$$

From eq. (2.17) and eq. (2.15), we obtain the effective lattice potential

$$V(x, y) = \frac{V_0}{2}\left[2\cos\left(3qx/2\right)\cos\left(\sqrt{3}qy/2\right) + \cos\left(\sqrt{3}qy\right)\right] \tag{2.19}$$

which produces a triangular lattice shown in fig. 2.1. A triangular optical lattice potential has been realised experimentally[66].

2.5 Inter-atomic potential

In ultracold atom ensembles, particle separations are typically larger than the length scales associated with interactions between atoms (eq. (2.2)). As a consequence, the two-body interactions dominate and three- and higher-body interactions may to a good approximation be neglected[1].

We describe the two-body interaction with a potential $U(\mathbf{r})$. At small particle separations, the potential is strongly repulsive due to overlapping electron clouds. For larger separations, the main contribution arises from dipole-dipole interactions. Because we consider alkali atoms that are polarised in the optical lattice there is no covalent bonding, giving a relatively weak van der Waals attraction on the form $-1/r^6$.

Scattering of particles with small total energy is dominated by the s-wave contribution to the total cross-section, and can be described by the *scattering length*, a[67, p. 279-284]. Consequently, for the purpose of calculating low-energy properties, the true inter-atomic potential may be replaced by an effective interaction potential proportional to the scattering length

$$U_{\text{eff}}(\mathbf{r}) = U_0\delta(\mathbf{r}), \qquad U_0 = \frac{4\pi a}{m}. \tag{2.20}$$

In detail, the effective potential can be obtained by integrating out short wavelength degrees of freedom, leaving the interactions between long wavelength degrees of freedom as an effective contact potential[45, p. 122-125].

2.5.1 Feshbach resonances and internal states

In cold atom experiments, Feshbach resonances are used to tune the strength of the two-body interaction[68][69]. When the total energy of an open scattering channel is close to a bound state in a closed channel, the incident atoms can scatter into the intermediate bound

[1] This is a requisite to having an ultracold quantum gas, rather than a consequence because three body processes lead to molecule formation.

state. The two particles in the bound state subsequently decay into the open channel. This is a second-order process that gives a contribution to the scattering length on the form [45]

$$a \propto \frac{C}{E - E_{\text{res}}}, \tag{2.21}$$

where E is the total energy of the particles in the open channel, and E_{res} the energy of the bound state. When $E \simeq E_{\text{res}}$, this is the dominating contribution giving rise to a repulsive interaction when the total energy of the open channel is greater than that of the bound state. The hyperfine states couple to external magnetic fields, making it possible to tune the effective interactions through the energy of the bound state[23].

The final note on inter-atomic interactions concerns the internal states. Inelastic scattering typically results in a release of energy allowing atoms to escape from the trapping potential [23], and consequently only elastic scattering processing are considered. For elastic processes, the effective interaction potential is generalised to a component-dependant potential $U_0 \to U_{\sigma\sigma'}$, according to [70]. Due to high tunability, the component-dependent potential can take several forms, but for simplicity, we shall later consider a potential on the form

$$U_{\sigma\sigma'} = U_0 \begin{pmatrix} 1 & \lambda \\ \lambda & 1 \end{pmatrix}, \tag{2.22}$$

where the effective potential only depends on whether the two atoms are in different internal states.

2.6 Quantum mechanical formalism

In this section we show how a general many-particle Hamiltonian can be recast as a lattice model in the tight binding limit. For simplicity we start with spinless particles without SOC, but this is readily generalised in chapter 3. The theory in this section is taken from [71, 72]

Consider a system of N identical bosonic particles of mass m with positions $\mathbf{r}_i$ and momenta $\mathbf{p}_i$. A general many particle Hamiltonian in first quantisation reads

$$H = \sum_{i=1}^{N} \left[\frac{\mathbf{p}_i^2}{2m} + V(\mathbf{r}_i) \right] + \frac{1}{2} \sum_{i \neq j} U(\mathbf{r}_i - \mathbf{r}_j), \tag{2.23}$$

where $V(\mathbf{r})$ is some background potential and the particles interact via the potential $U(\mathbf{r})$. This can be expressed in *second quantisation* by introducing creation and annihilation operators

- $\psi^\dagger(\mathbf{k})$ creates a particle of quasimomentum k.
- $\psi(\mathbf{k})$ removes a particle of quasimomentum k.

These follow the bosonic commutation relation $[\psi(\mathbf{k}), \psi^\dagger(\mathbf{k}')] = \delta_{\mathbf{k},\mathbf{k}'}$, which symmetrises the full many-particle wavefunction under the interchange of two particles. Furthermore, the number operator

$$\hat{n}(\mathbf{k}) = \psi^\dagger(\mathbf{k})\psi(\mathbf{k}), \tag{2.24}$$

counts the number of particles with quasimomentum k. If the system can be diagonalised exactly, the Hamiltonian in eq. (2.23) can now be written

$$H = \sum_{\mathbf{k}} \epsilon_{\mathbf{k}} \hat{n} \tag{2.25}$$

where $\epsilon_{\mathbf{k}}$ is the energy of a particle with quasimomentum $\mathbf{k}$.

In general, when the system is not readily diagonalised, the second quantised form of the Hamiltonian in eq. (2.23) is

$$H = \int \mathrm{d}\mathbf{r} \psi^\dagger(\mathbf{r}) \left[-\frac{\nabla^2}{2m} + V(\mathbf{r}) \right] \psi(\mathbf{r}) + \frac{1}{2} \int \mathrm{d}\mathbf{r}\, \mathrm{d}\mathbf{r}' U(\mathbf{r} - \mathbf{r}') \psi^\dagger(\mathbf{r}) \psi(\mathbf{r}) \psi^\dagger(\mathbf{r}') \psi(\mathbf{r}') \tag{2.26}$$

The position-dependant particle operators in this representation are related to the momenta-dependant operators through the Fourier transform. This is generalised to spinfull particles by adding an index σ representing the spin degrees of freedom to the creation and annihilation operators:

$$\psi^\dagger(\mathbf{r}) \to \psi^\dagger_\sigma(\mathbf{r}), \tag{2.27}$$

$$\psi(\mathbf{r}) \to \psi_\sigma(\mathbf{r}). \tag{2.28}$$

The spin-states have to be summed over in the second quantised form of the Hamiltonian. Furthermore, the commutation relations are now generalised to

$$\left[\psi_\sigma(\mathbf{r}), \psi^\dagger_{\sigma'}(\mathbf{r}') \right] = \delta_{\sigma\sigma'} \delta(\mathbf{r} - \mathbf{r}') \tag{2.29}$$

2.6.1 Tight binding model

Bloch's theorem states that any solution to the Schrödinger equation for particles in a periodic potential (i.e. a lattice potential) must be on the form

$$\phi_{n,\mathbf{p}}(\mathbf{r}) = u_{n,\mathbf{p}}(\mathbf{r}) e^{i\mathbf{p}\cdot\mathbf{r}}, \qquad n = 1, 2, 3, ... \tag{2.30}$$

where $u_{n,\mathbf{p}}(\mathbf{r})$ has the same periodicity as the potential, and $\mathbf{p}$ is the lattice momentum with values inside the Brilloine zone of the reciprocal lattice. The functions $u_{n,\mathbf{p}}(\mathbf{r})$ are typically hard to obtain, even numerically, but when the periodic potential is sufficiently strong we may recast the lattice problem in a *tight binding model*. The central assumption of the tight binding model is that each potential minimum can be approximated by a harmonic oscillator potential. Each particle is thus localised at a lattice site in a state given approximately by the lowest energy eigenfunction of the harmonic potential. Furthermore, there is a small but finite tunnelling rate between adjacent sites from overlapping wavefunctions.

To describe this behaviour the *Wannier functions* are introduced:

$$W_{n,i}(\mathbf{r}) = W_n(\mathbf{r} - \mathbf{r}_i) = \int_{\mathbf{p}\in \mathrm{BZ}} \frac{\mathrm{d}\mathbf{p}}{(2\pi)^2} \phi_{n,\mathbf{p}}(\mathbf{r}) e^{-i\mathbf{r}_i \cdot \mathbf{p}}. \tag{2.31}$$

Using the properties of the Bloch functions in eq. (2.30), it follows that the Wannier functions have three defining properties

I) They are centered around the potential minimas of the lattice.

II) They fall off exponentially.

III) They form an orthonormal set.

Using the third property, the field operators introduced in the second quantised form of the many particle Hamiltonian may be expanded in the Wannier basis

$$\psi^\dagger_\sigma(\mathbf{r}) = \sum_{n,i} W^*_{n,i}(\mathbf{r}) b^\dagger_{i\sigma}. \tag{2.32}$$

The operator $b^\dagger_{i\sigma}$ creates a particle in the n'th Wannier band at lattice site i. Furthermore, the external potential is assumed to be indifferent to the internal spin-states, so there is no spin-index in the Wannier function.

2.7 Energy scales

There are several energy scales associated with the various interactions introduced in this chapter, which warrants a discussion of their relative strengths. With the assumption that the particles are cold with low thermal energy, their energy is associated with the recoil energy $E_\mathrm{R} = k_\mathrm{L}/2m$, where k_L is the wavevector of the optical lattice laser. The strength of the lattice potential is associated with the depth, V_0. In the *deep lattice limit*, $V_0 \gg E_\mathrm{R}$, particles are tightly confined to quasi-bound states in one potential well around a lattice site with oscillatory energy $\omega_0 = 2E_\mathrm{R}(V_0/E_\mathrm{R})^{1/2}$[73].

The strength of the interactions between particles depend on the scattering parameter U_0 introduced in section 2.5, which can be tuned with Feshbach resonances. Furthermore, the effective on-site interaction strength[2], u, in the lattice model depends on the depth of the lattice and the recoil energy as[73]

$$u \propto k_\mathrm{L} a E_\mathrm{R} \left(\frac{V_0}{E_R}\right)^{3/4}, \tag{2.33}$$

where a is the s-wave scattering length. By increasing the lattice depth, the interaction strength is increased relative to the kinetic energy of the particles. For the deep lattice

[2]This will be properly introduced in section 3.1.1.

harmonic approximation to be valid, we still require that $u \ll \omega_0$ which is fulfilled when $k_{\mathrm{L}} a \ll 1$.

SOC is associated with the hyperfine states, and is more finely resolved than the energy scales considered in the previous paragraph. As long as the Raman lasers are detuned far from a resonance to another F-state, they have little or no effect on the quasi-bound harmonic oscillator states on the lattice sites.

Chapter 3

The Bose-Hubbard Hamiltonian

In this chapter, we go through the derivation the Bose-Hubbard Hamiltonian with SOC in a triangular lattice potential. Furthermore, we derive an effective spin Hamiltonian valid in the Mott insulator regime.

3.1 System Hamiltonian

Combining the considerations made in the previous chapter, we may now write down a general Hamiltonian for N identical bosonic particles. The second quantisation form – introduced in section 2.6 – of the non-interacting Hamiltonian reads:

$$H_{\mathrm{ni}} = \sum_{\sigma\sigma'} \int \mathrm{d}\mathbf{r} \psi_\sigma^\dagger(\mathbf{r}) \left[-\frac{\nabla^2}{2m} + V(\mathbf{r}) + \kappa_R(p_y\sigma_x - p_x\sigma_y) \right] \psi_{\sigma'}(\mathbf{r}). \tag{3.1}$$

The external potential includes the triangular lattice potential introduced in section 2.4 along with a slowly varying trapping potential that we take to be constant for the entire system. SOC is introduced on the Rashba form discussed in section 2.3. Furthermore, we consider particles in two internal states labelled by $\sigma \in \{\uparrow, \downarrow\}$. Experimentally this corresponds to a two-component condensate, and we will refer to the internal states as components, species or spin. Mathematically, we may write the field operators as spinors

$$\psi(\mathbf{r}) = \begin{pmatrix} \psi_\uparrow(\mathbf{r}) \\ \psi_\downarrow(\mathbf{r}) \end{pmatrix}, \tag{3.2}$$

where states with opposite spin are only coupled by the Pauli matrices in the SOC-term. Interactions between particles are introduced by the term

$$H_{\mathrm{int}} = \frac{1}{2} \sum_{\sigma\sigma'} \int \mathrm{d}\mathbf{r}\, \mathrm{d}\mathbf{r}' U_{\sigma\sigma'}(\mathbf{r} - \mathbf{r}') \psi_\sigma^\dagger(\mathbf{r}) \psi_\sigma(\mathbf{r}) \psi_{\sigma'}^\dagger(\mathbf{r}') \psi_{\sigma'}(\mathbf{r}'), \tag{3.3}$$

for the generalised component-dependant interaction potential $U_{\sigma\sigma'}(\mathbf{r})$ defined in eq. (2.22).

3.1.1 Wannier functions

In the deep lattice limit, we may expand field operators in the Wannier basis introduced in section 2.6.1. In the deep lattice limit, $V_0 \gg E_{\mathrm{R}}$, the quasi-bound lattice site states are

approximated by the Gaussian groundstate of a harmonic oscillator. Thus, we only include the lowest Wannier band which is written

$$W_i(\mathbf{r}) \simeq \left(\frac{m\omega_0}{\pi}\right)^{1/4} \exp\left(-\frac{m\omega_0(\mathbf{r}-\mathbf{r}_i)^2}{2}\right), \tag{3.4}$$

where ω_0 is the oscillatory energy given in section 2.7.

Consider first the kinetic and external potential term in the non-interacting Hamiltonian. Inserting the Wannier expansion we find

$$H_{K+V} = \sum_{\sigma\sigma'}\sum_{ij}\int \mathrm{d}\mathbf{r} W_i^*(\mathbf{r}) b_{i\sigma}^\dagger \left[-\frac{\nabla^2}{2m} + V(\mathbf{r})\right] W_j(\mathbf{r}) b_{j\sigma'}. \tag{3.5}$$

Both the kinetic term and the external potential are independent of the internal state, so only terms with $\sigma = \sigma'$ contribute. Furthermore, terms with $i = j$ re-normalise the chemical potential. Finally, using the exponential decay of the Wannier functions, only terms where i and j are nearest neighbours contribute. For these terms we introduce the spin-conserving hopping amplitude

$$t \equiv t_{i,i+a} = \int \mathrm{d}\mathbf{r} W_i^*(\mathbf{r}) \left[-\frac{\nabla^2}{2m} + V(\mathbf{r})\right] W_{i+a}(\mathbf{r}) \tag{3.6}$$

where $a \in \{a_1, a_2, a_3\}$ denotes the three directions in the lattice introduced in section 1.1. Inserting the harmonic approximation for the Wannier functions, this amplitude is always real. Furthermore, both the external potential and the kinetic energy are symmetric in every direction on the lattice, so the spin-conserving hopping amplitude is independent of a. The contribution from the kinetic energy and external potential can now be written

$$H_{K+V} = \sum_{\sigma}\sum_{i,a} t\left(b_{i,\sigma}^\dagger b_{i+a,\sigma} + \text{h.c.}\right), \tag{3.7}$$

where the Hermitian conjugate corresponds to tunnelling in the opposite direction $i \to i+a$, so that in total the sum goes over hopping between all nearest neighbours in the lattice.

The SO-interaction couples states of opposite spin through the Pauli matrices. Writing the spin-dependant part of the bosonic operators as spinors, we find in bra-ket notation

$$\langle\uparrow|\sigma_x|\uparrow\rangle = \langle\downarrow|\sigma_x|\downarrow\rangle = \langle\uparrow|\sigma_y|\uparrow\rangle = \langle\downarrow|\sigma_y|\downarrow\rangle = 0. \tag{3.8}$$

Only the off-diagonal terms give non-zero contributions

$$\langle\uparrow|\sigma_x|\downarrow\rangle = \langle\downarrow|\sigma_x|\uparrow\rangle = 1 \tag{3.9}$$

$$\langle\uparrow|\sigma_y|\downarrow\rangle = -i \tag{3.10}$$

$$\langle\downarrow|\sigma_y|\uparrow\rangle = \left(\langle\uparrow|\sigma_y|\downarrow\rangle\right)^* = i \tag{3.11}$$

Denoting the expectation value of Pauli matrices between spin-states as $(\sigma)^{\sigma,\sigma'}$, the SOC-term can be written in terms of the Wannier expansion as

$$H_{\text{SO}} = \sum_{\sigma\sigma'}\sum_{ij}\int \mathrm{d}\mathbf{r} W_i^*(\mathbf{r}) b_{i\sigma}^\dagger \kappa_R \left[(\sigma_x)^{\sigma,\sigma'} p_y - (\sigma_y)^{\sigma,\sigma'} p_x\right] W_j(\mathbf{r}) b_{j\sigma'}. \tag{3.12}$$

Summing only over nearest neighbour terms, we introduce the amplitude for hopping *with* spin-flip,

$$s_{i,i+a}^{\sigma,-\sigma} = \kappa_R \left[(\sigma_x)^{\sigma,-\sigma} \int \mathrm{d}\mathbf{r} W_i^*(\mathbf{r}) p_y W_{i+a}(\mathbf{r}) - (\sigma_y)^{\sigma,-\sigma} \int \mathrm{d}\mathbf{r} W_i^*(\mathbf{r}) p_x W_{i+a}^*(\mathbf{r}) \right] \tag{3.13}$$

where only off diagonal terms with $\sigma' = -\sigma$ are non-zero. When a particle is tunnelling between two sites, its momenta is given by the lattice direction $\hat{\boldsymbol{\epsilon}}_a$. Thus for $\hat{\boldsymbol{\mu}} \in \{\hat{\mathbf{x}}, \hat{\mathbf{y}}\}$, we can write

$$p_\mu = \mathbf{p} \cdot \hat{\boldsymbol{\mu}} = p(\hat{\boldsymbol{\epsilon}}_a \cdot \hat{\boldsymbol{\mu}}) \to -i\nabla(\hat{\boldsymbol{\epsilon}}_a \cdot \hat{\boldsymbol{\mu}}). \tag{3.14}$$

With this relation, the spin-flip hopping amplitude can be written

$$s_{i,i+a}^{\sigma,-\sigma} = -i\kappa \left[\hat{\mathbf{x}} \cdot \hat{\boldsymbol{\epsilon}}_a (\sigma_y)^{\sigma,-\sigma} - \hat{\mathbf{y}} \cdot \hat{\boldsymbol{\epsilon}}_a (\sigma_x)^{\sigma,-\sigma} \right], \tag{3.15}$$

where we have introduced the effective Rashba coupling parameter

$$\kappa = \kappa_R \int \mathrm{d}\mathbf{r} W_i^*(\mathbf{r}) \nabla W_{i+a}(\mathbf{r}). \tag{3.16}$$

This is real and independent of the lattice direction, so the spatial asymmetry of SOC is entirely captured by the Pauli matrix elements and projection of the momentum along lattice bonds in the spin-flip hopping amplitude (eq. (3.15)). The SOC part of the Hamiltonian can now be expressed in the Wannier representation as

$$H_{\mathrm{SO}} = \sum_\sigma \sum_{i,a} b_{i,\sigma}^\dagger s_{i,i+a}^{\sigma,-\sigma} b_{i+a,-\sigma} + \mathrm{h.c.} \tag{3.17}$$

Finally we consider the interacting Hamiltonian. Inserting the Wannier expansion along with the component-dependant interaction potential (eq. (2.20) and eq. (2.22)) in the second quantised expression for the interaction gives

$$\begin{aligned} H_{\mathrm{int}} &= \frac{1}{2} \sum_{\sigma\sigma'} \sum_{ijkl} \int \mathrm{d}\mathbf{r}\, \mathrm{d}\mathbf{r}' U_{\sigma\sigma'} \delta(\mathbf{r} - \mathbf{r}') W_i^*(\mathbf{r}) W_j(\mathbf{r}) W_k^*(\mathbf{r}') W_l(\mathbf{r}') b_{i,\sigma}^\dagger b_{j,\sigma} b_{k,\sigma'}^\dagger b_{l,\sigma'} \\ &= \frac{1}{2} \sum_{\sigma\sigma'} \sum_i u_{\sigma\sigma'} b_{i,\sigma}^\dagger b_{i,\sigma} b_{i,\sigma'}^\dagger b_{i,\sigma'}. \end{aligned} \tag{3.18}$$

Due to the small overlap between Wannier functions at neighbouring sites, only terms with $i = j = k = l$ have been included in the sum, and we have introduced the effective on-site interaction parameter

$$u_{\sigma\sigma'} = U_{\sigma\sigma'} \int \mathrm{d}\mathbf{r} |W(\mathbf{r})|^2. \tag{3.19}$$

In the harmonic approximation, this gives the expression (eq. (2.33)) used to discuss the relative strength of interactions.

3.2 The Bose-Hubbard Model

Recombining the terms discussed above, eqs. (3.7), (3.17) and (3.18), we arrive at the tight-binding Hamiltonian for interacting bosons in a triangular lattice potential with spin-orbit coupling

$$\begin{aligned} H = &\sum_{i,a}\sum_{\sigma}\left(-tb^{\dagger}_{i,\sigma}b_{i+a,\sigma} + b^{\dagger}_{i,\sigma}s^{\sigma,-\sigma}_{i,i+a}b_{i+a,-\sigma} + \text{h.c.}\right) \\ &+ \frac{1}{2}\sum_{i}\sum_{\sigma\sigma'}u_{\sigma\sigma'}b^{\dagger}_{i,\sigma}b_{i,\sigma}b^{\dagger}_{i,\sigma'}b_{i,\sigma'} - \sum_{i}\sum_{\sigma}\mu_{\sigma}n_{i,\sigma}, \end{aligned} \tag{3.20}$$

where a component-dependant chemical potential μ_σ has been introduced for completeness. This model is generally known as the Bose-Hubbard Hamiltonian, a model that has been thoroughly investigated. In this section we will review the physical interpretation of the terms and some of the previous work done on the model.

Writing out the sum over $\sigma \in \{\uparrow,\downarrow\}$ in the first term of the Bose-Hubbard Hamiltonian reveals a matrix structure

$$H = \sum_{\langle ij\rangle}\begin{pmatrix} b^{\dagger}_{i,\uparrow} & b^{\dagger}_{i,\downarrow}\end{pmatrix}\begin{pmatrix} -t & s^{\uparrow,\downarrow}_{ij,a} \\ s^{\downarrow,\uparrow}_{ij,a} & -t\end{pmatrix}\begin{pmatrix} b_{j,\uparrow} \\ b_{j,\downarrow}\end{pmatrix} + \frac{1}{2}\sum_{i,\sigma\sigma'}u_{\sigma\sigma'}n_{i,\sigma}(n_{i,\sigma'}-\delta_{\sigma\sigma'}) - \sum_{i,\sigma}\mu_{\sigma}n_{i,\sigma}. \tag{3.21}$$

Diagonal terms are coupled by $-t$ and describe spin-conserving hopping, while the off-diagonal terms describe hopping with spin-flip with amplitude $s^{\sigma,-\sigma}_{ij,a}$. The spin-conserving hopping amplitude is independent of the lattice direction due to the spherical symmetry of the kinetic plus external potential term. Hopping with spin-flip on the other hand, comes from the spin-orbit coupling which is anisotropic in real space. Because the momentum is reversed when $i \leftrightarrow j$, the non spin-conserving hopping amplitude picks up a relative minus-sign. We also require the Hamiltonian to be Hermitian. These requirements give the symmetry relations,

$$s^{\sigma,-\sigma}_{ij,a} = -\left(s^{-\sigma,\sigma}_{ij,a}\right)^{*}, \tag{3.22}$$

$$s^{\sigma,-\sigma}_{ij,a} = -s^{\sigma,-\sigma}_{ji,a}, \tag{3.23}$$

$$s^{\sigma,-\sigma}_{ij,a} = \left(s^{-\sigma,\sigma}_{ji,a}\right)^{*}, \tag{3.24}$$

which can be verified by writing out the terms in eq. (3.15) explicitly. Hermicity also dictates that t is real, which is the case in the harmonic approximation.

3.2.1 Superfluid and Mott insulator regime

The Bose-Hubbard Hamiltonian has become a popular model because it has a purely quantum mechanical phase transition, which was measured experimentally in 2002[74]. The two phases can be understood in terms of the relative magnitude between hopping terms and the on-site interaction. For large hopping amplitudes the kinetic energy of particles is large

compared to the on-site interaction strength, giving rise to a delocalised superfluid phase. In the limit of no on-site interaction, the superfluid ground state can be expressed as

$$|\Psi_{\mathrm{SF}}\rangle \propto \left(\sum_i b_i^\dagger\right)^N |0\rangle, \tag{3.25}$$

where $|0\rangle$ is an empty lattice and N is the total number of particles. This corresponds to an ideal Bose-Einstein condensate, where particles are described by the zero-momentum Bloch state. For a multi-component condensate with several spin-states, interactions between the different components give rise to currents in the lattice. This is described by the drag of one component on the other[75].

At small hopping amplitudes the particles are strongly confined to the lattice sites with small tunnelling rates between them. This will later be referred to as the *strong coupling regime*. When the average on-site occupation number is an integer this gives rise to the localised Mott insulator phase. This phase is defined by incompressiblity

$$\frac{\partial\langle\hat{n}_i\rangle}{\partial\mu} = 0, \tag{3.26}$$

which is a direct consequence of the finite excitation gap associated with with removing or adding a particle. In the limit of zero hopping amplitude, the Mott insulator ground state is given by

$$|\Psi_{\mathrm{MI}}\rangle \propto \prod_i (b_i^\dagger)^{n_i}|0\rangle. \tag{3.27}$$

Additional particles added to the system can move almost freely on top of the Mott insulator background, forming a condensate. Thus adding particles immediately leads to a superfluid state, showing that the Mott insulator only occurs at constant particle numbers.

Excitations in the Mott insulator are associated with hopping processes, and excited states are characterised by the simultaneous creation of an extra particle and a hole. This introduces correlated number-fluctuations in the system, which leads to non-vanishing on-site fluctuations

$$\sigma_i = \left\langle \sqrt{(\hat{n}_i - \langle\hat{n}_i\rangle)^2} \right\rangle. \tag{3.28}$$

In two-dimensional systems these fluctuations can take significant values, even for very small hopping amplitudes[35].

With a multi-component condensate, the Mott insulator ground state becomes massively degenerate. Since the energy difference between hyperfine states is small, any distribution between the different components with integer on-site occupation constitute a Mott insulator. This gives rise to an interesting excitation spectra, determined by the on-site interaction strength between different components and the strength of SOC relative to spin-conserving hopping amplitudes. In the next section we consider energy corrections from such excitations using an effective spin Hamiltonian.

3.3 Strong coupling regime

In the strong coupling regime at half filling, the ground state is the Mott insulator with one boson of either spin at each site. Since the hopping amplitudes are small compared to the on-site interaction, hopping terms can be written as a perturbation[1]. We write the unperturbed Hamiltonian

$$H_0 = \frac{1}{2}\sum_{i,\sigma\sigma'} u_{\sigma\sigma'} n_{i\sigma}(n_{i\sigma'} - \delta_{\sigma\sigma'}), \tag{3.29}$$

and the perturbation as a sum of three hopping terms.

$$H' = \sum_{a=1}^{3} H^a_{\text{hop}} = \sum_{a=1}^{3}\left(\sum_{\langle ij\rangle_a}\sum_{\sigma\sigma'} T^{\sigma,\sigma'}_{ij,a} b^\dagger_{i,\sigma} b_{j,\sigma'}\right), \tag{3.30}$$

where the sum over $\langle ij\rangle_a$ denotes summations over nearest neighbours connected by a vertex with direction a. The matrix elements $T^{\sigma,\sigma'}_{ij,a}$ are given in eq. (3.21), describing on- and off-diagonal hopping along that vertex.

The first-order energy shift from perturbation theory is

$$\Delta E_1 = \langle\Psi_0|H'|\Psi_0\rangle, \tag{3.31}$$

where $|\Psi_0\rangle$ is the Mott insulating ground state. Acting on the ground state with H' moves particles to neighbouring sites, creating a state that is orthogonal to the ground-state. Consequently, the fist order contribution is zero, and second order perturbation theory is needed.

Labelling the excited states of the Mott insulator $|n\rangle$ with energy E_n, the second-order energy shift is

$$\begin{aligned}\Delta E_2 &= \sum_n \frac{\langle\Psi_0|H'|n\rangle\langle n|H'|\Psi_0\rangle}{E_0 - E_n} \\ &= \sum_n \frac{1}{E_0 - E_n}\left(\sum_{a,b=1}^{3}\langle\Psi_0|H^a_{\text{hop}}|n\rangle\langle n|H^b_{\text{hop}}|\Psi_0\rangle\right)\end{aligned} \tag{3.32}$$

As discussed earlier, acting on the ground state with the perturbation creates a site with double boson occupancy next to an empty site in the lattice. Hence, the excited states have one doubly occupied site with two bosons of either equal or opposite spin. The energy difference from the ground state is the two-particle interaction energy from the effective interaction potential given by eq. (2.22)

[1] Most of the derivation done in this section is similar to work done on the same model on a square lattice in [76]. We go through most of the derivation in the same notation, but refer to that text for some of the lengthy calculations.

- Same spin occupancy: $E_0 - E_n = -u_{\sigma\sigma} = -u$.
- Opposite spin occupancy: $E_0 - E_n = -u_{\sigma,-\sigma} = -\lambda u$.

We now divide the space of excited states into two subspaces; the *same species subspace*, $\{|n_s\rangle\}$, containing states with same spin double site occupancy and the *different species subspace*, $\{|n_d\rangle\}$, with opposite spin double occupancy. The second order energy correction then takes the form

$$\Delta E_2 = \sum_{a,b=1}^{3} \left(-\frac{1}{u} \sum_{n_s} \langle \Psi_0 | H^a_{\text{hop}} | n_s \rangle \langle n_s | H^b_{\text{hop}} | \Psi_0 \rangle - \frac{1}{\lambda u} \sum_{n_d} \langle \Psi_0 | H^a_{\text{hop}} | n_d \rangle \langle n_d | H^b_{\text{hop}} | \Psi_0 \rangle \right) \tag{3.33}$$

To investigate the effect of the second order perturbation on the Mott insulator ground state, the energy correction is written in terms of an effective Hamiltonian

$$\Delta E_2 = \langle \Psi_0 | H_{\text{eff}} | \Psi_0 \rangle. \tag{3.34}$$

The effective Hamiltonian is quadratic in the hopping terms, but only some hopping processes give a non-zero contribution to the energy correction. Considering the effect of H_{hop} (eq. (3.30)) on the ground state, only states with same spin occupancy contribute to the first term in eq. (3.33), and similarly states with opposite spin occupancy contribute to the second term. Mathematically, this can be expressed by the projection operators $\mathcal{P}_s$ and $\mathcal{P}_d$, which project states onto the same and different species subspace respectively. In terms of these projection operators, the effective Hamiltonian (eq. (3.34)) can be split into two contributions, one from each subspace

$$H_{\text{eff}} = H^s_{\text{eff}} + H^d_{\text{eff}} = \sum_{a,b=1} \left(-\frac{1}{u} H^a_{\text{hop}} \mathcal{P}_s H^b_{\text{hop}} - \frac{1}{\lambda u} H^a_{\text{hop}} \mathcal{P}_d H^b_{\text{hop}} \right) \tag{3.35}$$

Inserting the expression from eq. (3.30), and letting $r \in \{s, d\}$, the contribution from each subspace can be written out as

$$H^r_{\text{eff}} = \sum_{a,b=1}^{3} \left(-\frac{1}{u_r} \sum_{\langle ij \rangle_a} \sum_{\langle kl \rangle_b} \sum_{\alpha\beta\nu\rho} T^{\alpha,\beta}_{ij,a} T^{\nu,\rho}_{kl,b} b^\dagger_{i,\alpha} b_{j,\beta} \mathcal{P}_r b^\dagger_{k,\nu} b_{l,\rho} \right), \tag{3.36}$$

with $u_s = u$ and $u_d = \lambda u$.

The effective Hamiltonian is evaluated in the ground state, so for any nonzero contribution $H_{\text{eff}}|\Psi_0\rangle$ must be a state with one particle per site. That occurs when $i = l$ and $j = k$, which is only possible for terms with $a = b$. Writing out the matrix structure of $T^{\alpha,\beta}_{ij,a}$, and inserting these constraints on the summation over lattice sites gives

$$H^r_{\text{eff}} = \sum_{a=1}^{3} \left[-\frac{1}{u_r} \sum_{\langle ij \rangle_a} \sum_{\alpha\beta\nu\rho} \left(-\delta_{\alpha\beta} t + \delta_{\alpha,-\beta} s^{\alpha,\beta}_{ij,a} \right) \left(-\delta_{\nu\rho} t + \delta_{\nu,-\rho} s^{\nu,\rho}_{ji,a} \right) b^\dagger_{i,\alpha} b_{j,\beta} \mathcal{P}_r b^\dagger_{j,\nu} b_{i,\rho} \right]. \tag{3.37}$$

Finally, we consider the effect of the projection operator(s) on the different spin-states. In eq. (3.37), the term $b^\dagger_{j,\nu}b_{i,\rho}$ creates a boson of spin ν at site j. The same species subspace projection operator allows this if there is already a boson of spin ν at site j, and similarly the different species subspace projection operator allows this if the boson at site j has spin $-\nu$. Mathematically, this can be expressed as

$$b^\dagger_{i,\alpha}b_{j,\beta}\mathcal{P}_s b^\dagger_{j,\nu}b_{i,\rho} = b^\dagger_{i,\alpha}b_{j,\beta}b^\dagger_{j,\nu}b_{i,\rho}(1-n_{j,-\nu}) = b^\dagger_{i,\alpha}b_{i,\rho}(\delta_{\beta\nu}+b^\dagger_{j,\nu}b_{j,\beta})n_{j,\nu}, \tag{3.38}$$

$$b^\dagger_{i,\alpha}b_{j,\beta}\mathcal{P}_d b^\dagger_{j,\nu}b_{i,\rho} = b^\dagger_{i,\alpha}b_{j,\beta}b^\dagger_{j,\nu}b_{i,\rho}(1-n_{j,\nu}) = b^\dagger_{i,\alpha}b_{i,\rho}(\delta_{\beta\nu}+b^\dagger_{j,\nu}b_{j,\beta})n_{j,-\nu}, \tag{3.39}$$

where the bosonic commutation relations have been used in the second equality.

3.3.1 Effective spin Hamiltonian

In this section we consider the summation over the spin degrees of freedom, and show how the effective Hamiltonian can be represented by the 2x2 Pauli matrices. The two internal states at each lattice site can be represented by spinors

$$|\uparrow\rangle = \begin{pmatrix}1\\0\end{pmatrix}, \qquad |\downarrow\rangle = \begin{pmatrix}1\\0\end{pmatrix}. \tag{3.40}$$

We now compare the effect of the boson operators in eq. (3.38) and eq. (3.39) on the pseudo-spin Hilbert space, with the effect of Pauli matrices on the the spinors. For example:

$$b^\dagger_{i,\uparrow}b_{i,\uparrow}|\uparrow\rangle_i = |\uparrow\rangle_i, \qquad b^\dagger_{i,\uparrow}b_{i,\uparrow}|\downarrow\rangle_i = 0|\downarrow\rangle_i, \tag{3.41}$$

so that in the matrix representation

$$b^\dagger_{i,\uparrow}b_{i,\uparrow} \quad \Rightarrow \quad \begin{pmatrix}1&0\\0&0\end{pmatrix}_i = \frac{1}{2}(1+\sigma^z_i). \tag{3.42}$$

In this notation, σ^z_i is the Pauli matrix acting on the pseudo-spin space of the particle at site i. Similar considerations for the other terms give the relations

$$\begin{aligned} b^\dagger_{i,\uparrow}b_{i,\uparrow} &\Rightarrow \frac{1}{2}(1+\sigma^z_i), & b^\dagger_{i,\downarrow}b_{i,\downarrow} &\Rightarrow \frac{1}{2}(1-\sigma^z_i), \\ b^\dagger_{i,\uparrow}b_{i,\downarrow} &\Rightarrow \frac{1}{2}\sigma^+_i, & b^\dagger_{i,\downarrow}b_{i,\uparrow} &\Rightarrow \frac{1}{2}\sigma^-_i. \end{aligned} \tag{3.43}$$

The operators acting on site j have an extra number operator at the end. This must have the same spin as the left adjacent annihilation operator to give a contribution, otherwise the effect is the same:

$$\begin{aligned} b^\dagger_{j,\uparrow}b_{j,\uparrow}n_{j,\uparrow} &\Rightarrow \frac{1}{2}(1+\sigma^z_j), & b^\dagger_{j,\downarrow}b_{j,\downarrow}n_{j,\downarrow} &\Rightarrow \frac{1}{2}(1-\sigma^z_j), \\ b^\dagger_{j,\uparrow}b_{j,\uparrow}n_{j,\downarrow} &\Rightarrow 0, & b^\dagger_{j,\downarrow}b_{j,\downarrow}n_{j,\uparrow} &\Rightarrow 0, \\ b^\dagger_{j,\uparrow}b_{j,\downarrow}n_{j,\downarrow} &\Rightarrow \frac{1}{2}\sigma^+_j, & b^\dagger_{j,\downarrow}b_{j,\uparrow}n_{j,\uparrow} &\Rightarrow \frac{1}{2}\sigma^-_j, \\ b^\dagger_{j,\uparrow}b_{j,\downarrow}n_{j,\uparrow} &\Rightarrow 0, & b^\dagger_{j,\downarrow}b_{j,\uparrow}n_{j,\downarrow} &\Rightarrow 0. \end{aligned} \tag{3.44}$$

The terms in eq. (3.37) can now be labelled according to hopping process and written out explicitly using the 2x2 matrix representation. There are three different hopping processes:

I) Two hoppings without spin-flip: $\alpha = \beta$, $\nu = \rho$.

II) Two hoppings with spin-flip: $\alpha = -\beta$, $\nu = -\rho$.

III) One hopping with and one without spin-flip: $\alpha = -\beta$, $\nu = \rho$ or $\alpha = \beta$, $\nu = -\rho$.

In total we end up with six terms for each lattice direction a, three for each of the two subspaces. The calculation of each term is done in detail in [76], and with $s_a \equiv s^{\uparrow,\downarrow}_{ij,a}$ the expressions from the two subspaces is:

$$H^s_{\text{eff}} = -\frac{2}{u}\sum_{i,a}\Big[\ \left(t^2 - |s_a|^2\right)\sigma^z_i\sigma^z_{i+a} - t\Re\{s_a\}\hat{\mathbf{y}}\cdot\boldsymbol{\sigma}_i\times\boldsymbol{\sigma}_{i+a} \tag{3.45}$$
$$- t\Im\{s_a\}\hat{\mathbf{x}}\cdot\boldsymbol{\sigma}_i\times\boldsymbol{\sigma}_{i+a} + t^2 + |s_a|^2\Big],$$
$$H^d_{\text{eff}} = -\frac{1}{\lambda u}\sum_{i,a}\Big[t^2\left(\sigma^x_i\sigma^x_{i+a} + \sigma^y_i\sigma^y_{i+a} - \sigma^z_i\sigma^z_{i+a}\right) + |s_a|^2\sigma^z_i\sigma^z_{i+a} \tag{3.46}$$
$$- \Re\{s_a^2\}\left(\sigma^x_i\sigma^x_{i+a} - \sigma^y_i\sigma^y_{i+a}\right) + \Im\{s_a^2\}\left(\sigma^x_i\sigma^y_{i+a} + \sigma^y_i\sigma^x_{i+a}\right)$$
$$+ t^2 + |s_a|^2\Big].$$

The coefficients in these expressions can be expressed by the effective Rashba coupling parameter κ and the spin-conserving hopping amplitude t. To find the dependence on κ, we insert the spin-flip hopping amplitude given in eq. (3.15)

$$s_{a_1} = -\frac{1}{2}\kappa + i\frac{\sqrt{3}}{2}\kappa, \qquad (s_{a_1})^2 = -\frac{1}{2}\kappa^2 - i\frac{\sqrt{3}}{2}\kappa^2, \tag{3.47}$$
$$s_{a_2} = -\kappa, \qquad (s_{a_2})^2 = \kappa^2, \tag{3.48}$$
$$s_{a_3} = -\frac{1}{2}\kappa - i\frac{\sqrt{3}}{2}\kappa, \qquad (s_{a_3})^2 = -\frac{1}{2}\kappa^2 + i\frac{\sqrt{3}}{2}\kappa^2. \tag{3.49}$$

We may now replace the Pauli matrices by spin operators $\mathbf{S}_i = \boldsymbol{\sigma}_i/2$, so that the effective Hamiltonian derived from second order perturbation theory is expressed as an effective spin Hamiltonian

$$H_{\text{eff}} = \sum_{i,a}\left[\sum_{l=x,y,z} J^l_a S^l_i S^l_{i+a} + K_a(S^x_i S^y_{i+a} + S^y_i S^x_{i+a}) + \mathbf{D}_a\cdot(\mathbf{S}_i\times\mathbf{S}_{i+a})\right]. \tag{3.50}$$

Coefficients are given in table 3.1 in units of $4t_0^2/\lambda u$, which we will use as the unit of energy in the remainder of the thesis. We have adopted a parametrisation used in [76][37]

$$t = t_0\cos\alpha, \qquad \kappa = t_0\sin\alpha. \tag{3.51}$$

Table 3.1: Coefficients of the effective spin Hamiltonian in units of $4t_0^2/\lambda u$

$J_1^x = -\frac{1}{4}(3+\cos 2\alpha)$	$J_2^x = -\cos 2\alpha$	$J_3^x = -\frac{1}{4}(3+\cos 2\alpha)$
$J_1^y = -\frac{1}{4}(1+3\cos 2\alpha)$	$J_2^y = -1$	$J_3^y = -\frac{1}{4}(1+3\cos 2\alpha)$
$J_1^z = -(2\lambda-1)\cos 2\alpha$	$J_2^z = -(2\lambda-1)\cos 2\alpha$	$J_3^z = -(2\lambda-1)\cos 2\alpha$
$\mathbf{D}_1 = -\lambda \sin 2\alpha \left(-\frac{\sqrt{3}}{2}\,\hat{\mathbf{x}} + \frac{1}{2}\,\hat{\mathbf{y}}\right)$	$\mathbf{D}_2 = -\lambda \sin 2\alpha\, \hat{\mathbf{y}}$	$\mathbf{D}_3 = -\lambda \sin 2\alpha \left(\frac{\sqrt{3}}{2}\,\hat{\mathbf{x}} + \frac{1}{2}\,\hat{\mathbf{y}}\right)$
$K_1 = \frac{\sqrt{3}}{4}(1-\cos 2\alpha)$	$K_2 = 0$	$K_3 = -\frac{\sqrt{3}}{4}(1-\cos 2\alpha)$

In this representation we can effectively tune the strength of the spin-orbit coupling through the ratio $\kappa/t = \tan\alpha$. The relative magnitude between inter- and intra-component scattering can be tuned through the parameter λ. Furthermore, we consider the spins as classical with unity length, $|\mathbf{S}_i| = 1$, in the remainder of the thesis.

3.3.2 Classification of the terms in the effective spin Hamiltonian

The effective spin Hamiltonian, eq. (3.50), consists of three distinct terms that couple the spins in fundamentally different ways. In this section we consider their physical origin, symmetries and what magnetic textures they give rise to. This serves as a starting point when we explore the zero-temperature phase diagram in $\{\alpha, \lambda\}$-parameter space in chapter 5.

The first term describes a Heisenberg interaction. This originates from exchange interactions only, either two hoppings with spin-flip or two hoppings without. In the absence of SOC, the Heisenberg interaction becomes purely ferromagnetic with easy plane- or easy axis- anisotropy depending on the relative magnitude between inter- and intra-component interaction strengths. When these are equal, $\lambda = 1$, the Heisenberg interaction becomes fully isotropic in spin-space. With non-zero SOC, the Heisenberg coefficients become anisotropic in real space and as the SOC strength increases, some of the Heisenberg coefficients become anti-ferromagnetic as a result of double spin-flip hopping processes.

The second term describes a more exotic coupling, which the author has not seen in any other spin models. In this thesis we will simply refer to it as the "K-coupling". It originates purely from exchange interactions with double spin-flip, and prefers neighbouring spins to be perpendicular in the xy-plane. To explain the origin of the K-coupling further, we consider the lattice symmetry of the effective spin Hamiltonian. The kinetic energy $\propto \mathbf{p}^2$ is rotationally invariant. Furthermore, the external potential generates the triangular lattice potential and is invariant under rotations of $\pi/3$ in the xy-plane. Finally, the spin-orbit coupling is conceptually generated by a uniform electric field in the z-direction and must have rotational invariance in the xy-plane. Effectively, the energy of any lattice configuration is invariant under a rotation of the entire lattice by $\pi/3$ in the xy-plane about any point.

Denoting rotations in the xy-plane by $\mathcal{R}_{xy}(\phi)$ we find:

$$E_{\mathrm{H}}(\{\mathbf{S}_i\}) \neq E_{\mathrm{H}}(\mathcal{R}_{xy}(\pi/3)\{\mathbf{S}_i\}), \tag{3.52}$$

$$E_{\mathrm{K}}(\{\mathbf{S}_i\}) \neq E_{\mathrm{K}}(\mathcal{R}_{xy}(\pi/3)\{\mathbf{S}_i\}), \tag{3.53}$$

$$E_{\mathrm{H+K}}(\{\mathbf{S}_i\}) = E_{\mathrm{H+K}}(\mathcal{R}_{xy}(\pi/3)\{\mathbf{S}_i\}). \tag{3.54}$$

The energy of the Heisenberg- or K-term alone is not invariant, while the combination of the two is. Thus the K-term effectively restores a lattice symmetry broken by the Heisenberg-term. This symmetry does not extend to spin-space, where the Heisenberg- and K-terms are highly anisotropic for $\alpha \neq 0$.

The third term in the effective spin Hamiltonian is a Dzyaloshinskii-Moriya (DM) interaction. It was originally proposed by Igor Dzyaloshinskii as an explanation of weak ferromagnetic behaviour in anti-ferromagnets[77], and later shown by Toru Moriya to originate from spin-orbit coupling in solids[78]. This arises from processes with one spin-flip hopping and one hopping without spin-flip, because all the DM coefficients are $\propto \sin 2\alpha = 2t\kappa$. In the context of spin-systems the DM interaction prefers to cant neighbouring spins so that they are perpendicular, aligning their cross product with the DM-vector $\mathbf{D}_a$. This gives rise to spiral spin-ordering, commonly seen in chiral magnets with DM-interaction[79, 80]. We also note that the DM-coefficients have large magnitude for $\alpha \simeq \pi/4$.

Because the DM-interaction arises from spin-orbit coupling we anticipate that the energy invariant under lattice rotations

$$E_{\mathrm{DM}}(\{\mathbf{S}_i\}) = E_{\mathrm{DM}}(\mathcal{R}_{xy}(\pi/3)\{\mathbf{S}_i\}), \tag{3.55}$$

which can be verified explicitly. Furthermore, the cross-product between neighbouring spins depends only on the angle between them. From this we obtain a symmetry in spin-space where the DM-term is invariant under spin-rotations in the plane perpendicular to the DM-vector.

3.3.3 K-coupling as an off-diagonal compass coupling

The effective spin Hamiltonian (eq. (3.50)) can alternatively be written on the form

$$H_{\mathrm{eff}} = \sum_{i,a} \left[J\mathbf{S}_i \cdot \mathbf{S}_{i+a} + \mathbf{D}_a \cdot (\mathbf{S}_i \times \mathbf{S}_{i+a}) + \sum_{k,l} S_i^k \Gamma_a^{kl} S_{i+a}^l \right] \tag{3.56}$$

where $k, l \in \{x, y, z\}$. Here the first term is a fully isotropic Heisenberg interaction with $J = -\cos 2\alpha = -(t^2 - \kappa^2)$, generated by spin-conserving hoppings and double spin-flip hopping processes. The second term describes the DM interaction similarly to before. The final term describes a spin-anisotropic interaction of a compass-model type[81], with coefficients given in table 3.2. Compass models have been researched lately in relation to Kitaev's honeycomb-model of a spin-liquid, arising from geometric frustration, although in that model the interaction is on the form $S_i^k \Gamma_k S_{i+k}^k$[82]. All the compass coefficients in the xy-plane

Table 3.2: Non-zero compass coefficients of the second effective spin Hamiltonian in units of $4t_0^2/\lambda u$

$\Gamma_1^{xx} = -\frac{3}{4}(1-\cos 2\alpha)$	$\Gamma_2^{xx} = 0$	$\Gamma_3^{xx} = -\frac{3}{4}(1-\cos 2\alpha)$
$\Gamma_1^{yy} = -\frac{1}{4}(1-\cos 2\alpha)$	$\Gamma_2^{yy} = -(1-\cos 2\alpha)$	$\Gamma_3^{yy} = -\frac{1}{4}(1-\cos 2\alpha)$
$\Gamma_1^{zz} = -2(\lambda-1)\cos 2\alpha$	$\Gamma_2^{zz} = -2(\lambda-1)\cos 2\alpha$	$\Gamma_3^{zz} = -2(\lambda-1)\cos 2\alpha$
$\Gamma_1^{xy} = \Gamma_1^{yx} = \frac{\sqrt{3}}{4}(1-\cos 2\alpha)$	$\Gamma_1^{xy} = \Gamma_1^{yx} = 0$	$\Gamma_1^{xy} = \Gamma_1^{yx} = -\frac{\sqrt{3}}{4}(1-\cos 2\alpha)$

are $\propto (1-\cos 2\alpha) = 2\kappa^2$, so in-plane anisotropy here arises from SOC. Similarly the out-of-plane anisotropy is $\propto \lambda(t^2-\kappa^2)$ and arises from the spin-anisotropy of the two-particle interaction.

In this notation, the spatial symmetry of the spin-anisotropic compass term can be visualised in an intuitive way. We define $\hat{\boldsymbol{\epsilon}}_{a\perp}$ as the clockwise perpendicular unit-vector to each lattice direction $\hat{\boldsymbol{\epsilon}}_a$, shown in fig. 3.1. These are parallel to the DM-vectors. The compass interaction can now be written

$$\sum_{i,a}\sum_{k,l} S_i^k \Gamma_a^{kl} S_{i+a}^l = \sum_{i,a} \Gamma(\mathbf{S}_i \cdot \hat{\boldsymbol{\epsilon}}_{a\perp})(\mathbf{S}_{i+a} \cdot \hat{\boldsymbol{\epsilon}}_{a\perp}) + \Gamma^{zz} S_i^z S_{i+a}^z, \tag{3.57}$$

with $\Gamma = -(1+\cos 2\alpha)$ and Γ^{zz} given in table 3.2. Since $\mathcal{R}_{xy}(\pi/3)\hat{\boldsymbol{\epsilon}}_{a_1\perp} = \hat{\boldsymbol{\epsilon}}_{a_2\perp}$ etc, this term clearly has the xy-plane lattice symmetry.

All of the calculations were done in terms of the K-coupling version of the spin Hamiltonian (eq. (3.50)), but we have chosen to include this form because it shows how the K-coupling is merely an off-diagonal spin-anisotropic term for exchange hopping processes with mixed momentum components.

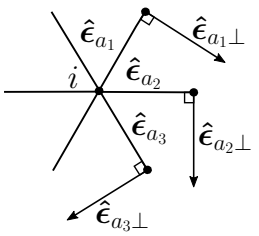

Figure 3.1: Visualisation of the rotational symmetry of the anisotrop compass coupling.

3.3.4 Fourier transform

When analysing the zero temperature ground states in chapter 5, incommensurate phases are simpler to analyse in Fourier space. To that end we derive the Fourier transform of the effective spin Hamiltonian eq. (3.50). With spins transforming as

$$\mathbf{S}_{\mathbf{q}} = \frac{1}{\sqrt{N}} \sum_i \mathbf{S}_i e^{i\mathbf{q}\mathbf{r}_i}, \qquad \mathbf{S}_i = \frac{1}{\sqrt{N}} \sum_{\mathbf{q}} \mathbf{S}_{\mathbf{q}} e^{-i\mathbf{q}\mathbf{r}_i}, \tag{3.58}$$

we end up with the Fourier transformed Hamiltonian

$$\begin{aligned} H = \sum_{\mathbf{q},a} \Bigg[\sum_{l=x,y,z} J_a^l S_{\mathbf{q}}^l S_{-\mathbf{q}}^l \cos(\mathbf{q}\cdot\boldsymbol{\epsilon}_a) + K_a (S_{\mathbf{q}}^x S_{-\mathbf{q}}^y + S_{\mathbf{q}}^y S_{-\mathbf{q}}^x) \cos(\mathbf{q}\cdot\boldsymbol{\epsilon}_a) \\ + i\mathbf{D}_a \cdot (\mathbf{S}_{\mathbf{q}} \times \mathbf{S}_{-\mathbf{q}}) \sin(\mathbf{q}\cdot\boldsymbol{\epsilon}_a) \Bigg]. \end{aligned} \tag{3.59}$$

The complete derivation is given in chapter A.

Chapter 4

Monte Carlo

Monte Carlo is a popular numerical method used commonly in many-particle physics problems. In this chapter we go through the underlying theoretical framework and some important concepts within Monte Carlo simulations[83], and show how we may apply these to our spin-model. As a starting point we review some basic statistical mechanics in the canonical ensemble[84].

4.1 Statistical mechanics

Statistical mechanics is based on the idea that any macroscopic quantity of a given system can be extracted from only microscopic degrees of freedom. Consider a general many-particle system described by a Hamiltonian $H[\Psi]$, in a given configuration Ψ, specified by the microscopic degrees of freedom. The probability of finding the system in this configuration is

$$p[\Psi] = \frac{1}{\mathcal{Z}} e^{-\beta H[\Psi]}, \tag{4.1}$$

where $\beta = 1/T$ is the inverse temperature. This gives the *canonical probability distribution* of the system. The normalisation factor is called the *partition function* and is calculated by integrating over the Boltzmann weight of all possible configurations

$$\mathcal{Z} = \int \mathcal{D}\Psi e^{-\beta H[\Psi]}. \tag{4.2}$$

Formally this is written as a functional integral over the configuration space because Ψ is generally a function of microscopic variables in the system. The partition function is related to the Helmholtz free energy by

$$F = -\frac{1}{\beta} \ln \mathcal{Z}, \tag{4.3}$$

Using the partition function and the canonical probability distribution, we may calculate the expectation value of physical quantities. Denoting the value of some observable for a given configuration by $\mathcal{O}[\Psi]$, the expectation value is

$$\langle \mathcal{O} \rangle = \int \mathcal{D}\Psi p[\Psi]\mathcal{O}[\Psi] = \frac{1}{\mathcal{Z}} \int \mathcal{D}\Psi \mathcal{O} e^{-\beta H}. \tag{4.4}$$

This expectation value is called the *thermal average* for a temperature specified by β. For most common observables, simpler expressions for the thermal average can be derived directly from eq. (4.4). For example, when there is no explicit temperature-dependence in the Hamiltonian, the internal energy is simply the thermal average of said Hamiltonian

$$U = \langle H \rangle = \frac{1}{\mathcal{Z}} \int \mathcal{D}\Psi H e^{-\beta H} = -\frac{1}{\mathcal{Z}} \frac{\partial \mathcal{Z}}{\partial \beta} = -\frac{\partial}{\partial \beta} \ln \mathcal{Z}, \tag{4.5}$$

given entirely by $\mathcal{Z}$.

Since most thermal averages can be directly calculated from the partition function this becomes a central quantity in statistical mechanics. The only problem is that the partition function is intrinsically difficult to compute in most cases because the space of possible configurations can be very large.

4.2 General Monte Carlo methods

The concept of Monte Carlo algorithms is very general and can be applied to problems in various fields. As an introductory example, consider the integral of some complicated function $f(x)$ that must be approximated numerically. In a simple Monte Carlo algorithm we could estimate the area under the graph by spreading N points randomly inside a square of size $h(b-a)$ fully encapsulating the graph. The value of the integral would then be approximated by the fraction of points, N_A/N, that end up below the graph

$$A = \int_a^b \mathrm{d}x f(x) \simeq \frac{N_A}{N}(b-a)h. \tag{4.6}$$

In the same manner we might attempt to measure observables of our spin Hamiltonian by simply picking out a large but finite number of random spin-configurations and calculate the thermal average in these configurations using eq. (4.4) with a discrete sum. In both cases the answer will become more accurate as we use more sampling points, but the problem arises when most of the points have little or no contribution to the correct answer. For example, the integral might have its main contribution from a very small interval in x, so that most of the sampling points are a waste of computational time.

4.2.1 Importance sampling and Markov chains

To avoid sampling from configurations with low probability, the concept of *importance sampling* is introduced. The general idea is to derive a scheme that only samples points with high statistical weight, making the convergence towards the exact result faster.

In statistical mechanics, the configurations are distributed according to the canonical probability distribution introduced in eq. (4.1). Drawing configurations from it directly is not possible, but it can be used to obtain the transition probabilities between configurations. To that we consider a general stochastic process with steps $t_1, t_2, t_3...$ for a system with a finite number of configurations $\{\Psi_n\}$, and denote the configuration at step t by X_t. Now,

consider the conditional probability that $X_t = \Psi_n$. If this probability only depends on the previous configuration in the chain, X_{t-1}, it is called a Markov process and the conditional probability can be interpreted as a transition probability:

$$W_{nm} = W(\Psi_n \to \Psi_m) = P(X_t = \Psi_m | X_{t-1} = \Psi_n). \tag{4.7}$$

Because W_{nm} is a probability it must satisfy

$$W_{nm} \geq 0, \qquad \sum_m W_{nm} = 1. \tag{4.8}$$

From this we can construct the total probability of finding the system in configuration Ψ_m at step t in the chain, in the form of a recursive relation

$$P(X_t = \Psi_m) = W_{nm} P(X_{t-1} = \Psi_n). \tag{4.9}$$

We now introduce the master equation for Markov chains. If t is considered as a continuous time variable rather than a discrete one, the rate of change in the probability that the system is in configuration m at time t can be written

$$\frac{\mathrm{d}}{\mathrm{d}t} P(X_t = \Psi_m) = \sum_n W_{nm} P(X_t = \Psi_n) - \sum_n W_{mn} P(X_t = \Psi_m), \tag{4.10}$$

which is the probability of moving into configuration m minus the probability of moving out of that configuration. The true probability of state m occurring at time t is given by the canonical distribution (eq. (4.1)), which is stationary in thermal equilibrium. Thus we require that our Markov chain probabilities are are also stationary

$$\frac{\mathrm{d}}{\mathrm{d}t} P(X_t = \Psi_m) = 0. \tag{4.11}$$

Inserting this into eq. (4.10) and requiring that it is satisfied term by term in the sum over n, we obtain the *detailed balance* relation:

$$W_{nm} P(X_t = \Psi_m) = W_{mn} P(X_t = \Psi_n) \tag{4.12}$$

4.2.2 Ergodicity and local energy minimas

The principle of ergodicity dictates that all configurations of the system should be reachable from any starting configuration in the Markov chain. In a complex system, configuration space is usually large and we might have several local minimas located far from the global minima. If the Monte Carlo algorithm "gets stuck" in a local minima it leads to improper sampling that does not capture the proper dynamics of the system.

Ergodicity is closely related to phase transitions with *symmetry breaking*. Consider for example an easy axis ferromagnet. At high temperatures the spins fluctuate, whereas the zero temperature configuration is one with all spins up or down. For a non-ergodic algorithm starting from a random high temperature configuration, we might end up with domains

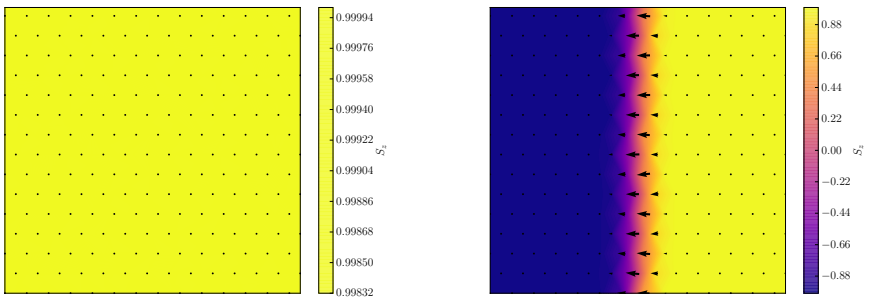

(a) **(b)**

Figure 4.1: Ground state configuration of an easy axis ferromagnet, without (a) and with (b) a domain wall.

where all the spins point up and other domains with spins pointing down separated by *domain walls*. Since the domain walls have an associated energy cost compared to the uniform groundstate configuration, this is a local minima.

In general the question of ergodicity has a complex dependence on the symmetries of the system under consideration, and consequently there is not one "master Monte Carlo algorithm" that works well for all systems. In the next section we present the Metropolis-Hastings algorithm which has a neat mechanism for enforcing ergodicity, but we still need to consider the possibility of domain walls when interpreting results.

4.3 The Metropolis-Hastings algorithm

Introduced by Hastings[85] based on earlier work by Metropolis[86], this is a general algorithm that enforces the two crucial requirements of detailed balance and ergodicity. In the Metropolis-Hastings algorithm, the transition probabilities are written

$$W_{nm} = Q_{nm}\alpha_{nm}, \tag{4.13}$$

where Q_{nm} is the probability of selecting configuration m from n, and α_{nm} is the probability of accepting the change. The acceptance probability is chosen to be the ratio between the probabilities of the two configurations, given by the canonical probability distribution. Furthermore, if the probability of the new configuration is higher than old the change is always accepted, so the acceptance probability is written

$$\alpha_{nm} = \min\left(1, \frac{p[\Psi_m]}{p[\Psi_n]}\right) = \min\left(1, e^{-\beta(E_m - E_n)}\right) \tag{4.14}$$

The selection probabilities, Q_{nm}, must be symmetric so that the transition probabilities defined in eq. (4.13) meet the detailed balance condition. Since the acceptance probability

of going to a state with higher energy is always non-zero, the requirement of ergodicity is also met.

We are now in a position to write down the Metropolis-Hastings importance sampling Monte Carlo scheme applied to spins on a lattice:

I) Start from an initial state Ψ_n.

II) Choose a site i on the lattice and change the spin on that site to generate a new state Ψ_m.

III) Calculate the energy difference $\Delta E = E_m - E_n$ between the old state and the proposed new state.

IV) Accept the change if $\log r \leq -\beta \Delta E$, where $r \in [0, 1]$ is a random number.

V) Start from II picking a new site.

The process of selecting a site attempting to change the spin (step II - IV) will be referred to as a *Monte Carlo step*. A *Monte Carlo sweep* consists of one step for each site in the lattice, and we typically use between 10^3 and 10^6 Monte Carlo sweeps for each temperature in the simulations.

4.3.1 Generating new configurations

With a general scheme in place, a method for generating new configurations from the old one is needed. This method needs to fulfil the symmetry requirement on Q_{ij} and ensure ergodicity. We consider classical spins with constant length, $|\mathbf{S}_i| = 1$, described by the azimuthal and polar angles

$$\mathbf{S}_i = \begin{pmatrix} \sin\theta_i \cos\phi_i \\ \sin\theta_i \sin\phi_i \\ \cos\theta_i \end{pmatrix} \qquad \phi_i \in [0, 2\pi), \quad \theta_i \in [0, \pi]. \tag{4.15}$$

To generate a new configuration, we tilt the spin at site i by some set angle θ_R in a direction drawn at random. Formally, this is done by defining a new coordinate system where $\mathbf{S}_i$ coincides with the z-axis. In this coordinate system the proposed new spin can be written

$$\mathbf{S}_R = \begin{pmatrix} \sin\theta_R \cos\phi_R \\ \sin\theta_R \sin\phi_R \\ \cos\theta_R \end{pmatrix}, \qquad \phi_R = \text{rand}[0, 2\pi). \tag{4.16}$$

The new spin in the standard coordinate system, $\mathbf{S}'_i$, is now obtained through the rotation matrices, where the relation between the two coordinate systems is given by the angles of

the spin $\mathbf{S}_i$. Letting $\mathcal{R}_e(\Omega)$ denote rotations of an angle Ω about the axis $\hat{\mathbf{e}}$, the proposed new spin in the original coordinate system is given by

$$\begin{aligned}\mathbf{S}_i' &= \mathcal{R}_z(\phi_i)\mathcal{R}_y(\theta_i)\mathbf{S}_R \\ &= \begin{pmatrix} \cos\theta_i\cos\phi_i & -\sin\phi_i & \sin\theta_i\cos\phi_i \\ \cos\theta_i\sin\phi_i & \cos\phi_i & \sin\theta_i\sin\phi_i \\ -\sin\theta_i & 0 & \cos\phi_i \end{pmatrix} \mathbf{S}_R.\end{aligned} \tag{4.17}$$

This rotarion is visualised in fig. 4.2. It can easily be verified that when $\theta_R = 0$ the spin is unchanged, $\mathbf{S}_i' = \mathbf{S}_i$. Furthermore the spin is equally likely to change in any direction, so the selection probability is symmetric and any configuration can be reached from successive Monte Carlo sweeps.

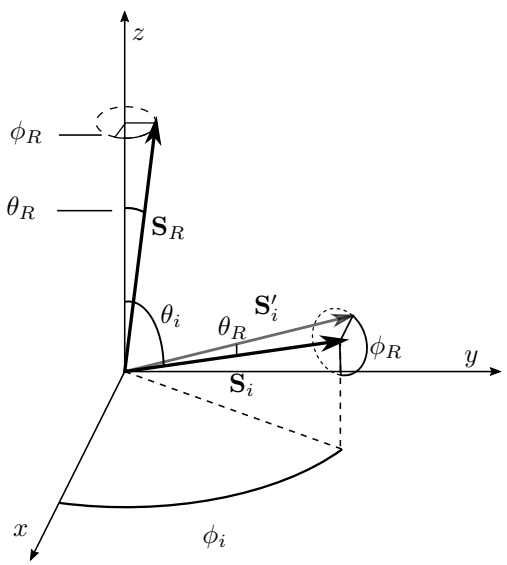

Figure 4.2: Shows the generation of new configurations

In general the update scheme can be chosen quite liberally, as long as it fulfils the requirements of ergodicity and symmetry. A good update scheme is one that finds the most probable configurations, so that we minimise the number of unsuccessful update attempts. In nearest neighbour models a local update scheme – such as the one we use – works well because the energy difference between successive configurations in the chain is small. One big pitfall here is choosing the set angle θ_R too small, so that the algorithm has no way of escaping from a local minima. In addition very small updates can lead to highly correlated configurations in our Markov chain.

4.3.2 Thermalisation

In simulations we typically start from a completely random configuration. Depending on the temperature in the system, this configuration might have high or low probability. From the canonical probability distribution eq. (4.1), we see that for high temperatures (low β) the dependence of the the probability on the energy is suppressed and all states have relatively equal probability. As the temperature is decreased, low energy configurations become more probable.

Thermalisation is the process of allowing the system to reach a configuration near thermal equilibrium through successive Monte Carlo sweeps. The number of sweeps required to reach thermal equilibrium depend on the temperature of the system, and in fig. 4.3 we see a thermalisation process for the Heisenberg model for three different temperatures. For high temperatures, the thermalisation process is faster because more configurations have equal probability, while for lower temperatures its slightly slower.

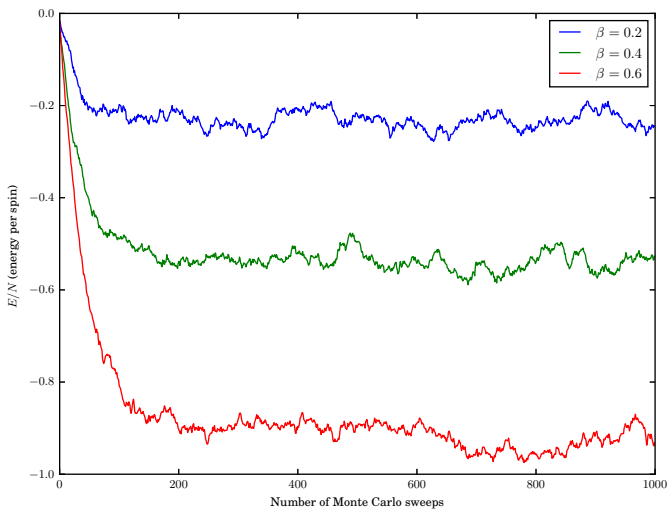

Figure 4.3: Thermalisation from a random configuration at three different temperatures for the Heisenberg model in a 64x64 lattice.

In simulations we want to capture the dynamics of the system in thermal equilibrium, drawing only configurations that are "physical" in the sense that they would occur in a real system at that temperature. Thus, for each temperature we make a number of thermalisation sweeps before observables are measured. From fig. 4.3 we can see that ~ 200 sweeps are enough to properly thermalise this particular system. The number of thermalisation sweeps needed might be higher for more complicated models or lower temperatures, but by monitoring the internal energy we can check that the system is properly thermalised in

simulations.

4.3.3 Monte Carlo annealing

An important part of this thesis is exploring the ground state magnetic textures of the effective spin Hamiltonian derived in chapter 3. At zero temperature ($\beta \to \infty$), a system in thermal equilibrium is the ground state. Starting from a random configuration, the system must then be thermalised for some very high value of β to obtain the ground state. The pitfall here is that at zero temperature only updates with lower energy are accepted in the Metropolis Hastings algorithm. Starting from a random configuration, there is therefore no guarantee that the thermalised system is not a local minima.

Annealing is a scheme where – starting from a high temperature random configuration – the system is eased into the ground state by step-wise thermalisation at incrementally lower temperatures. This decreases the chance of ending up in a local minima, but there is still no guarantee. Furthermore, annealing does not fully prevent the occurrence of domain walls, which are especially prominent in ground state textures with high anisotropy. Consequently, several annealing simulations are done to ensure that we obtain the true ground state.

In all of the simulations periodic boundary conditions are used. These are implemented by the torus topology, shown in fig. 4.4. With periodic boundary conditions and finite size effects, the ground states we obtain will always appear fully ordered if such order exists. Whether this ordering occurs in an infinitely large systems is another question, discussed more in section 4.5 and chapter 6.

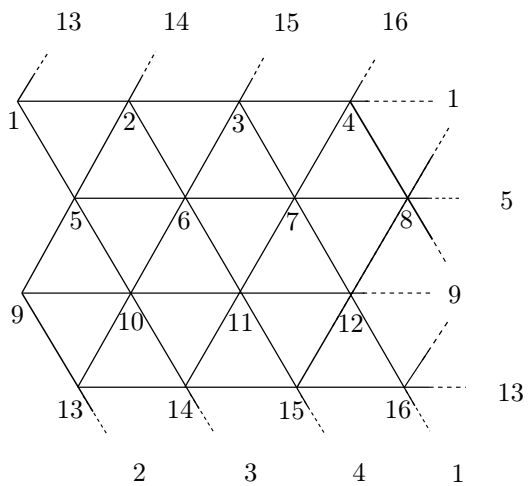

Figure 4.4: 4x4 triangular lattice with periodic boundary conditions.

4.4 Observables

In the annealing process, not many observables are needed. To confirm that the annealing process goes smoothly we measure the internal energy, given by the thermal average of the effective spin Hamiltonian (eq. (3.50)). In addition we sample the magnetic structure factor of the fully annealed zero temperature state. When considering thermal effects and ordering, we sample the helicity modulus.

4.4.1 Magnetic structure factor

The correlation between spins at sites i and j is given by the spin-spin correlation function

$$G(i,j) = \langle \mathbf{S}_i \cdot \mathbf{S}_j \rangle = G(\boldsymbol{\delta}), \tag{4.18}$$

where $\boldsymbol{\delta} = \mathbf{r}_i - \mathbf{r}_j$. Inserting the Fourier transform introduced in eq. (3.59) gives the *magnetic structure factor*

$$G(\mathbf{q}) = \frac{1}{N} \sum_{\boldsymbol{\delta}} e^{i\mathbf{q}\cdot\boldsymbol{\delta}} G(\boldsymbol{\delta}). \tag{4.19}$$

This shows the ordering of magnetic ground state phases in a simple way. Often, complicated magnetic ordering in real space is characterised by simple delta function-like maximas in the magnetic structure factor for some vector $\mathbf{q}$. For example the XY- and Z-ferromagnets are characterised by a maxima at the centre of the Brilloine zone $\mathbf{q} = \mathbf{0}$, while stripe and spiral phases are characterised by two symmetric maximas $\pm\mathbf{q}_0$. There also exist more complex phases characterised by several several distinct points in Fourier space. The magnetic structure factor is in other words directly related to the periodicity and symmetries of the magnetic ordering, and consequently it can be used to characterised the ground state textures obtained by Monte Carlo methods. This is especially useful when the results are obscured in real space by the presence of domain walls.

In annealing simulations, the structure factor is only sampled for the final configuration. Since we assume that the global minima has been reached, there are no fluctuations in the system and consequently the thermal average in eq. (4.18) becomes an exact expression. Furthermore, the sampling is done starting from all lattice sites but we only sum up until $|\boldsymbol{\delta}| = L/2$ to save computational time. The final result is then the average of the structure factor obtained from each site.

4.4.2 Helicity modulus

In this section we consider two ways of measuring the helicity modulus (spin stiffness) for the Heisenberg and XY-model. Since the XY-model is a special case of the Heisenberg model, we will begin by considering a general form of the Heisenberg Hamiltonian

$$H = \sum_{i,a} \left(J_a^x S_i^x S_{i+a}^x + J_a^y S_i^a S_{i+a}^y + J_a^z S_i^z S_{i+a}^z \right). \tag{4.20}$$

where negative/positive coupling constants correspond to a ferromagnetic/anti-ferromagnetic spin model.

The helicity modulus measures the response of the spins to an imposed twist δ_μ along a direction $\hat{\boldsymbol{\mu}}$ in the system. It is defined as the second order derivative of the Helmholtz free energy with respect to an infinitesimal twist

$$\Upsilon_\mu = \left.\frac{\partial^2 F[\delta_\mu]}{\partial \delta_\mu^2}\right|_{\delta_\mu=0}. \tag{4.21}$$

Physically, this corresponds to twisting the spins at one boundary of the system by an angle δ_μ about some axis, while keeping the spins at the opposite boundary fixed. Inserting the expressions for the free energy, eq. (4.3), and the partition function, eq. (4.2), gives the expression

$$\Upsilon_\mu = \left[\beta\left\langle \frac{\partial H}{\partial \delta_\mu}\right\rangle^2 + \left\langle \frac{\partial^2 H}{\partial \delta_\mu^2}\right\rangle - \beta\left\langle \left(\frac{\partial H}{\partial \delta_\mu}\right)^2\right\rangle\right]\Bigg|_{\delta_\mu=0}. \tag{4.22}$$

The first term is current-like and should always have expectation value zero in the Mott-insulator. Thus we will simply set it to zero in all coming expressions, but numerically it is used to check the validity of results.

Twist about three perpendicular axes

We impose a twist where each spin is rotated about one of the three major axes (xyz). The twist is imposed along the direction $\hat{\boldsymbol{\mu}} \in \{\hat{\mathbf{x}}, \hat{\mathbf{y}}\}$, so that the spins at one boundary are twisted an angle Φ compared to the ones at the opposite boundary. This method has previously been used in [87] and for a similar model in [42]. We use the notation introduced in [42].

To introduce this twist, we consider the polar angle ϕ_i^α of each spin about an axis $\hat{\boldsymbol{\alpha}} \in \{\hat{\mathbf{x}}, \hat{\mathbf{y}}, \hat{\mathbf{z}}\}$. For nearest neighbouring spins on the lattice, we impose the twist shown in fig. 4.5a by letting

$$\begin{aligned}
&\phi_i^\alpha - \phi_{i+a}^\alpha \to \phi_i^\alpha - \phi_{i+a}^\alpha + \Delta\phi_{i,i+a}^\alpha, \\
&\phi_i^\alpha + \phi_{i+a}^\alpha \to \phi_i^\alpha + \phi_{i+a}^\alpha + \Delta\phi_{i,i+a}^\alpha, \\
&\Delta\phi_{i,i+a}^\alpha = \frac{\Phi^\alpha}{L_\mu}|\hat{\boldsymbol{\epsilon}}_a \cdot \hat{\boldsymbol{\mu}}|.
\end{aligned} \tag{4.23}$$

We denote the length of the system along the direction of the twist by L_μ since this is different for the x- and y-direction with an equal amount of spins in both directions on the triangular lattice. Taking α, β, γ to be in cyclic order, the Heisenberg Hamiltonian

(eq. (4.20)) can be written on the form

$$
\begin{aligned}
H &= \sum_{i,a} \left(J_a^\beta S_i^\beta S_{i+a}^\beta + J_a^\gamma S_i^\gamma S_{i+a}^\gamma + J_i^\alpha S_i^\alpha S_{i+a}^\alpha \right) \\
&= \sum_{i,a} \sin\theta_i^\alpha \sin\theta_{i+a}^\alpha \left\{ \frac{1}{2}\left[J_a^\beta + J_a^\gamma\right] \cos(\phi_i^\alpha - \phi_{i+a}^\alpha) + \frac{1}{2}\left[J_a^\beta - J_a^\gamma\right] \cos(\phi_i^\alpha + \phi_{i+a}^\alpha) \right\} \\
&\quad + J_a^\alpha \cos\theta_i^\alpha \cos\theta_{i+a}^\alpha,
\end{aligned}
\tag{4.24}
$$

where θ_i^α is the azimuthal angle in the coordinate system specified by α. Inserting the expression for the twist in eq. (4.23) and differentiating with respect to Φ^α, gives

$$
\begin{aligned}
\Upsilon_\mu^\alpha = &- \frac{1}{L_\mu^2} \left\langle \sum_{i,a} \left(J_a^\beta S_i^\beta S_{i+a}^\beta + J_a^\gamma S_i^\gamma S_{i+a}^\gamma \right) |\hat{\boldsymbol{\epsilon}}_a \cdot \hat{\boldsymbol{\mu}}|^2 \right\rangle \\
&- \frac{\beta}{L_\mu^2} \left\langle \left[\sum_{i,a} \left(J_a^\beta S_i^\gamma S_{i+a}^\beta - J_a^\gamma S_i^\beta S_{i+a}^\gamma \right) |\hat{\boldsymbol{\epsilon}}_a \cdot \hat{\boldsymbol{\mu}}| \right]^2 \right\rangle .
\end{aligned}
\tag{4.25}
$$

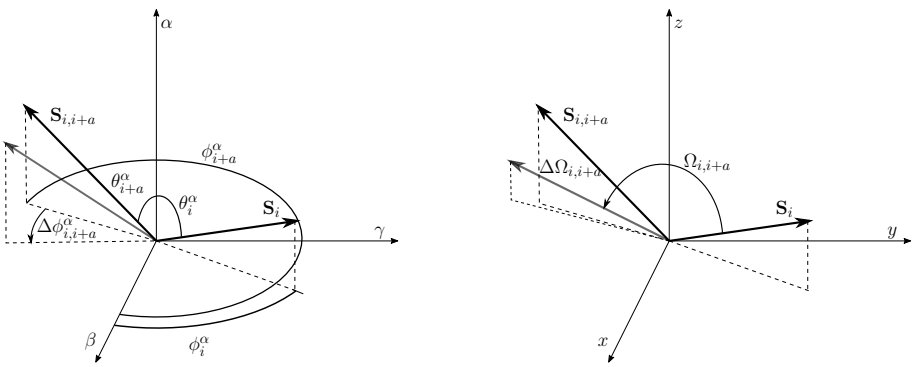

(a) **(b)**

Figure 4.5: Shows the imposed twist around a fixed axis (a), and on the planar angle between the spins (b).

Directly twisting the angle between spins

Instead of twisting the spins about a set axis we now impose a twist where nearest neighbour spins are directly twisted apart, used previously in [43]. We denote the planar angle between two neighbouring spins by $\Omega_{i,i+a}$ and introduce a twist along a direction in the lattice given by

$$
\Omega_{i,i+a} \to \Omega_{i,i+a} + \Delta\Omega_{i,i+a}, \qquad \Delta\Omega_{i,i+a} = \frac{\omega}{L_\mu} |\hat{\boldsymbol{\epsilon}}_a \cdot \hat{\boldsymbol{\mu}}|,
\tag{4.26}
$$

so that the total twist between two boundaries is ω. If the Heisenberg Hamiltonian is assumed to be fully isotropic, it can be written on the form

$$H = \sum_{i,a} J\cos(\Omega_{i,i+a}). \tag{4.27}$$

Inserting the twist defined in eq. (4.26) and differentiating with respect to ω, gives

$$\Upsilon_\mu^\Omega = -\frac{1}{L_\mu^2}\left\langle \sum_{i,a} J\cos(\Omega_{i,i+a})|\hat{\boldsymbol{\epsilon}}_a\cdot\hat{\boldsymbol{\mu}}|^2\right\rangle - \frac{\beta}{L_\mu^2}\left\langle\left[\sum_{i,a} J\sin(\Omega_{i,i+a})|\hat{\boldsymbol{\epsilon}}_a\cdot\hat{\boldsymbol{\mu}}|\right]^2\right\rangle \tag{4.28}$$

XY-model

In the XY-model spins are confined to the xy-plane, so each spin is described by the polar angle ϕ with θ fixed at $\pi/4$. With isotropic interactions in the xy-plane, it can be written

$$H_{\mathrm{XY}} = \sum_{i,a} J(S_i^x S_{i+a}^x + S_i^y S_{i+a}^y) = \sum_{i,a} J\cos(\phi_i - \phi_{i+a}) \tag{4.29}$$

In the axis twisting method, we only have to consider a twist about the z-axis. For the direct twisting method, the planar angle between neighbouring spins is simply the polar angle difference between the two $\phi_{i,i+a} = \phi_i - \phi_{i+a}$. With these identifications we find the helicity modulus for the XY-model

$$\Upsilon_\mu^\phi = -\frac{1}{L_\mu^2}\left\langle \sum_{i,a} J\cos(\phi_{i,i+a})|\hat{\boldsymbol{\epsilon}}_a\cdot\hat{\boldsymbol{\mu}}|^2\right\rangle - \frac{\beta}{L_\mu^2}\left\langle\left[\sum_{i,a} J\sin(\phi_{i,i+a})|\hat{\boldsymbol{\epsilon}}_a\cdot\hat{\boldsymbol{\mu}}|\right]^2\right\rangle, \tag{4.30}$$

where both expressions for the helicity modulus of the Heisenberg model, eq. (4.25) and eq. (4.28), reduce to the same expression.

4.4.3 Helicity modulus with spin-orbit coupling

So far, only ferromagnetic models have been considered. In this section we propose a method to measure the helicity modulus for a spin-model with a DM interaction[1]. We consider a toy model Hamiltonian

$$H = \sum_{i,a} J\mathbf{S}_i\cdot\mathbf{S}_{i+a} + \mathbf{D}_a\cdot(\mathbf{S}_i\times\mathbf{S}_{i+a}), \tag{4.31}$$

where some general DM interaction is given by the vector $\mathbf{D}_a$. The cross product between neighbouring spins can be written in terms of the planar angle introduced in the previous section.

$$\mathbf{S}_i\times\mathbf{S}_{i+a} = \hat{\mathbf{n}}\sin(\Omega_{i,i+a}). \tag{4.32}$$

[1] In the end the results obtained from this method where bad, but it is still included in the thesis because the writer spent considerable time attempting to get this to work.

Denoting the angle between the DM-vector and the cross product by $\Phi_{i,i+a}$, the Hamiltonian can be written

$$H = \sum_{i,a} J\cos(\Omega_{i,i+a}) + |\mathbf{D}_a|\cos(\Phi_{i,i+a})\sin(\Omega_{i,i+a}), \tag{4.33}$$

with angles shown explicitly in fig. 4.6. We now impose a twist by the direct twisting method defined in eq. (4.26). Inserting the twist and differentiating w.r.t. ω, we find

$$\begin{aligned}\Upsilon^{\Omega}_{\mu} = &-\frac{1}{L^2_{\mu}}\left\langle \sum_{i,a}\left[J\cos(\Omega_{i,i+a}) + |\mathbf{D}_a|\cos(\Phi_{i,i+a})\sin(\Omega_{i,i+a})\right]|\hat{\boldsymbol{\epsilon}}_a\cdot\hat{\boldsymbol{\mu}}|^2\right\rangle \\ &-\frac{\beta}{L^2_{\mu}}\left\langle \sum_{i,a}\left\{\left[-J\sin(\Omega_{i,i+a}) + |\mathbf{D}_a|\cos(\Phi_{i,i+a})\cos(\Omega_{i,i+a})\right]|\hat{\boldsymbol{\epsilon}}_a\cdot\hat{\boldsymbol{\mu}}|\right\}^2\right\rangle\end{aligned} \tag{4.34}$$

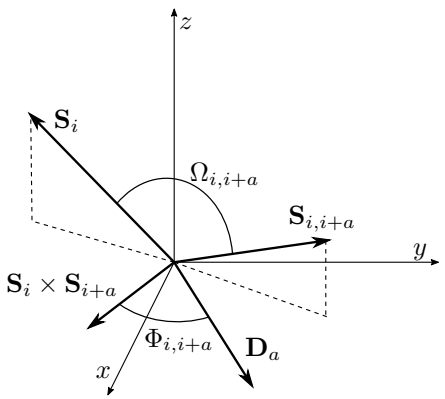

Figure 4.6: Angles used to write out the DM-interaction.

4.5 Quasi-long-range order in lower dimensions

It has been proven rigorously by Mermin and Wagner that there is no long range order in one- or two- dimensional systems with a continuous symmetry[88]. One consequence of this is that the Heisenberg and XY-model discussed in section 4.4.2 never have a finite net magnetisation unlike their three-dimensional counterparts, even at zero temperature. Hohenberg later extended this argument to superconductivity and superfluidity, showing that the expectation value of the superfluid order parameter in a two-dimensional Bose liquid is zero[89]. This begs the question of whether there is a phase transition in lower dimensional magnetic systems.

The work of Berezinskii, Kosterlitz and Thouless later showed that the two-dimensional XY-model exhibits a topological phase transition[90, 91]. This phase transition is characterised by quasi-long-range order (QLRO) in the low temperature phase, where the correlation function exhibits an algebraic decay to zero as opposed to the exponential decay in

the high temperature phase. This can be compared to true long range order seen in three-dimensional systems where the correlation function decays to some constant value in the low-temperature ordered phase. Long range order in two-dimensional systems is destroyed by topological defects, manifested as vortices in superfluids and dislocations in crystals[92]. In the the XY-model, the phase transition is driven by proliferation of vortex-antivortex pairs. Mean-field arguments show that below the transition temperature vortices are confined in pairs. Above the transition temperature free vortices as energetically favoured, allowing the unbinding of vortex-antivortex pairs. These considerations give an upper bound on the critical temperature

$$T_{\mathrm{BKT}} \leq \pi J. \tag{4.35}$$

This is the temperature at which free vortices are no longer energetically allowed in the mean field picture, but more detailed numerical simulations shows that the true critical temperature is lower[93].

Because there is no long range order, the magnetisation can not be used as an order parameter in two-dimensional systems. The order parameter is instead the helicity modulus, defined in section 4.4.2, which is equivalent to the superfluid density. At the critical temperature, the phase transition is characterised by a discontinuous jump in the helicity modulus of universal magnitude[94]

$$\Upsilon(T_{\mathrm{BKT}}) = \frac{2T_{\mathrm{BKT}}}{\pi}. \tag{4.36}$$

We compare this magnitude to our numerical results in chapter 6.

In a truly long range ordered system, phases are characterised by delta-like peaks in the magnetic structure factor for one or several wavevectors, discussed in section 4.4.1. With QLRO, these peaks instead exhibit an exponential decay due to deviations from perfect ordering over long distances. In our numerical simulations on finite lattices, this will always be the case independent of whether we have long range order, QLRO, or no long range order at all. Consequently, when we derive the ground state phase diagram in chapter 5 we will refer to phases as ordered, but generally this is only true in a finite system. In chapter 6 we will consider whether there is actually QLRO in the systems.

Chapter 5

Classical zero temperature phase diagram

In this chapter we present the results from Monte Carlo annealing. We look at the magnetic texture and structure factor of each distinct phase, and get an indication of where in parameter space they are located. Following this we use a variational approach to locate the boundaries between phases more accurately, which leads to a classical zero temperature phase diagram.

5.1 Monte Carlo annealing results

All the annealing simulations are done on a 30×30 lattice. We run simulations for a large part of parameter space $(\alpha, \lambda) \in [0, \pi/2] \times [0.5, 2.0]$, with 20 discrete steps in the α-direction and 31 in the λ-direction. The annealing process is done in four steps starting from a random configuration with $\beta = 0$:

I) 100 increments of 0.05 with $\theta_R = \pi/16$

II) 24 increments of 0.5 with $\theta_R = \pi/16$

III) 16 increments of 5 with $\theta_R = \pi/16$

IV) Two final runs with $\beta = 10^6$ for $\theta_R = \pi/16$ and finally $\theta_R = \pi/32$

Small increments are used at low inverse temperature because the phases typically order for $\beta \in (0.5, 2.0)$, and this is the region where we have to be careful. For each temperature, 4000 thermalisation sweeps are used.

In the next sections we present the magnetic textures obtained for different parts of parameter space. For each phase we show the magnetic texture and structure factor, which is typically representable for a larger region of parameter space around that point.

Ferromagnetic order

For $\alpha = 0$, we obtain 3 different ferromagnetic ground state textures. The xy-ferromagnet (XYFM) phase shown in fig. 5.1a has all spins aligned in the xy-plane and appears for $\lambda < 1$. For $\lambda > 1$ we obtain a z-ferromagnet (ZFM) phase shown in fig. 5.2a with all spins aligned

in the z-direction. Between these two, at $\lambda = 1$, we obtain the fully isotropic Heisenberg ferromagnet shown in fig. 5.3a with spins aligned in some arbitrary direction. The fully isotropic phase is only present for $\lambda = 1$, showing that a slight anisotropy is enough to tilt the spins into the easy plane/along the easy axis. This is consistent with the simple considerations made in section 3.3.2. All three phases are characterised by a simple maxima in the magnetic structure factor at the middle of the Brilloine zone, corresponding to nearest neighbour ordering of periodicity one in the lattice.

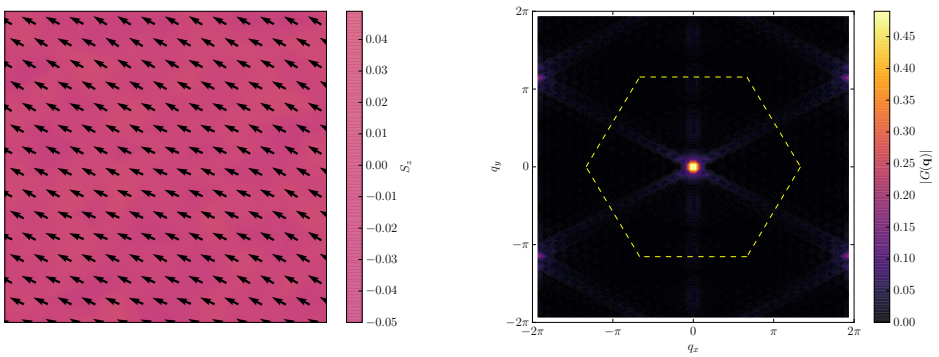

(a) Real space magnetic texure **(b)** Magnetic structure factor

Figure 5.1: XYFM ordering for $\alpha = 0$ and $\lambda = 1.0$.

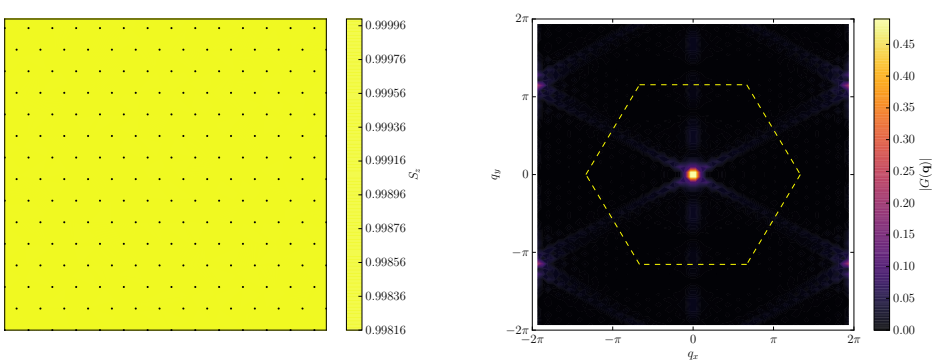

(a) **(b)**

Figure 5.2: ZFM ordering for $\alpha = 0$ and $\lambda = 1.75$

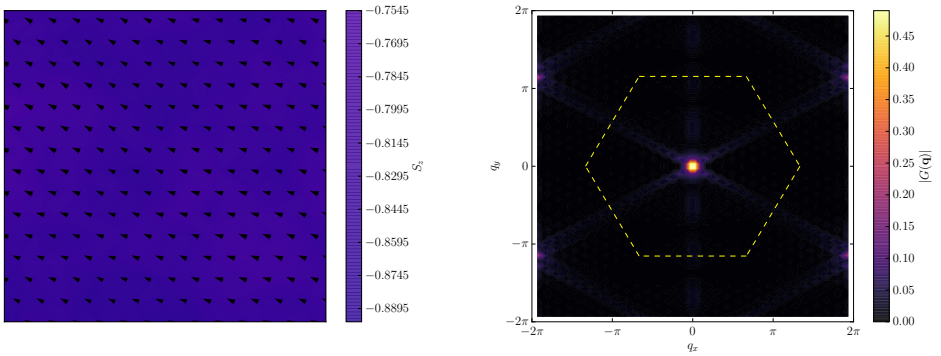

(a) **(b)**

Figure 5.3: Isotropic ferromagnetic ordering for $\alpha = 0$ and $\lambda = 1.0$.

Spiral order

For intermediate values of $\alpha \simeq \pi/4$, we find a variety of co-planar spiral ordering. The spiral phases are labelled by their periodicity along the three different directions in the lattice, and the plane in which they spiral. For example, the spiral-Y (SpY) 4x1x4 phase shown in fig. 5.4a spirals in the yz-plane with periodicity one along the a_2 direction and periodicity four in the other two directions. Similarly, the spiral-X (SpX) phase spirals in the the xz-plane. In addition to simple periodic spirals, we find incommensurate spiral ordering with periodicities that do not fit on the lattice, shown in fig. 5.5a.

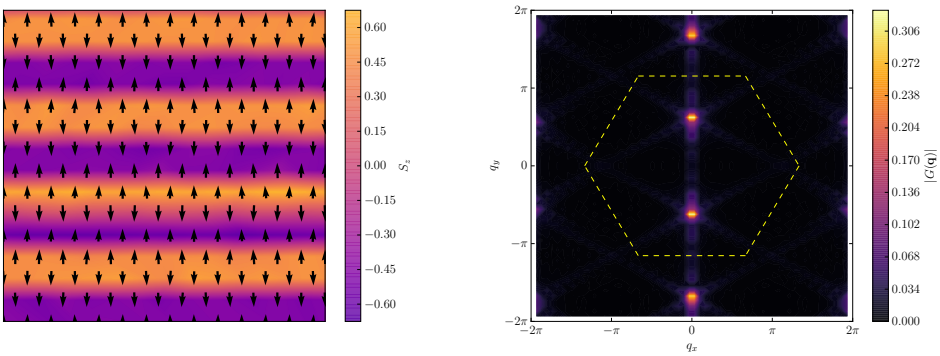

(a) **(b)**

Figure 5.4: SpY 4x1x4 ordering for $\alpha = 0.32\pi$ and $\lambda = 0.5$.

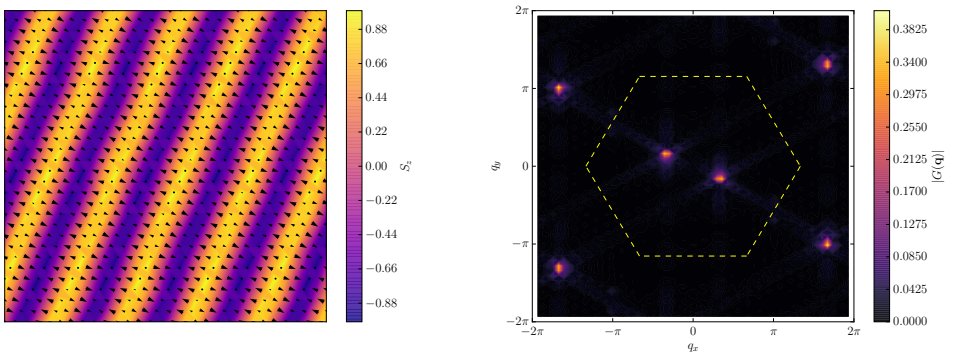

(a) **(b)**

Figure 5.5: Incommensurate SpY ordering for $\alpha = 0.19\pi$ and $\lambda = 1.0$.

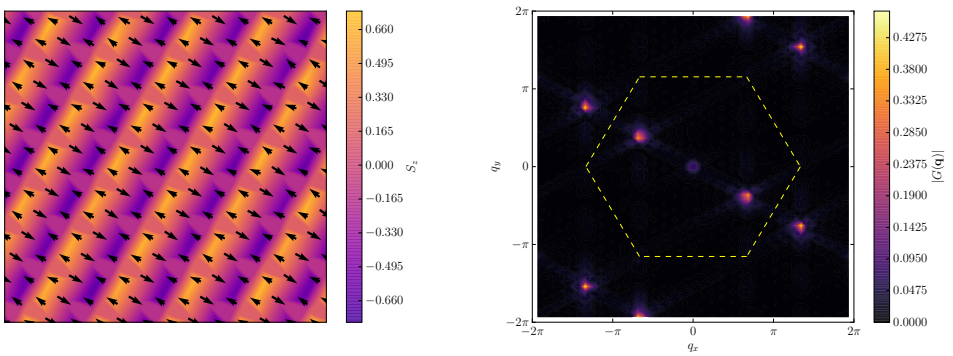

(a) **(b)**

Figure 5.6: SpY 3x1x3 ordering for $\alpha = 0.37\pi$ and $\lambda = 0.85$.

The co-planer spiral phases have one Fourier component given by two symmetric q-vectors along the spiralling direction, shown by the magnetic structure factor of the SpY 4x1x4 phase in fig. 5.4b. The position of the maxima along the y-axis is related to the periodicity of the spiral, where large periodicities correspond maximas close to the centre of the Brillouin zone. We stated in section 3.3.2 that all the phases are invariant under real space rotations of $\pi/3$ in the xy-plane. This symmetry extends to Fourier space, so any spiral phase with magnetic structure factor maxima that can be aligned with the q_y-axis by rotations of $\pi/3$ will be characterised as a SpY phase. For example the spiral phase of period three shown in fig. 5.6a is equivalent to the SpY 3x1x3 phase.

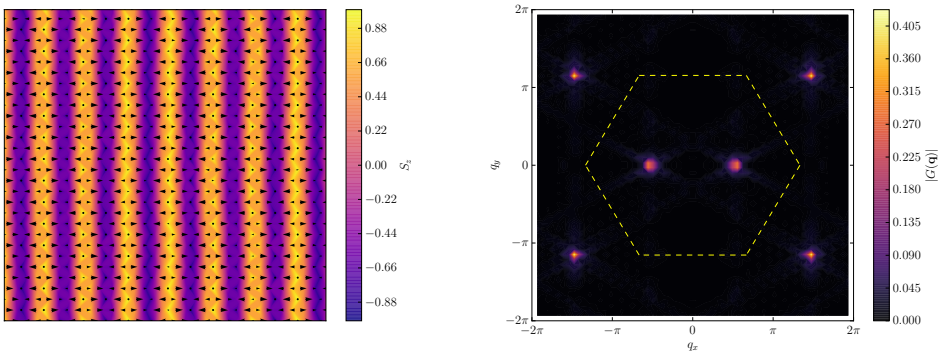

(a) **(b)**

Figure 5.7: Incommensurate SpX ordering for $\alpha = 0.24\pi$ and $\lambda = 2.0$

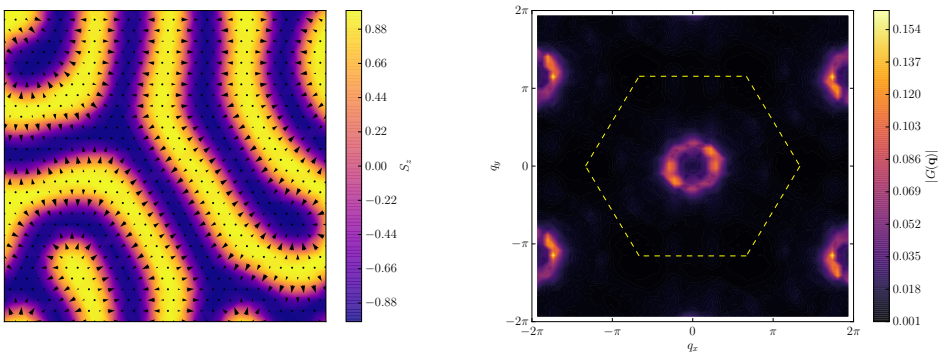

(a) **(b)**

Figure 5.8: Coexistence of spiral ordering in multiple directions for $\alpha = 0.16\pi$ and $\lambda = 1.9$.

We mostly observe SpY ordering in the annealing results, but for high values of $\lambda \to 2$ we also find spiralling in the xz-plane, shown in fig. 5.7a. These are mostly incommensurate and obscured by domain walls, but there is still a clear tendency of SpX ordering in the regime where the intra-component scattering amplitude is large. Close to the Z- and XY-ferromagnetic regimes, we also observe phases with spiralling in multiple directions, shown in fig. 5.8a. In real space this phase looks chaotic, but the magnetic structure factor in fig. 5.8b shows that this phase consist of spiralling order of the same periodicity in almost every direction. In section 5.2 we show that this happens because the SpX and SpY phases have the same energy in this parameter regime.

Antiferromagnetic stripe order

For $\alpha \simeq \pi/2$ and $\lambda < 1.0$, we find a co-linear stripe-Y (StrY) 2x1x2 phase with antiferromagnetic ordering, shown in fig. 5.9a. It is very similar to the SpY ordering discussed in the previous section, with antiferromagnetism along two lattice directions and ferromagnetism along the third. Furthermore, the magnetic structure factor maxima lies at the edge of the Brilloine zone, corresponding to a periodicity of two in the real space lattice along that direction.

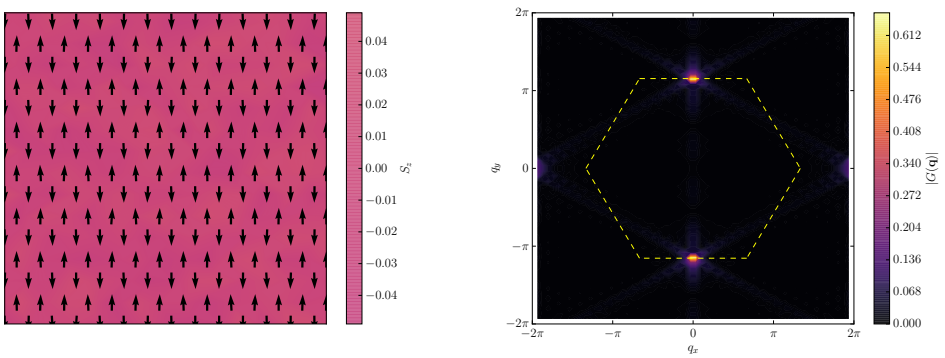

(a) **(b)**

Figure 5.9: StrY 2x1x2 ordering for $\alpha = \pi/2$ and $\lambda = 0.5$.

Vortex phase

For $\alpha \simeq \pi/2$ and $\lambda \simeq 2$ we find a Vortex (VX) phase, shown in fig. 5.10a. This phase consists of vortices with one spin pointing in the z-direction surrounded by spins pointing towards it while slightly canted in the z-direction opposite to the centre spin. The VX phase is a triple q-state, characterised by a maxima at each vertex on the edge of the Brilloine zone shown in fig. 5.10b.

$$\mathbf{q}_2 = \frac{2\pi}{3}\hat{\mathbf{x}} + \frac{2\pi}{\sqrt{3}}\hat{\mathbf{y}}, \qquad \mathbf{q}_2 = \frac{4\pi}{3}\hat{\mathbf{x}}, \qquad \mathbf{q}_3 = \mathbf{q}_2 - \mathbf{q}_1. \tag{5.1}$$

This corresponds to second nearest neighbour ordering along every lattice bond. We observe both negative vortices with all spins pointing inwards such as the one in fig. 5.10a, but also positive vortices with all spins pointing outward shown in fig. 5.11a. This is slightly peculiar, particularly since there are no results with both positive and negative vortices in the same lattice. The variational calculation done in section 5.2 will show explicitly that phases with negative and positive vortices are equivalent, and furthermore that the vortex phase has a continuous symmetry.

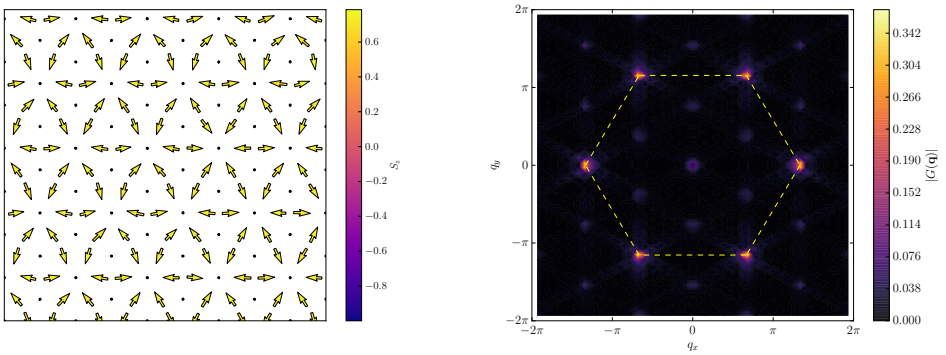

(a) **(b)**

Figure 5.10: Negative VX ordering for $\alpha = \pi/2$ and $\lambda = 1.9$.

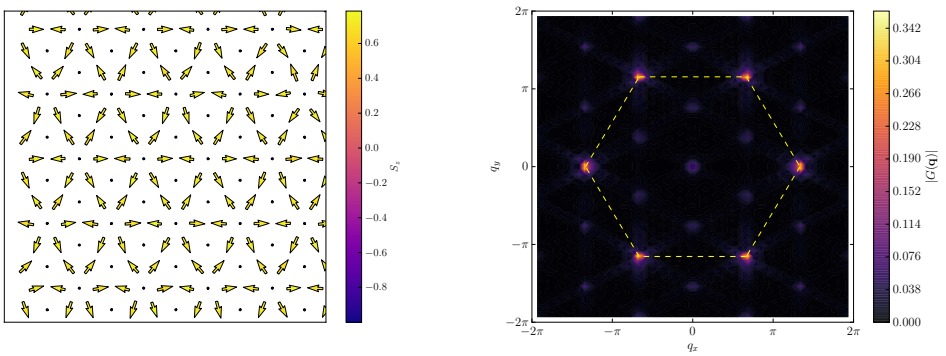

(a) **(b)**

Figure 5.11: Positive VX ordering for $\alpha = \pi/2$ and $\lambda = 1.8$.

Complex spiral ordering

Close to the VX phase we find spiral phases of higher complexity than the simple spirals with ferromagnetism along one lattice direction. The SpY 6x3x6 phase, shown in fig. 5.12a, is located between the stripe and VX phase for $\alpha \simeq \pi/2$ and $\lambda \simeq 1.3$. The magnetic structure factor, shown in fig. 5.12b, has two large maximas along the spiralling direction at the edge of the Brilloine zone, along with weak maximas at the vertices. This corresponds to coexistence between VX and stripe ordering in the form of a spiral phase. As λ increases, the maximas at the vertices become stronger as the SpY 6x3x6 turns into the VX phase.

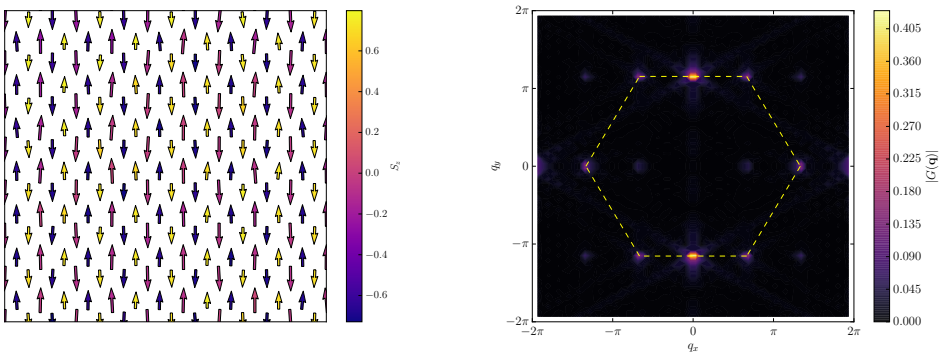

(a) **(b)**

Figure 5.12: SpY 6x3x6 ordering for $\alpha = \pi/2$ and $\lambda = 1.3$.

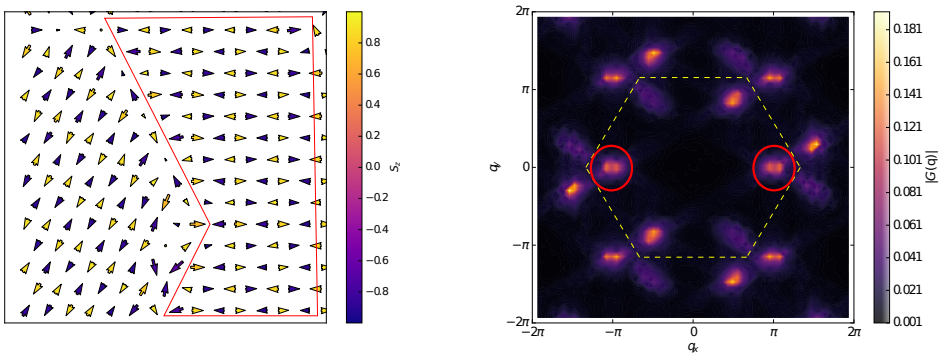

(a) **(b)**

Figure 5.13: SpX 4x2x4 ordering for $\alpha = 0, 39\pi$ and $\lambda = 1.95$.

For $\lambda \simeq 2.0$, between the simple spiral order and the VX phase, we find a SpX 4x2x4 phase shown in fig. 5.13a. In all the annealing results obtained, this phase had several domain walls occurring because of strong antiferromagnetism in the z-direction. In fig. 5.13b, we see that the magnetic structure factor has several strong maxima. The marked ones along the x-direction correspond to the SpX ordering indicated in the real space figure, while the other maximas correspond to the equivalent rotated phase. These are separated by a domain wall.

5.2 Variational phase energies

In this section we compute the energy per spin for variational states based on the Monte Carlo annealing results. This is done by proposing ansatzes for each of the phases introduced in the previous section. The energy of the ansatz phases are computed with the effective spin Hamiltonian, eq. (3.50), and minimised analytically or numerically.

Ferromagnetic order

The easy plane XYFM phase has all spins aligned in the xy-plane, so the ansatz for this phase is $\mathbf{S}_i = (\cos\phi, \sin\phi, 0)$. With all spins aligned there is no contribution from the DM term, and the energy becomes

$$\begin{aligned} E_{\text{XYfm}} &= \sum_a J_a^x \cos^2\phi + J_a^y \sin^2\phi + 2K_a \cos\phi \sin\phi) \\ &= -\frac{3}{2}(1 + \cos 2\alpha), \end{aligned} \tag{5.2}$$

where the cross-term cancels because $K_1 = -K_3$. As expected, the phase is continuously degenerate with energy independent of the angle ϕ.

The easy axis ZFM has all spins aligned in the z-direction, so the ansatz is simply $\mathbf{S}_i = \hat{\mathbf{z}}$. There is only one non-zero term in the effective spin Hamiltonian so the energy is given by

$$E_{\text{Zfm}} = \sum_a J_a^z = -3(2\lambda - 1)\cos 2\alpha. \tag{5.3}$$

Comparing the energies of the XYFM and ZFM shows that they are equal when $\alpha = 0$ and $\lambda = 1.0$, where the effective spin Hamiltonian reduces to the isotropic Heisenberg model.

Commensurate spiral-Y order

We consider commensurate spiral order in the yz-plane. The annealing results revealed a host of different periodicities, so consequently we consider spirals of periodicity up to six. We start by considering the SPY 3x1x3 phase. The ansatz used is shown in figure fig. 5.14a, with one spin fixed along the y-axis and the two other spins given by a variational angle ξ

$$\mathbf{S}_1 = (0, -\cos\xi, \sin\xi), \qquad \mathbf{S}_2 = (0, 1, 0), \qquad \mathbf{S}_3 = (0, -\cos\xi, -\sin\xi). \tag{5.4}$$

The energy of this phase is obtained by summing over the three lattice sites indicated in fig. 5.14b with nearest neighbours given by the periodicity of the phase. We obtain

$$\begin{aligned} E_{\text{SpY3x1x3}} = -\frac{1}{3}\Big\{ &\frac{1}{4}(5 + 3\cos 2\alpha)\cos 2\xi - (1 + 3\cos 2\alpha)\cos\xi \\ &+ \lambda\sqrt{3}\sin 2\alpha \sin 2\xi + 2\lambda\sqrt{3}\sin 2\alpha \sin\xi - \frac{1}{4}(9 + 3\cos 2\alpha)\Big\}, \end{aligned} \tag{5.5}$$

which has to be minimised numerically with respect to the variational angle.

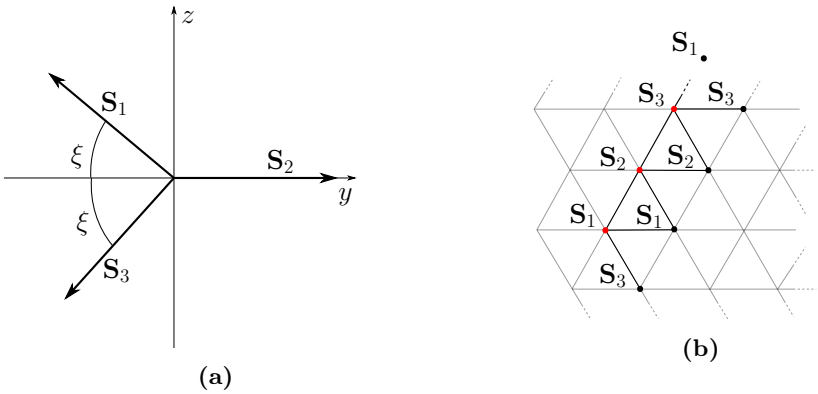

Figure 5.14: Ansatz for the SpY 3x1x3 phase (a), and periodicity of the phase on the lattice (b).

For SpY 4x1x4, we consider an ansatz with four spins drawn an angle ξ away from the z-axis as shown in fig. 5.15a.

$$\begin{aligned} \mathbf{S}_1 &= (0, \sin\xi, \cos\xi), \qquad \mathbf{S}_2 = (0, \sin\xi, -\cos\xi), \\ \mathbf{S}_3 &= (0, -\sin\xi, \cos\xi), \quad \mathbf{S}_4 = (0, -\sin\xi, \cos\xi). \end{aligned} \tag{5.6}$$

Inserting this ansatz into the effective spin Hamiltonian and summing over the four different configurations, we obtain

$$E_{\mathrm{SpY4x1x4}} = -\left\{ \frac{1}{2}\left[1 + (2\lambda - 1)\cos 2\alpha\right] + \frac{1}{2}[(2\lambda - 1)\cos 2\alpha - 1]\cos 2\xi + \sqrt{3}\lambda \sin 2\alpha \sin 2\xi \right\}. \tag{5.7}$$

The minima of an expression of the form $C_1 \cos x + C_2 \sin x$ can be found analytically as $\sqrt{C_1^2 + C_2^2}$. Inserting this relation we find the variation energy to be

$$E_{\mathrm{SpY4x1x4}} = -\left\{ \sqrt{\frac{1}{4}\left[(2\lambda - 1)\cos 2\alpha - 1\right]^2 + 3\lambda^2 \sin^2 2\alpha} + \frac{1}{2}\left[1 + (2\lambda - 1)\cos 2\alpha\right] \right\}, \tag{5.8}$$

where the variational angle is given by

$$\xi = \frac{1}{2} \arctan\left(\frac{-2\sqrt{3}\lambda \sin 2\alpha}{(2\lambda - 1)\cos 2\alpha - 1} \right). \tag{5.9}$$

For the SpY 5x1x5 phase we propose a similar ansatz to the period 3 spiral, shown in fig. 5.15b. The ansatz spins are written

$$\begin{aligned} \mathbf{S}_1 = (0, 1, 0), \quad \mathbf{S}_2 &= (0, \sin\xi_1, -\cos\xi_1), \quad \mathbf{S}_3 = (0, -\sin\xi_2, -\cos\xi_2), \\ \mathbf{S}_4 &= (0, -\sin\xi_2, \cos\xi_2), \quad \mathbf{S}_5 = (0, \sin\xi_1, \cos\xi_1). \end{aligned} \tag{5.10}$$

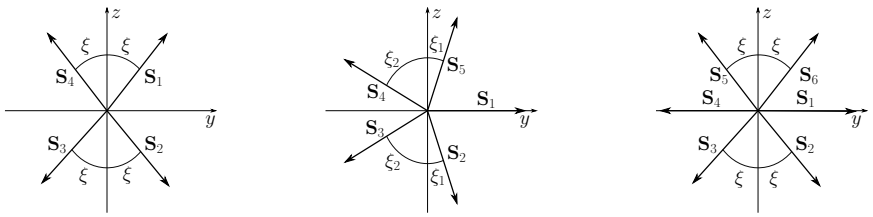

Figure 5.15: Ansatz for the SpY 4x1x4 phase (a), 5x1x5 (b) and 6x1x6 (c).

From these we obtain the variational energy

$$\begin{aligned} E_{\mathrm{SpY5x1x5}} = \frac{1}{5}\Big\{ & 4J_1^y \sin\xi_1 + (J_1^z - J_2^y)\cos 2\xi_1 - 4D_1^x \cos\xi_1 - 4J_1^y \sin\xi_1 \sin\xi_2 \\ & + 4J_1^z \cos\xi_1 \cos\xi_2 - 4D_1^x \sin\xi_1 \cos\xi_2 - 4D_1^x \cos\xi_1 \sin\xi_2 \\ & - (J_1^y + J_2^y)\cos 2\xi_2 - 2D_1^x \sin 2\xi_2 + (3J_2^y + J_1^z + J_1^y)\Big\}, \end{aligned} \tag{5.11}$$

written in terms of the coupling constants (table 3.1) to somewhat shorten the expression. This has to be minimised numerically with respect to the two variational angles.

The final simple commensurate spiral order we consider is the SpY6x1x6. We use an ansatz similar to the period four spiral, shown in fig. 5.15c, with the spins written

$$\begin{aligned} \mathbf{S}_1 &= (0,1,0), & \mathbf{S}_2 &= (0,\sin\xi,-\cos\xi), \\ \mathbf{S}_3 &= (0,-\sin\xi,-\cos\xi), & \mathbf{S}_4 &= (0,-1,0), \\ \mathbf{S}_5 &= (0,-\sin\xi,\cos\xi), & \mathbf{S}_6 &= (0,\sin\xi,\cos\xi). \end{aligned} \tag{5.12}$$

Inserting these into the Hamiltonian gives the variational energy

$$\begin{aligned} E_{\mathrm{SpY6x1x6}} = -\frac{1}{6}\Big\{ & \Big[4(2\lambda-1)\cos 2\alpha - \frac{3}{2}(1-\cos 2\alpha)\Big]\cos 2\xi + 4\sqrt{3}\lambda \sin 2\alpha \cos\xi \\ & + 2\sqrt{3}\lambda \sin 2\alpha \sin 2\xi + 2(1+3\cos 2\alpha)\sin\xi \\ & + 4(2\lambda-1)\cos 2\alpha + \frac{1}{2}(7-3\cos 2\alpha)\Big\} \end{aligned} \tag{5.13}$$

which again has to be minimised numerically.

Incommensurate spiral order

In this section we consider incommensurate spiral phases in Fourier space. We use the Fourier transformed Hamiltonian, eq. (3.59), and assume that there is one contributing wavevector

$\mathbf{q}_0$ with two non-zero contributions $\mathbf{S}_{q_0}$ and $\mathbf{S}_{-q_0}$. The Fourier modes must satisfy Parseval's theorem

$$\sum_q |\mathbf{S}_q|^2 = \sum_i (\mathbf{S}_i)^2. \tag{5.14}$$

Furthermore, we require that Parseval's theorem is satisfied by each component

$$\sum_q |\mathbf{S}_q^a|^2 = \sum_i (\mathbf{S}_i^a)^2. \tag{5.15}$$

In the single mode approximation, using $\mathbf{S}_{q_0} = (\mathbf{S}_{-q_0})^*$, Parseval's theorem can be written

$$|\mathbf{S}_{q_0}|^2 = \frac{N}{2} \tag{5.16}$$

The real space spins satisfy the relation $\mathbf{S}_i \cdot \mathbf{S}_i = S^2 = 1$. Writing this out in terms of the Fourier transform and using Parseval's theorem gives

$$\Re\{\mathbf{S}_{q_0} \cdot \mathbf{S}_{q_0} e^{-2i\mathbf{q}_0 \cdot \mathbf{r}_i}\} = 0. \tag{5.17}$$

When $\mathbf{q}_0$ is incommensurate, the exponential takes different values for each site, so this can only be satisfied for all sites if $\mathbf{S}_{q_0} \cdot \mathbf{S}_{q_0} = 0$.

The ansatz for the incommensurate spiral phases can now be written in terms of a single variational mode

$$\mathbf{S}_{q_0} = \sqrt{\frac{N}{2}} \left(\gamma_x e^{i\phi_x}, \gamma_y e^{i\phi_y}, \gamma_z e^{i\phi_z}\right), \tag{5.18}$$

with constraints on the variational parameters given by Parseval's theorem and the constant spin length condition. In the incommensurate SpY phase, all spins lie in the yz-plane. The component dependant Parseval theorem ,eq. (5.15), then implies that $\gamma_x = 0$. Furthermore, global phase freedom allows us to set $\phi_z = 0$. Using Parseval's theorem and the constant spin length condition, the SpY Fourier component ansatz takes the form

$$\mathbf{S}_{q_0} = \frac{N}{2}\left(0, \frac{1}{\sqrt{2}} e^{i\pi/2}, \frac{1}{\sqrt{2}}\right) \tag{5.19}$$

Inserting this along with a variational wavevector $\mathbf{q_0} = (0, q_0)$ into the Fourier transformed Hamiltonian, eq. (3.59), gives

$$E_{\mathrm{ICSpY}} = -\left\{\sqrt{\left[\frac{1}{4} + \left(2\lambda - \frac{1}{4}\right)\cos 2\alpha\right]^2 + 3\lambda^2 \sin^2 2\alpha} + \frac{1}{2}\left[1 + (2\lambda - 1)\cos 2\alpha\right]\right\}. \tag{5.20}$$

where the magnitude of the wavevector is found analytically to be

$$q_0 = \frac{2}{\sqrt{3}} \arctan\left\{\frac{\sqrt{3}\lambda \sin 2\alpha}{(1 + 3\cos 2\alpha)/4 + (2\lambda - 1)\cos 2\alpha}\right\}. \tag{5.21}$$

We also consider an incommensurate SpX phase, with spins in the xz-plane. Similarly to the SpY phase, we set $\gamma_y = 0$ and $\phi_z = 0$, so the Fourier component becomes

$$\mathbf{S}_{q_0} = \frac{N}{2}\left(\frac{1}{\sqrt{2}}e^{i\pi/2}, 0, \frac{1}{\sqrt{2}}\right) \tag{5.22}$$

With $\mathbf{q_0} = (q_0, 0)$, the variational energy becomes

$$\begin{aligned} E_{\mathrm{ICSpX}} = -\Bigg\{ &\left[\frac{1}{4}(3+\cos 2\alpha) + (2\lambda - 1)\cos 2\alpha\right]\cos(q_0/2) + \lambda \sin 2\alpha \sin(q_0/2) \\ &+ \lambda \cos 2\alpha \cos q_0 + \lambda \sin 2\alpha \sin q_0 \Bigg\}, \end{aligned} \tag{5.23}$$

which is minimised numerically with respect to the wavevector magnitude.

Complex spiral order

In addition to the simple spiral phases with ferromagnetism along one lattice direction, we obtained two spiral phases of higher complexity in the annealing results. Our ansatz for the SpiralY 6x3x6 phase is shown in fig. 5.16a, with the spins written as

$$\begin{aligned} &\mathbf{S}_1 = (0, -\sin\xi_1, \cos\xi_1), \quad \mathbf{S}_2 = (0, \sin\xi_2, \cos\xi_2), \\ &\mathbf{S}_3 = (0, -\sin\xi_3, \cos\xi_3), \quad \mathbf{S}_4 = (0, -\sin\xi_1, \cos\xi_1), \\ &\mathbf{S}_5 = (0, -\sin\xi_2, \cos\xi_2), \quad \mathbf{S}_6 = (0, \sin\xi_3, \cos\xi_3). \end{aligned} \tag{5.24}$$

Inserting these into the spin Hamiltonian and summing over the sites indicated by red dots in fig. 5.16b gives the variational energy

$$E_{\mathrm{SpY6x3x6}} = -\frac{1}{3}\left\{[1 - (1 + 3\cos 2\alpha)]\sum_{i<j}\sin\xi_i \sin\xi_j + 3(2\lambda - 1)\cos 2\alpha \sum_{i<j}\cos\xi_i \cos\xi_j\right\}, \tag{5.25}$$

which is minimised numerically with respect to the three variational angles.

Similarly we consider the SpX 4x2x4 phase, with an ansatz like to the SpY 4x1x4 phase in fig. 5.15a, but with spins in the xz plane and a different periodicity

$$\begin{aligned} &\mathbf{S}_1 = (\sin\xi, 0, \cos\xi), \qquad \mathbf{S}_2 = (\sin\xi, 0, -\cos\xi), \\ &\mathbf{S}_3 = (-\sin\xi, 0, -\cos\xi), \quad \mathbf{S}_4 = (-\sin\xi, 0, \cos\xi). \end{aligned} \tag{5.26}$$

Summing over the four configurations shown in fig. 5.16c, we obtain the energy

$$E_{\mathrm{SpX4x2x4}} = \cos 2\alpha \sin^2\xi + (2\lambda - 1)\cos 2\alpha \cos^2\xi - 2\lambda \sin 2\alpha \cos\xi \sin\xi, \tag{5.27}$$

which again has to be minimised numerically. We observe that for $\alpha > \pi/4$, all three terms have negative signs as expected.

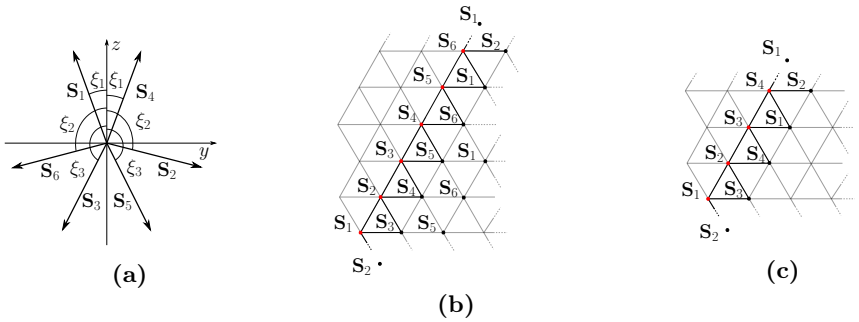

Figure 5.16: Ansatz for the SpY 6x3x6 phase (a), lattice periodicity for the SpX 6x3x6 phase (b) and SpY 4x2x4 phase (c).

Stripe order

The StrY 2x1x2 phase is obtained by considering the ansatz

$$\mathbf{S}_1 = \hat{\mathbf{y}}, \qquad \mathbf{S}_2 = -\hat{\mathbf{y}}, \tag{5.28}$$

with periodicity like the simple spiral phases. Only the Heisenberg y-coupling contributes to the variational energy and we simply obtain

$$E_{\mathrm{StrY}} = \sum_{i=1,2} \sum_{a} J_a^y S_i^y S_{i+a}^y = -\frac{1}{2} + \frac{3}{2}\cos 2\alpha \tag{5.29}$$

The second term becomes negative for $\alpha > \pi/4$, giving an overall negative energy.

Vortex order

The VX phase is built from the periodic repetitions of the pattern shown in fig. 5.17a. Surrounding the middle up/down spin are six spins given by the same angle γ indicated in the figure, with an out-of-plane component given by the angle ξ of opposite sign as the middle spin.

$$\begin{aligned}
\mathbf{S}_0 &= [0, 0, -1], \\
\mathbf{S}_1 &= [\sin\xi\cos\gamma, -\sin\xi\sin\gamma, \cos\xi], \\
\mathbf{S}_2 &= [\sin\xi\cos(\pi/3+\gamma), \sin\xi\sin(\pi/3+\gamma), \cos\xi], \\
\mathbf{S}_3 &= [-\sin\xi\cos(\pi/3-\gamma), -\sin\xi\sin(\pi/3-\gamma), \cos\xi], \\
\mathbf{S}_4 &= [\sin\xi\cos(\pi/3-\gamma), -\sin\xi\sin(\pi/3-\gamma), \cos\xi], \\
\mathbf{S}_5 &= [-\sin\xi\cos(\pi/3+\gamma), \sin\xi\sin(\pi/3+\gamma), \cos\xi], \\
\mathbf{S}_6 &= [-\sin\xi\cos\gamma, -\sin\xi\sin\gamma, \cos\xi].
\end{aligned} \tag{5.30}$$

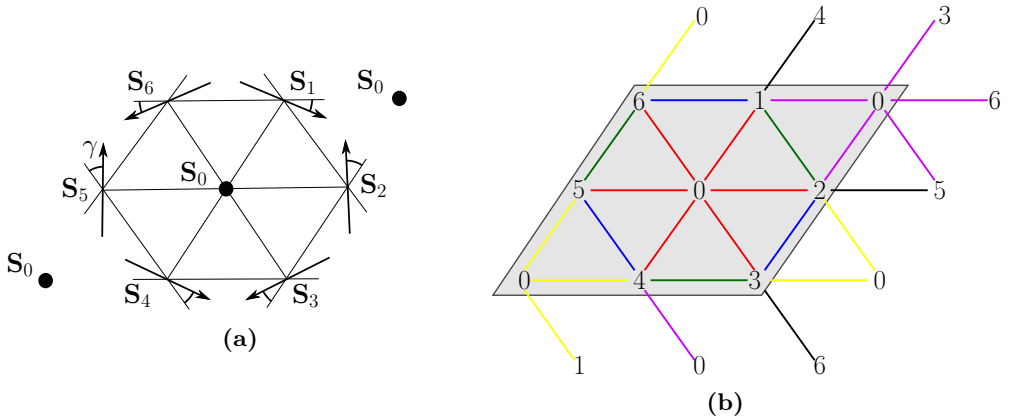

Figure 5.17: Ansatz for the VX phase (a), and schematic representation of the periodicity (b).

The energy is calculated by summing over the spins indicated by the grey area in fig. 5.17b. This calculation is simplified by realising that many of the links between spins are equivalent. For example the blue link $6 \to 1$ can be rotated $2\pi/3$ clockwise to obtain the blue link $3 \to 2$. In total we find six distinct links, indicated by the colour in the figure. Inserting the ansatz spins and adding up the contribution from different links, we obtain the energy

$$E_{\mathrm{VX}} = -2J_1^z \cos\xi + \frac{1}{4}\left(J_2^x - J_2^y + 2J_1^z\right)\cos 2\xi + \frac{1}{4}\left(-J_2^x + J_2^y + 2J_1^z\right) \tag{5.31}$$

Remarkably, the energy is independent of the angle γ, suggesting that the canted spins can rotate freely as long as they all have the same angle. This VX phase is thus continuously degenerate, unlike any other phase in its vicinity in parameter space.

To find the energy minima, we have to minimise an expression on the form $A\cos x + B\cos 2x$. Since S_0^z was set to be negative in the ansatz, we are looking for a positive, non-zero solution. This is given by

$$\cos x = -\frac{A}{4B}, \tag{5.32}$$

from which we obtain

$$\cos 2x = \frac{1}{8}\frac{A^2}{B^2} - 1. \tag{5.33}$$

Inserting these relations into eq. (5.31) gives the minimised energy of the VX phase

$$E_{\mathrm{VX}} = 2\frac{(2\lambda-1)^2\cos^2 2\alpha}{(4\lambda-1)\cos 2\alpha - 1} + \frac{1}{2}\left(\cos 2\alpha - 1\right). \tag{5.34}$$

When $\alpha \to \pi/2$ and $\lambda > 1$, the overall sign is negative. The variational angle can be

expressed on the form

$$\xi = \arccos\left(\frac{2J_1^z}{2J_1^z + J_1^x - J_2^y}\right) = \arccos\left(\frac{2J_1^z}{2J_1^z + (1-\cos 2\alpha)}\right), \tag{5.35}$$

which is always positive when J_1^z is positive.

5.3 Ground state phase diagram

We may now compare the minimised variational phase energies for different values of α and λ. Figure 5.18 shows the lowest variational energies along with numerical results from Monte Carlo annealing for four values of λ.

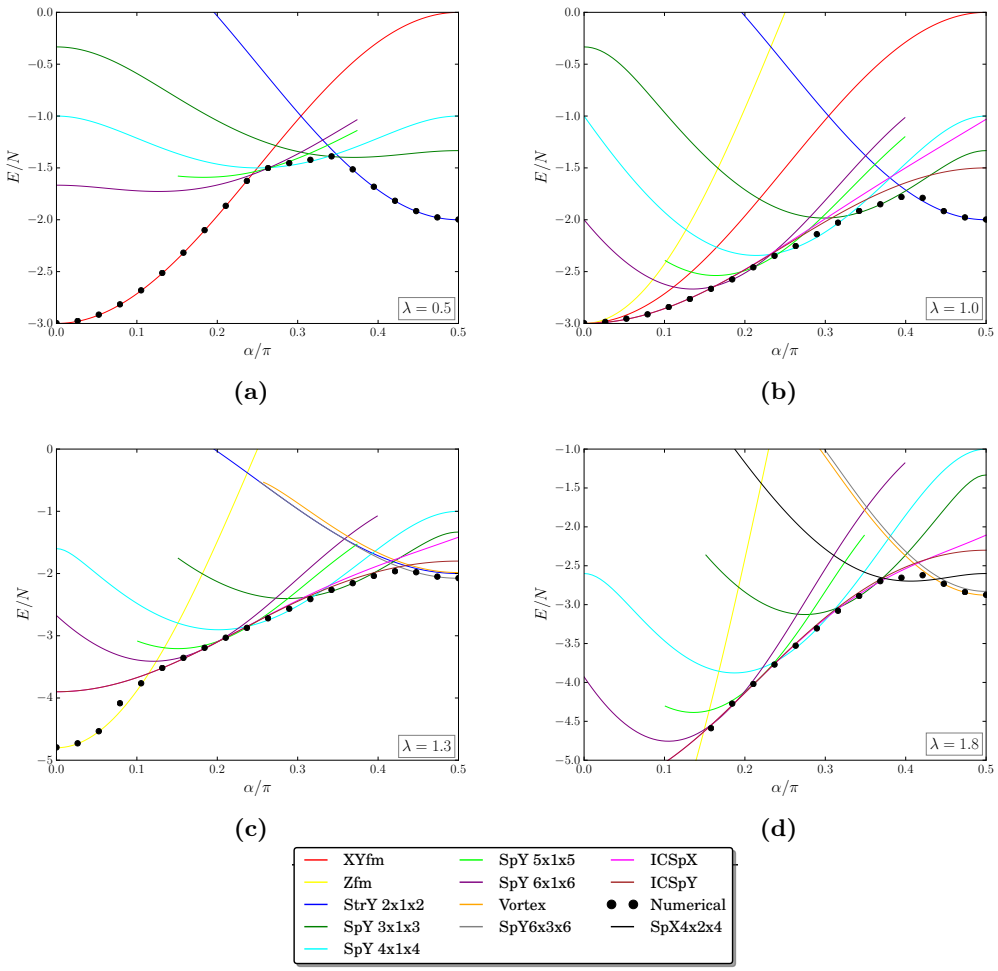

Figure 5.18: Comparison between variational energies for $\lambda = 0.5$ (a), 1.0 (b), 1.3 (c), 1.8 (d). Numerical results from Monte Carlo annealing plotted with dots.

In general the variational energies agree very well with the energies obtained from Monte Carlo annealing. In fig. 5.18c and fig. 5.18d there are slight deviations for the ZFM and SPY 6x3x6 phases, explained by domain walls in the numerical results. For some of the

phases, we have only plotted parts of the energy curves. This is because they reduce to other periodicities in the parts not plotted. For example, the SpY 5x1x5 phase reduces to the XY ferromagnet by setting $\beta_1 = \pi/2$ and $\beta_2 = 3\pi/2$ in the the ansatz (eq. (5.10)). Furthermore we observe that the spiral phases lie very close in energy, especially for large values of the intra-component scattering parameter. In particular, the two incommensurate spiral phases – the brown and pink lines in fig. 5.18 – have the same energy for $\alpha < \pi/4$. As α increases, the SpY ordering has lowest energy for low values of λ, while at higher values the SpX phase wins.

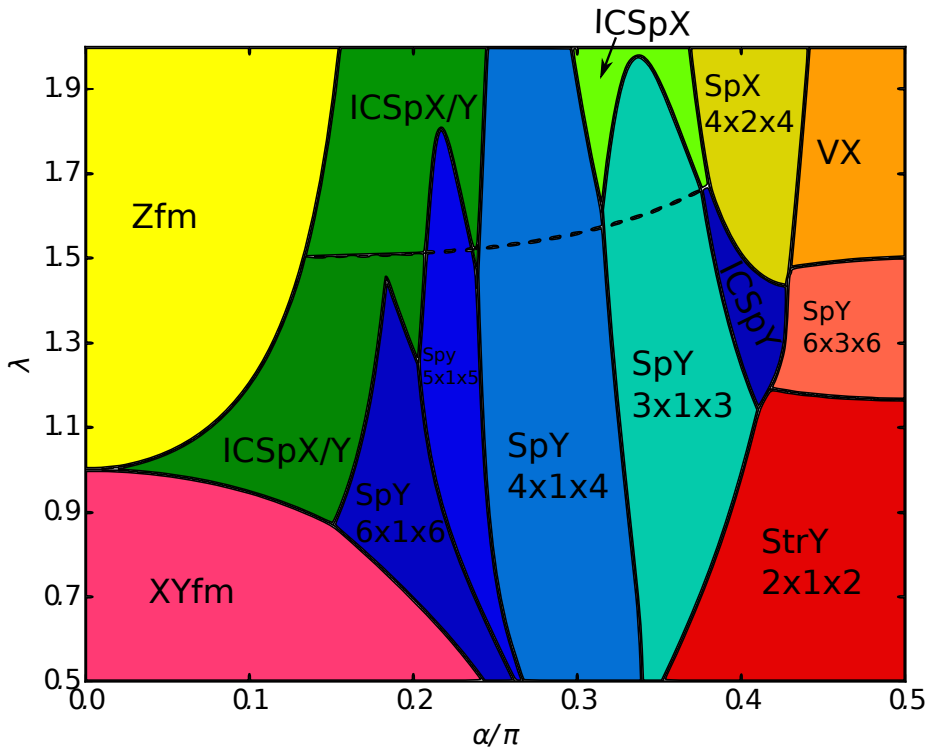

Figure 5.19: Phase diagram obtained from variational energies. The complete overview of every ansatz used is given in section 5.2. The dashed line indicates where the ICSpX phase has less energy than the ICSpY phase.

Comparisons between variational energies are summarised in the classical ground state phase diagram shown in fig. 5.19, obtained by plotting the lowest variational energy at each point in parameter space. Because there are so many competing phases in the spiralling regime, we can not claim more than a qualitative description in this region. The ferromagnetic-, vortex-, complex spiral- and stripe- phases on the other hand stand out, so

we expect these to more accurately describe the true groundstate.

5.3.1 Comparison with Monte Carlo results

The phase diagram can be understood in terms of the magnetic structure factor. Figure 5.20 shows the magnetic structure factor of various points in parameter space from the Monte Carlo results. Comparing this to the phase diagram, we see obvious similarities.

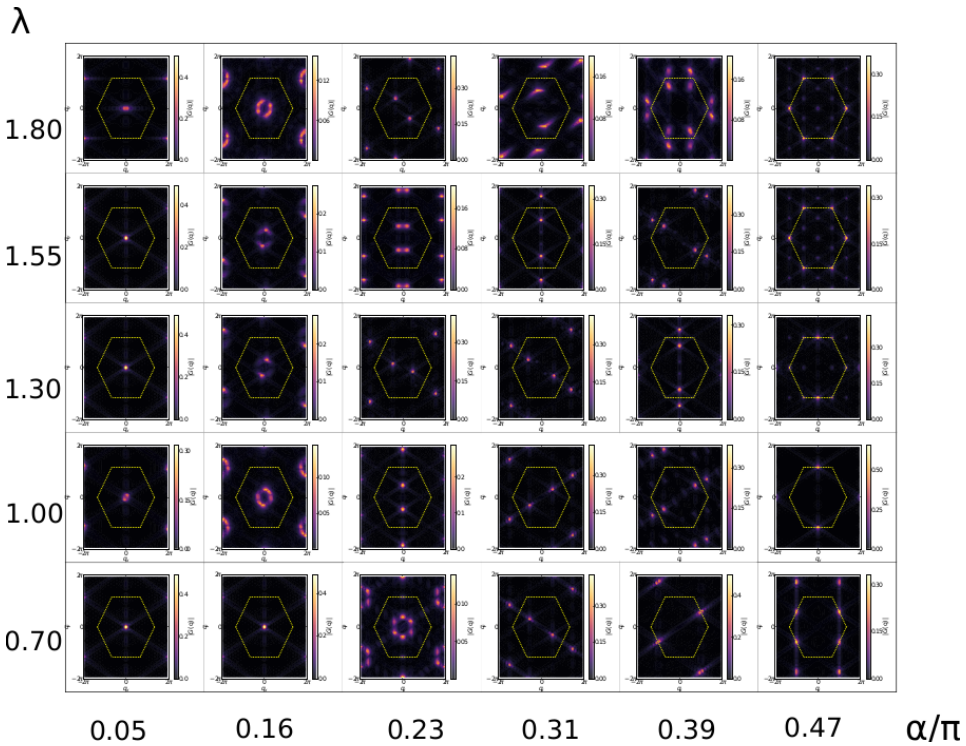

Figure 5.20: Magnetic structure factor for various points in parameter space from Monte Carlo results. Axes are scaled, to better highlight regions of interest.

For low alpha we see one maxima at $\mathbf{q} = 0$, characterising either the easy-plane ferromagnet for $\lambda < 1$ or the easy-axis ferromagnet for $\lambda > 1$. To the right of these phases we see spiralling with long periodicities in multiple directions, characterised by a ring of maximas around the centre of the Brilloine zone. This is consistent with the fact that the two variational incommensurate spiral phases have the same energy in this regime, inducing coexistence of spiralling in several directions in the Monte Carlo results. For intermediate values of $\alpha \simeq \pi/4$, we see the simple spiralling phases. The periodicity of the spiral phases decreases as α is increased, characterised by maximas closer to the edge of the Brilloine zone. For low values of λ spiralling mainly occurs in the yz-plane, while for higher values we

also find SpX-ordering, in qualitative agreement with the variational phase diagram. To the very right, for $\alpha \simeq \pi/2$, we find the StrY-, SpY 6x3x6- and VX-phases characterised by maximas at the Brilloine zone edges. The (semi)-continuous development of the magnetic structure factor – from one maxima at the centre to several maximas at the edges of the Brilloine zone with increasing α – qualitatively explains why we observe SpX ordering for high values of λ, as this turns into the VX phase with maximas at the vertices.

5.3.2 Comparison with literature

To the writer's knowledge no previous work has been done on this exact model, and consequently its hard to verify our results by direct comparison. In this section we argue why the different phases occur based on the relative strength between interactions in the effective spin Hamiltonian (eq. (3.50)) and comparisons with slightly similar models.

As a starting point we may compare our results with work done on the same Bose-Hubbard Hamiltonian on the square lattice by Cole et. al.[37]. Ferromagnetic phases are indifferent to the underlying lattice, and consequently we see that they are almost identical to results obtained on the square lattice. The square lattice model also supports two types of spiral order; one along the lattice bonds that we can compare with SpX-ordering, and one directly between the lattice bonds which can be compared to SpY-ordering. In the square lattice, spiralling between the bonds occur for low λ, consistent with our findings. The two spiralling orders can be understood as a competition between the DM-interaction and the ferromagnetic y-component of the Heisenberg interaction. At high λ, when DM dominates, spiralling occurs in the plane perpendicular to the DM-vectors. For lower λ, the ferromagnetic y-component drags the spiralling order into the yz-plane. In [95] it is shown that DM- and antiferromagnetic Heisenberg-coupling gives rise to spiral order perpendicular to the DM-vector, even in the presence of an external magnetic field[1].

In a purely antiferromagnetic XY-model, geometric frustration leads to the 120° Néel ordering[96]. The StrY ordering, found in our results, is very different from this; while we have antiferromagnetic interactions along the a_1- and a_3-directions, the Heisenberg y-coupling remains ferromagnetic along the a_2-bond. In this region of parameter space on the square lattice, Cole et. al. finds an in-plane vortex phase that is shown to be continuously degenerate in [76]. For a specific orientation, this vortex phase reduces to a stripe phase similar to the one we find, so on the triangular lattice the stripe phase can be interpreted as a result of symmetry breaking from geometric frustration.

Some aspects of the vortex phase can be understood in terms of strong z-antiferromagnetism. In the limit of $\lambda \to \infty$ and $\alpha = \pi/2$, the antiferromagnetic z-couplings dominate and our spin Hamiltonian essentially reduces to the antiferromagnetic Ising model. This has a massively degenerate groundstate where each elemental triangle has two spins up and one down (or equivalently one up and two down)[97]. From the analytic expression for the variational angle ξ, we find that $\lim_{\lambda\to\infty} \xi\big|_{\alpha=\pi/2} = \arccos(1) = 0$, so that the VX phase reduces to the antiferromagnetic Ising model.

[1] The focus of this article is a high-field skyrmion phase, but in a low field they obtain spiral order.

Chapter 6

Thermal excitations

In this chapter we consider the effects of thermal excitations on the ordering of magnetic phases by sampling the helicity modulus using Monte Carlo. The original idea was to use the more common twist-about-axis method (eq. (4.25)) to show that the direct twisting method (eq. (4.28)) works and then use this to measure the helicity modulus with a DM-interaction from SOC. In the end the direct twisting method did not work with DM, discussed in section 6.3, but we still show that the two twisting methods give qualitatively equal results in the Heisenberg model and discuss these. As an introduction we present results for the famous XY-model, known to exhibit a vortex-driven phase transition.

6.1 Ordering in the XY-model

To see how ordering in the XY-model is influenced by thermal fluctuations, we run Monte Carlo simulations in the interval $\beta \in [0, 2]$ with 100 discrete steps. We set $\lambda = 0.5$ and $\alpha = 0$, in the effective spin Hamiltonian, eq. (3.50), to obtain the XY-model given in eq. (4.29). Furthermore, we initialise the spins with random orientations in the xy-plane and set $\phi_R = \pm\pi/4$, $\theta_R = \pi/16$ (eq. (4.16)), so that spins only fluctuate in-plane. For each inverse temperature we use 10^4 initial thermalisation sweeps[1] followed by $5 \cdot 10^5$ Monte Carlo sweeps where the helicity modulus and internal energy is measured every 500'th sweep using the expressions in eq. (4.30) and eq. (4.29). We run one simulation for lattices of size 32×32, 44×44, 54×54 and 64×64.

The result from this simulation is shown in fig. 6.1, where we have plotted the average from twisting along $\hat{\boldsymbol{\mu}} = \hat{\mathbf{x}}, \hat{\mathbf{y}}$ in the lattice. Energy per spin for the same inverse temperatures are shown in the bottom right corner. We can see that the energies are the same for each lattice size, and that they tend towards -3 which is the energy of the XYFM groundstate (eq. (5.2)). Around $\beta = 0.5$, we see the effects of *critical slowing down*. As the system starts to order, large clusters of highly correlated spins are formed. The Monte Carlo algorithm struggles with breaking these up, making it difficult to sample large parts of parameter space. This leads to the statistical errors indicated by deviations from the continuous curve that we would expect. To remedy this, multiple runs could have been done to get a better statistical foundation, but here we are merely interested in showing qualitatively that measuring the helicity modulus using the analytic expression eq. (4.30) works. Furthermore, for $\beta \geq 0.7$

[1] This is really overkill, but does not cost much computational time on the whole.

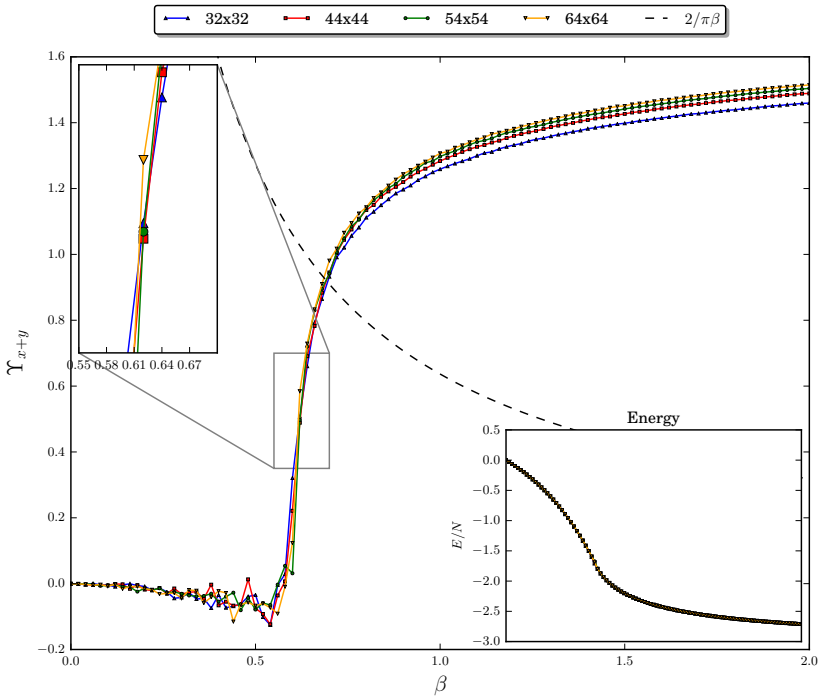

Figure 6.1: Helicity modulus, averaged over the x- and y- direction, of the XY-model plotted as a function of inverse temperature. Energy for the same temperatures in the right corner box. Zoomed area highlights where the curves cross at the critical temperature.

the results give smooth curves where larger lattice sizes give larger values for the helicity modulus, seemingly converging to some finite value in the limit of an infinitely large system.

The critical temperature is given by a negative dip in the fourth order modulus, corresponding to a discontinuous jump in the helicity modulus[98]. Because we are only interested in a qualitative agreement, we measure the critical temperature at the point where the helicity modulus curves intersect, which gives $T_c = \beta_c^{-1} \simeq 1.61$. This is motivated by the fact the the helicity modulus should have a jump of universal magnitude, independent of the lattice size. Furthermore, in [98] the intersection point and fourth order dip are only separated by $\Delta\beta = 0.01$ so using the intersection point gives a qualitatively good description.

To our knowledge, only results from an anti-ferromagnetic Heisenberg model exists on the triangular lattice, investigated in relation to nematic and chiral order in frustrated spin systems[99, 100]. We can however compare our result to ones obtained for a ferromagnetic XY-model on the square lattice giving a critical temperature $T_c = 0.893$ for $J = 1$[93]. The critical temperature is lower on the square lattice because each site is connected by

fewer bonds. Furthermore, it is about 2/3 of what we find on the triangular lattice, which is the ratio between bonds to each lattice site in the respective lattices. In addition to this, we have plotted the helicity modulus given by the magnitude of the universal jump in eq. (4.36) predicted by Nelson and Kosterlitz. In terms of the inverse temperature, the helicity modulus should have the value $2/(\pi\beta_c)$ at the critical temperature, which agrees well with our results. All together we believe that this is compelling evidence that our method works on the triangular lattice, and turn to the slightly more complicated Heisenberg model.

6.2 Ordering in the Heisenberg model

The numerical simulations for the Heisenberg model are similar to the one on the XY-model with slight tweaks. We use the same temperature-regime $\beta \in [0, 2]$, but with 50 discrete steps. In turn we have used 10^3 thermalisation sweeps and 10^6 Monte Carlo sweeps, measuring observables every 100'th sweep. The helicity modulus is a lot harder to sample in the Heisenberg model than the XY-model because configuration space is much larger with 3D spins. Consequently, by trial and error, we set $\theta_R = \pi/8$ to reach more configurations. Furthermore, we ran 8 independent runs for each lattice size to get a better statistical foundation. The helicity modulus was sampled using both the axes-twisting method (eq. (4.25)) and the direct twisting method (eq. (4.28)) in the same run. Error bars are given by the standard error of the eight data points for each temperature from independent runs.

Results for the axis twisting method are shown in fig. 6.2. We show the average of the quantities measured from twisting about the x, y- and z- axis along the two directions in the lattice. We can see that the ordering[2] happens for a higher inverse temperature than for the XY-model, which is reasonable as there are more fluctuations with 3D spins. In contrast to the XY-model, larger lattice sizes give lower values for the helicity modulus in the ordered phase, discussed further in section 6.2.1. This can be compared to results obtained by K. Mon[43] on the square lattice, where the same trend is shown. Furthermore, they measure the helicity modulus to be 0.59 in a 64x64 lattice[3] at $\beta = 2.5$. Assuming the trend shown in fig. 6.2 continues, the corresponding value on the triangular lattice is around 1.0, explained by the fact that there are more bonds than on the square lattice.

We may now compare results from the axis twisting method with those obtained from the direct twisting method, shown in fig. 6.3. Firstly, we can see that this method of measuring is more prone to statistical errors. Because the two methods are sampled for the same data, we conclude that the multiple axis twisting methods give better results because considering all three axes compensates for our inability to sample enough configurations. For low values of β, the direct twisting method gives slightly negative values. The best explanation for this is that in the unordered state the direct twisting method does not correspond to a physical twist through the system, but locally twisting spins apart around some arbitrary axis. As the spins align in the ordered phase these local axes will also align, giving a physical twist like in the axis twisting method. Apart from that, there is an overall good qualitative agreement

[2] "Ordering" is used in lack of a better word, since in a finite small system the Heisenberg model will in fact order.

[3] In this article only one temperature was considered

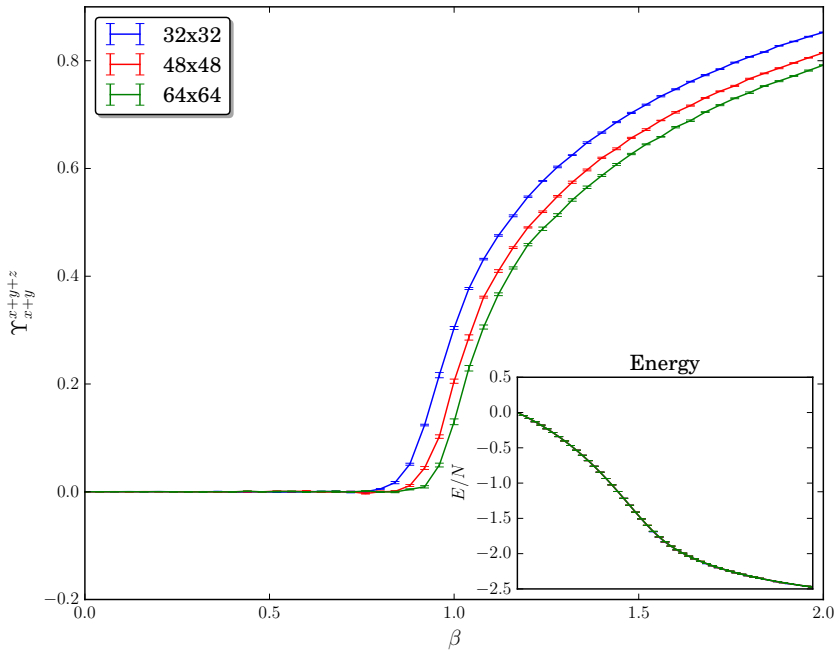

Figure 6.2: Helicity modulus for the Heisenberg model sampled using the axis twisting method, averaged over the x, y and z axis. Curve shows the average of measurements for twists along the x- and y- directions.

between the two curves with transitions at the same temperature, $\beta \simeq 1$. Furthermore, in the direct twisting method we can also see that the helicity modulus is larger for smaller lattice sizes, and the magnitude is of the same order.

6.2.1 Pseudo-critical behaviour

Originally, measuring the helicity modulus for the Heisenberg model was intended as a way of verifying that the two methods gave similar results. When checking for known results in the literature however, it became clear that whether there is QLRO in the Heisenberg model is still an unanswered question of some controversy. The main reason to deny the existence of QLRO in the Heisenberg model is that rotation symmetries of the spins form a non-Abelian group that does not support formation of stable topological defects[101]. In contrast, the XY-model has a corresponding Abelian symmetry supporting defects that we now know to be vortex-pairs. The evidence against QLRO in the Heisenberg model is summarised by J. Kosterlitz in his Nobel Lecture in 2017[102], where he points to numeri-

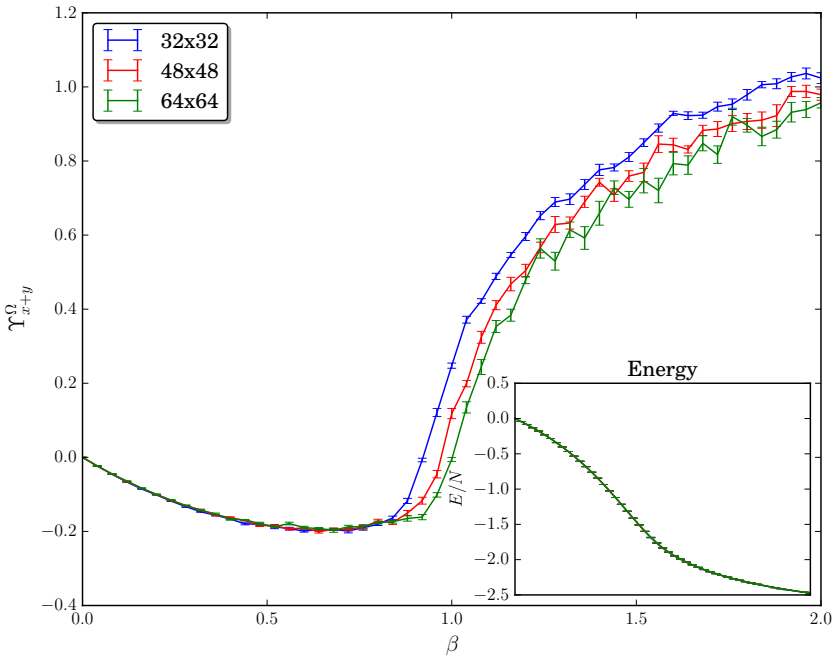

Figure 6.3: Helicity modulus for the Heisenberg model sampled using the direct twisting method. Curve shows the average of measurements for twists along the x- and y- directions.

cal work by Moore[103], normalisation theory by Polyakov[104] and finally experiments on superfluids[105, 106]. Conversely, numerical work in [106] indicates QLRO in the Heisenberg model, while a perturbation expansion used to deny the existence of QLRO is called into question in [107].

The most recent contribution to this discussion we were able to find is an article by Tomita in 2014[108], where finite-size scaling analysis is used to predict *pseudo-critical* behaviour in the Heisenberg model. Pseudo-critical behaviour is characterised by extremely large, yet finite correlation lengths which can be erroneously recognised as infinite by conventional finite size scaling methods because the distinction is very fine. Our results seem to align well with the considerations of Tomita. Around $\beta = 1.0$ there is some size-dependant pseudo-critical temperature below which the correlation length takes very large but ultimately finite values, characterised by the size-dependant decline of the helicity modulus compared to the increase in the XY-model.

6.3 Ordering with spin-orbit coupling

Finally, we present the results obtained from measuring the helicity modulus with SOC in the form of a DM interaction using the direct twisting method introduced in eq. (4.34). As shown in fig. 6.4, inclusion of a DM interaction introduces an unphysical divergence into negative values. A negative helicity modulus would correspond to a local energy maxima, which cannot be true as we found ordered groundstates in the presence of non-zero SOC in chapter 5. Furthermore, in this result we have only introduced a very weak DM-coupling with $J = -1$, $\lambda = 0.2$ and the DM-vectors given by

$$\mathbf{D}_1 = \lambda\left(\frac{\sqrt{3}}{2}\hat{\mathbf{x}} - \frac{1}{2}\hat{\mathbf{y}}\right), \quad \mathbf{D}_2 = -\lambda\hat{\mathbf{y}}, \quad \mathbf{D}_3 = \lambda\left(-\frac{\sqrt{3}}{2}\hat{\mathbf{x}} - \frac{1}{2}\hat{\mathbf{y}}\right), \tag{6.1}$$

in eq. (4.31). Increasing λ leads to greater divergence into negative values. It is worth noting that fig. 6.4 shows one of many failed tests to produce results that made sense, and that we considered other parameter regimes and choices for the DM-vector. We must therefore conclude that this method for measuring the helicity modulus does not work[4].

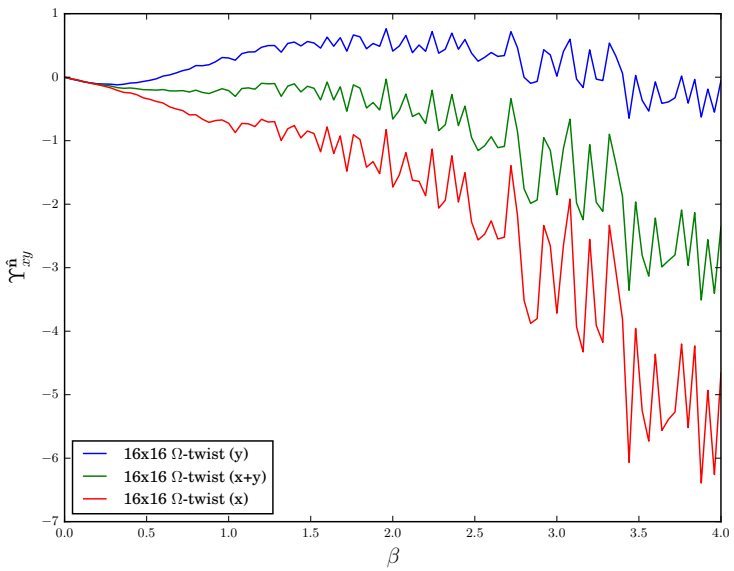

Figure 6.4: Helicity modulus the Heisenberg model with a DM interaction. Unphysical negative values indicate that this result cannot be correct.

[4]Close, but no cigar.

To see what goes wrong, we recall that the helicity modulus is given by

$$\Upsilon_\mu = \left[\beta\left\langle \frac{\partial H}{\partial \delta_\mu}\right\rangle^2 + \left\langle \frac{\partial^2 H}{\partial \delta_\mu^2}\right\rangle - \beta\left\langle \left(\frac{\partial H}{\partial \delta_\mu}\right)^2\right\rangle\right]\Bigg|_{\delta_\mu=0}. \tag{6.2}$$

In the pure Heisenberg model, the first term is proportional to $-\sin(\Omega_{i,i+a})$ which is zero in the ordered phase as it should. Including a DM-interaction however, introduces a non-vanishing term proportional to $\cos(\Omega_{i,i+a})$ causing the first term in the helicity modulus to take non-zero values. This also makes the third term finite in the ordered phase, causing the negative divergence. Furthermore, there is an ambiguity in how we define the angle Φ_a introduced as the angle between the DM-vector and the cross product of neighbouring spins. When neighbouring spins align, the cross product is zero and Φ_a is no longer defined, indicating that the direct twisting method should not work with DM coupling. In retrospect, these are considerations that could have been made before doing numerical simulations. Finally, we note that this method has not – to our knowledge, and for good reason – been used to measure the helicity modulus with SOC previously.

Chapter 7

Summary

In this thesis we have investigated a strongly correlated two-component bosonic system of ultracold atoms with spin-orbit coupling. Starting from a review of the fundamental interactions in such systems, we have shown how ultracold atom experiments are used to investigate spin degrees of freedom coupled by a spin-orbit interaction. Furthermore, we have pointed to literature where such experiments have been realised, leading to groundbreaking discoveries of novel phenomena. Starting from a general quantum mechanical description, the Bose-Hubbard tight binding model was derived for spin-orbit coupled bosons with two pseudo-spin degrees of freedom in a triangular lattice potential. We have also reviewed literature on this model, famous for exhibiting a pure quantum phase transition between a strongly coupled Mott insulator and a delocalised superfluid phase.

In the Mott insulator regime, we derived an effective spin Hamiltonian that has not been considered in literature previously. Comparisons with previous work done on the square lattice, showed that mixed momentum components along the diagonal vertices in the triangular lattice gave rise to an exotic off-diagonal compass coupling, not considered in many previous models. In addition the spin Hamiltonian included a Heisenberg coupling and a Dzyaloshinskii-Moriya interaction, where the latter results exclusively from spin-orbit coupling.

The spin model was studied through extensive Monte Carlo simulations. After a review of the literature on Monte Carlo methods, we showed how the Metropolis Hastings algorithm can be employed in a system of three-dimensional spins. This was done using a fully isotropic selection probability to ensure the crucial requirements of detailed balance and ergodicity. Monte Carlo annealing was used to obtain magnetic groundstate textures for different magnitudes of spin-orbit coupling and inter- relative to intra-component scattering. These results revealed a plethora of magnetic ground states, most of which have been considered in previous works along with a novel vortex phase with a continuous symmetry. The energies of these phases were compared using a variational approach with ansatzes based on the Monte Carlo results, resulting in a zero temperature groundstate phase diagram. This was compared to the Monte Carlo results, were we claim a good qualitative agreement although the boundaries between phases can not be taken as exact.

Finally, we considered the effects of thermal excitations. Due to the absence of long range order in two-dimensional systems, this was done by sampling the helicity modulus. Based on literature, we found two analytic expressions for measuring the helicity modulus of the Heisenberg model. Both these reduced to the same expression for the XY-model,

which we used as an introductory testing ground of our method. Results for the XY-model were compared to numerical work done on the square lattice along with the predictions of Kosterlitz, Thouless and Nelson, where we found a good agreement in both cases. The results from simulations on the Heisenberg model showed that the two methods used gave qualitatively similar results. Encouraged by this, we tried to generalise the direct twisting method to include spin-orbit coupling in the form of a Dzyaloshinksii-Moryia interaction, but this proved fruitless. Results from the Heisenberg model also sparked interest in a controversy of whether the Heisenberg Hamiltonian has a topological phase transition like the XY-model. In our results we found a size-dependant decline in the helicity modulus of the Heisenberg-model, indicating a weaker ordering than the XY-model with pseudo-critical behaviour only occurring in finite systems.

Bibliography

[1] F. Schmidt, J. Maguire, T. Welsh, and S. Bratt, "Operation Experience and further Development of a High-Temperature Superconducting Power Cable in the Long Island Power Authority Grid," *Physics Procedia*, vol. 36, pp. 1137 – 1144, 2012. SUPERCONDUCTIVITY CENTENNIAL Conference 2011.

[2] L. Rossi, "Superconductivity: its role, its success and its setbacks in the Large Hadron Collider of CERN," *Superconductor Science and Technology*, vol. 23, no. 3, p. 034001, 2010.

[3] Aarnink, René and Overweg, Johan, "Magnetic Resonance Imaging, a success story for superconductivity," *Europhysics News*, vol. 43, no. 4, pp. 26–29, 2012.

[4] R. Hanson, L. P. Kouwenhoven, J. R. Petta, S. Tarucha, and L. M. K. Vandersypen, "Spins in few-electron quantum dots," *Rev. Mod. Phys.*, vol. 79, pp. 1217–1265, Oct 2007.

[5] J. Li, P. Ndai, A. Goel, S. Salahuddin, and K. Roy, "Design paradigm for robust spin-torque transfer magnetic ram (stt mram) from circuit/architecture perspective," *IEEE Transactions on Very Large Scale Integration (VLSI) Systems*, vol. 18, pp. 1710–1723, Dec 2010.

[6] B. Dieny, "Giant magnetoresistance in spin-valve multilayers," *Journal of Magnetism and Magnetic Materials*, vol. 136, no. 3, pp. 335 – 359, 1994.

[7] M. Z. Hasan and C. L. Kane, "Colloquium: Topological insulators," *Rev. Mod. Phys.*, vol. 82, pp. 3045–3067, Nov 2010.

[8] C. Gross and I. Bloch, "Quantum simulations with ultracold atoms in optical lattices," *Science*, vol. 357, no. 6355, pp. 995–1001, 2017.

[9] I. Bloch, J. Dalibard, and S. Nascimbène, "Quantum simulations with ultracold quantum gases," *Nature Physics*, vol. 8, pp. 267–276, 2012.

[10] M. H. Anderson, J. R. Ensher, M. R. Matthews, C. E. Wieman, and E. A. Cornell, "Observation of Bose-Einstein Condensation in a Dilute Atomic Vapor," *Science*, vol. 269, no. 5221, pp. 198–201, 1995.

[11] K. B. Davis, M. O. Mewes, M. R. Andrews, N. J. van Druten, D. S. Durfee, D. M. Kurn, and W. Ketterle, "Bose-Einstein Condensation in a Gas of Sodium Atoms," *Phys. Rev. Lett.*, vol. 75, pp. 3969–3973, Nov 1995.

[12] C. C. Bradley, C. A. Sackett, J. J. Tollett, and R. G. Hulet, "Evidence of Bose-Einstein Condensation in an Atomic Gas with Attractive Interactions," *Phys. Rev. Lett.*, vol. 75, pp. 1687–1690, Aug 1995.

[13] A. Einstein, "Quantentheorie des einatomigen idealen gases," *Sitzungsberichte der Preussischen Akademie der Wissenschaften*, vol. 1, no. 3, 1925.

[14] Bose, "Plancks Gesetz und Lichtquantenhypothese," *Zeitschrift für Physik*, vol. 26, pp. 178–181, Dec 1924.

[15] T. Hänsch and A. Schawlow, "Cooling of gases by laser radiation," *Optics Communications*, vol. 13, no. 1, pp. 68 – 69, 1975.

[16] D. Egorov, W. C. Campbell, B. Friedrich, S. Maxwell, E. Tsikata, L. D. van Buuren, and J. Doyle, "Buffer-gas cooling of nh via the beam loaded buffer-gas method," *The European Physical Journal D*, vol. 31, pp. 307–311, 11 2004.

[17] B. K. Stuhl, M. T. Hummon, M. Yeo, G. Quéméner, J. L. Bohn, and J. Ye, "Evaporative cooling of the dipolar hydroxyl radical," *Nature*, vol. 492, pp. 396–400, 2012.

[18] W. S. Bakr, J. I. Gillen, A. Peng, S. Fölling, and M. Greiner, "A quantum gas microscope for detecting single atoms in a Hubbard-regime optical lattice," *Nature*, vol. 462, pp. 74–77, 2009.

[19] J. F. Sherson, C. Weitenberg, M. Endres, M. Cheneau, I. Bloch, and S. Kuhr, "Single-atom-resolved fluorescence imaging of an atomic Mott insulator," *Nature*, vol. 467, pp. 68–72, 2010.

[20] C. J. Myatt, E. A. Burt, R. W. Ghrist, E. A. Cornell, and C. E. Wieman, "Production of Two Overlapping Bose-Einstein Condensates by Sympathetic Cooling," *Phys. Rev. Lett.*, vol. 78, pp. 586–589, Jan 1997.

[21] I. Bloch, "Ultracold quantum gases in optical lattices," *Nature*, vol. 1, pp. 23–30, 2005.

[22] R. Grimm, M. Weidemüller, and Y. B. Ovchinnikov, "Optical Dipole Traps for Neutral Atoms," vol. 42 of *Advances In Atomic, Molecular, and Optical Physics*, pp. 95 – 170, Academic Press, 2000.

[23] C. Chin, R. Grimm, P. Julienne, and E. Tiesinga, "Feshbach resonances in ultracold gases," *Rev. Mod. Phys.*, vol. 82, pp. 1225–1286, Apr 2010.

[24] B. Bransden, "Physics of atoms and molecules," 2003.

[25] R. Winkler, "Spin-orbit coupling effects in two-dimensional electron and hole systems," 2003.

[26] Y. A. Bychkov and É. I. Rashba, "Properties of a 2D electron gas with lifted spectral degeneracy," *Soviet Journal of Experimental and Theoretical Physics Letters*, vol. 39, p. 78, Jan. 1984.

[27] G. Dresselhaus, "Spin-Orbit Coupling Effects in Zinc Blende Structures," *Phys. Rev.*, vol. 100, pp. 580–586, Oct 1955.

[28] B. M. Anderson, G. Juzeliūnas, V. M. Galitski, and I. B. Spielman, "Synthetic 3D Spin-Orbit Coupling," *Phys. Rev. Lett.*, vol. 108, p. 235301, Jun 2012.

[29] J. Sinova, D. Culcer, Q. Niu, N. A. Sinitsyn, T. Jungwirth, and A. H. MacDonald, "Universal Intrinsic Spin Hall Effect," *Phys. Rev. Lett.*, vol. 92, p. 126603, Mar 2004.

[30] V. Galitski and I. B. Spielman, "Spin-orbit coupling in quantum gases," *Nature*, vol. 494, pp. 49–54, 2013.

[31] U. J. Lin, K. Jiménez-García, and I. B. Spielman, "Spin-orbit-coupled Bose-Einstein condensates," *Nature*, vol. 471, pp. 83–86, 2011.

[32] Z. Wu, L. Zhang, W. Sun, X.-T. Xu, B.-Z. Wang, S.-C. Ji, Y. Deng, S. Chen, X.-J. Liu, and J.-W. Pan, "Realization of two-dimensional spin-orbit coupling for Bose-Einstein condensates," *Science*, vol. 354, no. 6308, pp. 83–88, 2016.

[33] "Electron correlations in narrow energy bands," *Proceedings of the Royal Society of London A: Mathematical, Physical and Engineering Sciences*, vol. 276, no. 1365, pp. 238–257, 1963.

[34] M. P. A. Fisher, P. B. Weichman, G. Grinstein, and D. S. Fisher, "Boson localization and the superfluid-insulator transition," *Phys. Rev. B*, vol. 40, pp. 546–570, Jul 1989.

[35] M. Endres, *Probing correlated quantum many-body systems at the single-particle level*. Springer Science & Business, 2014.

[36] A. T. Bolukbasi and M. Iskin, "Superfluid–Mott-insulator transition in the spin-orbit-coupled Bose-Hubbard model," *Phys. Rev. A*, vol. 89, p. 043603, Apr 2014.

[37] W. S. Cole, S. Zhang, A. Paramekanti, and N. Trivedi, "Bose-Hubbard Models with Synthetic Spin-Orbit Coupling: Mott Insulators, Spin Textures, and Superfluidity," *Phys. Rev. Lett.*, vol. 109, p. 085302, Aug 2012.

[38] T. H. R. Skyrme, "A Non-Linear Field Theory," *Proceedings of the Royal Society of London. Series A, Mathematical and Physical Sciences*, vol. 260, no. 1300, pp. 127–138, 1961.

[39] M. Heide, G. Bihlmayer, and S. Blügel, "Dzyaloshinskii-Moriya interaction accounting for the orientation of magnetic domains in ultrathin films: Fe/W(110)," *Phys. Rev. B*, vol. 78, p. 140403, Oct 2008.

[40] N. Romming, C. Hanneken, M. Menzel, J. E. Bickel, B. Wolter, K. von Bergmann, A. Kubetzka, and R. Wiesendanger, "Writing and Deleting Single Magnetic Skyrmions," *Science*, vol. 341, no. 6146, pp. 636–639, 2013.

[41] L. Balents, "Spin liquids in frustrated magnets," *Nature*, vol. 464, pp. 199–208, 2010.

[42] M. Caffarel, P. Azaria, B. Delamotte, and D. Mouhanna, "Monte Carlo Calculation of the Spin Stiffness of the Two-Dimensional Heisenberg Model," *EPL (Europhysics Letters)*, vol. 26, no. 7, p. 493, 1994.

[43] K. K. Mon, "Monte Carlo studies of spin-stiffness fluctuations in the two-dimensional classical Heisenberg model," *Phys. Rev. B*, vol. 44, pp. 6809–6811, Oct 1991.

[44] G. Shlyapnikov, "Ultracold quantum gases, part 1: Bose-condensed gases," 2014.

[45] C. J. Pethick and H. Smith, *Bose-Einstein condensation in dilute gases*. Cambridge university press, 2002.

[46] W. D. Phillips, "Nobel Lecture: Laser cooling and trapping of neutral atoms," *Rev. Mod. Phys.*, vol. 70, pp. 721–741, Jul 1998.

[47] P. M. Duarte, R. A. Hart, J. M. Hitchcock, T. A. Corcovilos, T.-L. Yang, A. Reed, and R. G. Hulet, "All-optical production of a lithium quantum gas using narrow-line laser cooling," *Phys. Rev. A*, vol. 84, p. 061406, Dec 2011.

[48] S. R. Granade, M. E. Gehm, K. M. O'Hara, and J. E. Thomas, "All-Optical Production of a Degenerate Fermi Gas," *Phys. Rev. Lett.*, vol. 88, p. 120405, Mar 2002.

[49] K. M. O'Hara, S. L. Hemmer, M. E. Gehm, S. R. Granade, and J. E. Thomas, "Observation of a Strongly Interacting Degenerate Fermi Gas of Atoms," *Science*, vol. 298, no. 5601, pp. 2179–2182, 2002.

[50] T. Weber, J. Herbig, M. Mark, H.-C. Nägerl, and R. Grimm, "Bose-Einstein Condensation of Cesium," *Science*, vol. 299, no. 5604, pp. 232–235, 2003.

[51] W. Petrich, M. H. Anderson, J. R. Ensher, and E. A. Cornell, "Stable, Tightly Confining Magnetic Trap for Evaporative Cooling of Neutral Atoms," *Phys. Rev. Lett.*, vol. 74, pp. 3352–3355, Apr 1995.

[52] C. S. Adams, H. J. Lee, N. Davidson, M. Kasevich, and S. Chu, "Evaporative Cooling in a Crossed Dipole Trap," *Phys. Rev. Lett.*, vol. 74, pp. 3577–3580, May 1995.

[53] D. M. Stamper-Kurn, M. R. Andrews, A. P. Chikkatur, S. Inouye, H.-J. Miesner, J. Stenger, and W. Ketterle, "Optical Confinement of a Bose-Einstein Condensate," *Phys. Rev. Lett.*, vol. 80, pp. 2027–2030, Mar 1998.

[54] G. Modugno, G. Ferrari, G. Roati, R. J. Brecha, A. Simoni, and M. Inguscio, "Bose-Einstein Condensation of Potassium Atoms by Sympathetic Cooling," *Science*, vol. 294, no. 5545, pp. 1320–1322, 2001.

[55] B. Paredes, A. Widera, V. Murg, O. Mandel, S. Fölling, I. Cirac, G. V. Shlyapnikov, T. W. Hänsch, and I. Bloch, "Tonks–Girardeau gas of ultracold atoms in an optical lattice," *Nature*, vol. 429, pp. 277–281, 2004.

[56] M. Köhl, H. Moritz, T. Stöferle, K. Günter, and T. Esslinger, "Fermionic Atoms in a Three Dimensional Optical Lattice: Observing Fermi Surfaces, Dynamics, and Interactions," *Phys. Rev. Lett.*, vol. 94, p. 080403, Mar 2005.

[57] G. Reinaudi, T. Lahaye, Z. Wang, and D. Guéry-Odelin, "Strong saturation absorption imaging of dense clouds of ultracold atoms," *Opt. Lett.*, vol. 32, pp. 3143–3145, Nov 2007.

[58] W. E. Lamb and R. C. Retherford, "Fine Structure of the Hydrogen Atom by a Microwave Method," *Phys. Rev.*, vol. 72, pp. 241–243, Aug 1947.

[59] H. Friedrich and H. Friedrich, *Theoretical atomic physics*, vol. 2. Springer, 1991.

[60] S. Millman and M. Fox, "Nuclear Spins and Magnetic Moments of Rb^{85} and Rb^{87}," *Phys. Rev.*, vol. 50, pp. 220–225, Aug 1936.

[61] L. H. Thomas, "The Motion of the Spinning Electron," *Nature*, vol. 117, 1926.

[62] L. T. B.A., "I. The kinematics of an electron with an axis," *The London, Edinburgh, and Dublin Philosophical Magazine and Journal of Science*, vol. 3, no. 13, pp. 1–22, 1927.

[63] M. P. Surh, M.-F. Li, and S. G. Louie, "Spin-orbit splitting of GaAs and InSb bands near Γ," *Phys. Rev. B*, vol. 43, pp. 4286–4294, Feb 1991.

[64] C. V. Raman, "A new radiation," 1928.

[65] M. Aidelsburger, "Cold atoms twisting spin and momentum," *Science*, vol. 354, no. 6308, pp. 35–36, 2016.

[66] J. Struck, M. Weinberg, C. Ölschläger, P. Windpassinger, J. Simonet, K. Sengstock, R. Höppner, P. Hauke, A. Eckardt, M. Lewenstein, and L. Mathey, "Engineering Ising-XY spin-models in a triangular lattice using tunable artificial gauge fields," *Nature Physics*, vol. 9, pp. 738–743, 2013.

[67] P. C. Hemmer, *Kvantemekanikk*. tapir akademisk forlag, 5 ed., 2005.

[68] A. Marte, T. Volz, J. Schuster, S. Dürr, G. Rempe, E. G. M. van Kempen, and B. J. Verhaar, "Feshbach Resonances in Rubidium 87: Precision Measurement and Analysis," *Phys. Rev. Lett.*, vol. 89, p. 283202, Dec 2002.

[69] Fatemi, Jones, and Lett, "Observation of optically induced feshbach resonances in collisions of cold atoms," *Physical review letters*, vol. 85, November 2000.

[70] L. Zhang, Y. Deng, and P. Zhang, "Scattering and effective interactions of ultracold atoms with spin-orbit coupling," vol. 87, November 2012.

[71] M. Hermele, "Second Quantization, unpublished lecture notes," 2010.

[72] W. Kohn, "Analytic Properties of Bloch Waves and Wannier Functions," *Phys. Rev.*, vol. 115, pp. 809–821, Aug 1959.

[73] W. Zwerger, "Mott–Hubbard transition of cold atoms in optical lattices," *Journal of Optics B: Quantum and Semiclassical Optics*, vol. 5, no. 2, p. S9, 2003.

[74] M. Greiner, O. Mandel, T. Esslinger, T. W. Hänsch, and I. Bloch, "Quantum phase transition from a superfluid to a Mott insulator in a gas of ultracold atoms," *Nature*, vol. 415, pp. 39–44, 2002.

[75] K. Sellin and E. Babaev, "Superfluid drag in the two-component Bose-Hubbard model," *Phys. Rev. B*, vol. 97, p. 094517, Mar 2018.

[76] E. Thingstad, "Two-component spin-orbit coupled ultracold atoms in weak and strong coupling regimes," *Master thesis, NTNU*, 2017.

[77] I. Dzyaloshinsky, "A thermodynamic theory of "weak" ferromagnetism of antiferromagnetics," *Journal of Physics and Chemistry of Solids*, vol. 4, no. 4, pp. 241 – 255, 1958.

[78] T. Moriya, "Anisotropic Superexchange Interaction and Weak Ferromagnetism," *Phys. Rev.*, vol. 120, pp. 91–98, Oct 1960.

[79] M. Gong, Y. Qian, M. Yan, V. W. Scarola, and C. Zhang, "Dzyaloshinskii-Moriya Interaction and Spiral Order in Spin-orbit Coupled Optical Lattices," *Scientific Reports*, vol. 5, no. 10050, 2015.

[80] J. Chen, W. P. Cai, M. H. Qin, S. Dong, X. B. Lu, X. S. Gao, and J.-M. Liu, "Helical and skyrmion lattice phases in three-dimensional chiral magnets: Effect of anisotropic interactions," *Scientific Reports*, vol. 7, no. 7392, 2017.

[81] Z. Nussinov and J. van den Brink, "Compass models: Theory and physical motivations," *Rev. Mod. Phys.*, vol. 87, pp. 1–59, Jan 2015.

[82] A. Kitaev, "Anyons in an exactly solved model and beyond," *Annals of Physics*, vol. 321, no. 1, pp. 2 – 111, 2006. January Special Issue.

[83] D. P. Landau and K. Binder, *A Guide to Monte Carlo Simulations in Statistical Physics*. Cambridge University Press, 4 ed., 2014.

[84] J. O. Andersen, *Introduction to Statistical Mechanics*. Akademika Forlag, 2014.

[85] W. K. Hastings, "Monte Carlo Sampling Methods Using Markov Chains and Their Applications," *Biometrika*, vol. 57, no. 1, pp. 97–109, 1970.

[86] N. Metropolis, A. W. Rosenbluth, M. N. Rosenbluth, A. H. Teller, and E. Teller, "Equation of state calculations by fast computing machines," *The journal of chemical physics*, vol. 21, no. 6, pp. 1087–1092, 1953.

[87] W. Stephan and B. W. Southern, "Monte Carlo study of the anisotropic Heisenberg antiferromagnet on the triangular lattice," *Phys. Rev. B*, vol. 61, pp. 11514–11520, May 2000.

[88] N. D. Mermin and H. Wagner, "Absence of Ferromagnetism or Antiferromagnetism in One- or Two-Dimensional Isotropic Heisenberg Models," *Phys. Rev. Lett.*, vol. 17, pp. 1133–1136, Nov 1966.

[89] P. C. Hohenberg, "Existence of Long-Range Order in One and Two Dimensions," *Phys. Rev.*, vol. 158, pp. 383–386, Jun 1967.

[90] V. Berezinskii, "Destruction of long-range order in one-dimensional and two-dimensional systems having a continuous symmetry group i. classical systems," *Sov. Phys. JETP*, vol. 32, no. 3, pp. 493–500, 1971.

[91] J. M. Kosterlitz and D. J. Thouless, "Ordering, metastability and phase transitions in two-dimensional systems," *Journal of Physics C: Solid State Physics*, vol. 6, no. 7, p. 1181, 1973.

[92] J. M. Kosterlitz and D. J. Thouless, "Long range order and metastability in two dimensional solids and superfluids. (Application of dislocation theory)," *Journal of Physics C: Solid State Physics*, vol. 5, no. 11, p. L124, 1972.

[93] P. Olsson and P. Minnhagen, "On the helicity modulus, the critical temperature and Monte Carlo simulations for the two-dimensional XY-model," *Physica Scripta*, vol. 43, no. 2, p. 203, 1991.

[94] D. R. Nelson and J. M. Kosterlitz, "Universal Jump in the Superfluid Density of Two-Dimensional Superfluids," *Phys. Rev. Lett.*, vol. 39, pp. 1201–1205, Nov 1977.

[95] H. D. Rosales, D. C. Cabra, and P. Pujol, "Three-sublattice skyrmion crystal in the antiferromagnetic triangular lattice," *Phys. Rev. B*, vol. 92, p. 214439, Dec 2015.

[96] S. E. Korshunov, "Phase diagram of the antiferromagnetic XY model with a triangular lattice in an external magnetic field," *Journal of Physics C: Solid State Physics*, vol. 19, no. 29, p. 5927, 1986.

[97] R. Liebmann, "Statistical mechanics of periodic frustrated ising systems," 1986.

[98] P. N. Galteland and A. Sudbø, "Competing interactions in population-imbalanced two-component Bose-Einstein condensates," *Phys. Rev. B*, vol. 94, p. 054510, Aug 2016.

[99] J.-H. Park, S. Onoda, N. Nagaosa, and J. H. Han, "Nematic and Chiral Order for Planar Spins on a Triangular Lattice," *Phys. Rev. Lett.*, vol. 101, p. 167202, Oct 2008.

[100] T. Obuchi and H. Kawamura, "Spin and Chiral Orderings of the Antiferromagnetic XY Model on the Triangular Lattice and Their Critical Properties," *Journal of the Physical Society of Japan*, vol. 81, no. 5, p. 054003, 2012.

[101] O. Kapikranian, B. Berche, and Y. Holovatch, "Quasi-long-range ordering in a finite-size 2D classical Heisenberg model," *Journal of Physics A: Mathematical and Theoretical*.

[102] J. M. Kosterlitz, "Nobel Lecture: Topological defects and phase transitions," *Rev. Mod. Phys.*, vol. 89, p. 040501, Oct 2017.

[103] M. A. Moore, "Additional Evidence for a Phase Transition in the Plane-Rotator and Classical Heisenberg Models for Two-Dimensional Lattices," *Phys. Rev. Lett.*, vol. 23, pp. 861–863, Oct 1969.

[104] A. Polyakov, "Interaction of goldstone particles in two dimensions. Applications to ferromagnets and massive Yang-Mills fields," *Physics Letters B*, vol. 59, no. 1, pp. 79 – 81, 1975.

[105] M. Chester, L. C. Yang, and J. B. Stephens, "Quartz Microbalance Studies of an Adsorbed Helium Film," *Phys. Rev. Lett.*, vol. 29, pp. 211–214, Jul 1972.

[106] M. Chester and L. C. Yang, "Superfluid Fraction in Thin Helium Films," *Phys. Rev. Lett.*, vol. 31, pp. 1377–1380, Dec 1973.

[107] M. Aguado and E. Seiler, "Some new results on an old controversy: Is perturbation theory the correct asymptotic expansion in non-Abelian models?," *Phys. Rev. D*, vol. 70, p. 107706, Nov 2004.

[108] Y. Tomita, "Finite-size scaling analysis of pseudocritical region in two-dimensional continuous-spin systems," *Phys. Rev. E*, vol. 90, p. 032109, Sep 2014.

Appendix A

Fourier transform derivation

We consider the three terms of the Hamiltonian separately. The sum over a and l in eq. (3.50) is taken to be implicit during the derivation for brevity. The identity

$$\frac{1}{N}\sum_i e^{i(\mathbf{q}-\mathbf{q}')\cdot\mathbf{r}_i} = \delta_{\mathbf{q},\mathbf{q}'}, \tag{A.1}$$

is used frequently along with symmetry properties of the transform around $\mathbf{q} = 0$. Inserting the Fourier transform given by eq. (3.58), we consider each term separately.

- **Heisenberg term:**

$$\begin{aligned} H_H &= \sum_i J_a^l S_i^l S_{i+a}^l = \frac{1}{N} \sum_{i,\mathbf{q}\mathbf{q}'} J_a^l S_{\mathbf{q}}^l e^{-i\mathbf{q}\cdot\mathbf{r}_i} S_{\mathbf{q}'}^l e^{-i\mathbf{q}'(\mathbf{r}_i+\boldsymbol{\epsilon}_a)} \\ &= \sum_{\mathbf{q}\mathbf{q}'} J_a^l S_{\mathbf{q}}^l S_{\mathbf{q}'}^l e^{-i\mathbf{q}'\cdot\boldsymbol{\epsilon}_a} \delta_{\mathbf{q},-\mathbf{q}'} = \sum_{\mathbf{q}} J_a^l S_{\mathbf{q}}^l S_{-\mathbf{q}}^l e^{i\mathbf{q}\cdot\boldsymbol{\epsilon}_a} \\ &= \sum_{\mathbf{q}} J_a^l S_{\mathbf{q}}^l S_{-\mathbf{q}}^l (\cos(\mathbf{q}\cdot\boldsymbol{\epsilon}_a) + i\sin(\mathbf{q}\cdot\boldsymbol{\epsilon}_a)) \\ &= \sum_{\mathbf{q}} J_a^l S_{\mathbf{q}}^l S_{-\mathbf{q}}^l \cos(\mathbf{q}\cdot\boldsymbol{\epsilon}_a). \end{aligned} \tag{A.2}$$

  The last line follows from the asymmetry of the sine function around $\mathbf{q} = 0$.

- **Dzyaloshinskii-Moriya term:**

$$\begin{aligned} H_{DM} &= \sum_i \mathbf{D}_a \cdot (\mathbf{S}_i \times \mathbf{S}_{i+a}) \\ &= \frac{1}{N} \sum_{i,\mathbf{q}\mathbf{q}'} \mathbf{D} \cdot (\mathbf{S}_{\mathbf{q}} e^{-i\mathbf{q}\cdot\mathbf{r}_i} \times \mathbf{S}_{\mathbf{q}'} e^{-i\mathbf{q}'\cdot(\mathbf{r}_i+\boldsymbol{\epsilon}_a)}) \\ &= \sum_{\mathbf{q}} \mathbf{D}_a \cdot (\mathbf{S}_{\mathbf{q}} \times \mathbf{S}_{-\mathbf{q}})(\cos(\mathbf{q}\cdot\boldsymbol{\epsilon}_a) + i\sin(\mathbf{q}\cdot\boldsymbol{\epsilon}_a)) \\ &= \sum_{\mathbf{q}} i\mathbf{D}_a \cdot (\mathbf{S}_{\mathbf{q}} \times \mathbf{S}_{-\mathbf{q}}) \sin(\mathbf{q}\cdot\boldsymbol{\epsilon}_a) \end{aligned} \tag{A.3}$$

  The last line follows from the asymmetry of the cross-product and the sine function. Using ${\mathbf{S}_{\mathbf{q}}}^* = \mathbf{S}_{-\mathbf{q}}$ we find

$$\mathbf{S}_{\mathbf{q}} \times \mathbf{S}_{-\mathbf{q}} = -(\mathbf{S}_{-\mathbf{q}} \times \mathbf{S}_{\mathbf{q}}) = -({\mathbf{S}_{\mathbf{q}}}^* \times {\mathbf{S}_{-\mathbf{q}}}^*) = -(\mathbf{S}_{\mathbf{q}} \times \mathbf{S}_{-\mathbf{q}})^*, \tag{A.4}$$

  showing that the cross product is purely imaginary. Thus H_{DM} gives real energies.

- **K term**

$$\begin{aligned} H_K &= \sum_i K_a (S_i^x S_{i+a}^y + S_i^y S_{i+a}^x) \\ &= \frac{1}{N} \sum_{i,\mathbf{q}\mathbf{q}'} K_a (S_{\mathbf{q}}^x S_{\mathbf{q}'}^y + S_{\mathbf{q}}^y S_{\mathbf{q}'}^x) e^{-i\mathbf{q}\cdot\mathbf{r}_i} e^{-i\mathbf{q}\cdot(\mathbf{r}_i+\boldsymbol{\epsilon}_a)} \\ &= \sum_{\mathbf{q}} K_a (S_{\mathbf{q}}^x S_{-\mathbf{q}}^y + S_{\mathbf{q}}^y S_{-\mathbf{q}}^x)(\cos(\mathbf{q}\cdot\boldsymbol{\epsilon}_a) + i\sin(\mathbf{q}\cdot\boldsymbol{\epsilon}_a)) \\ &= \sum_{\mathbf{q}} K_a (S_{\mathbf{q}}^x S_{-\mathbf{q}}^y + S_{\mathbf{q}}^y S_{-\mathbf{q}}^x) \cos(\mathbf{q}\cdot\boldsymbol{\epsilon}_a) \end{aligned} \tag{A.5}$$